

FINAL REPORT

Grant Number N00014-07-1-0226

Light Scattering by Marine Particles: Modeling with Non-Spherical Shapes

Howard R. Gordon
Department of Physics
University of Miami
Coral Gables, FL 33124
hgordon@miami.edu

20110425663

REPORT DOCUMENTATION PAGE				Form Approved OMB No. 0704-0188								
<p>The public reporting burden for this collection of information is estimated to average 1 hour per response, including the time for reviewing instructions, searching existing data sources, gathering and maintaining the data needed, and completing and reviewing the collection of information. Send comments regarding this burden estimate or any other aspect of this collection of information, including suggestions for reducing the burden, to Department of Defense, Washington Headquarters Services, Directorate for Information Operations and Reports (0704-0188), 1215 Jefferson Davis Highway, Suite 1204, Arlington, VA 22202-4302. Respondents should be aware that notwithstanding any other provision of law, no person shall be subject to any penalty for failing to comply with a collection of information if it does not display a currently valid OMB control number.</p> <p>PLEASE DO NOT RETURN YOUR FORM TO THE ABOVE ADDRESS.</p>												
1. REPORT DATE (DD-MM-YYYY) 04/15/2011		2. REPORT TYPE Final		3. DATES COVERED (From - To) 01-12-2006 to 28-2-2011								
4. TITLE AND SUBTITLE Light Scattering by Marine Particles: Modeling with Non-Spherical Shapes				5a. CONTRACT NUMBER								
				5b. GRANT NUMBER N00014-07-1-0226								
				5c. PROGRAM ELEMENT NUMBER								
6. AUTHOR(S) Howard R. Gordon				5d. PROJECT NUMBER								
				5e. TASK NUMBER								
				5f. WORK UNIT NUMBER								
7. PERFORMING ORGANIZATION NAME(S) AND ADDRESS(ES) University of Miami Sponsored Programs Fiscal Management PO Box 248293 Coral Gables, FL 33124-5215				8. PERFORMING ORGANIZATION REPORT NUMBER								
9. SPONSORING/MONITORING AGENCY NAME(S) AND ADDRESS(ES) Steven G. Ackleson Office of Naval Research 875 North Randolph Street Arlington, VA 22203-1995				10. SPONSOR/MONITOR'S ACRONYM(S)								
				11. SPONSOR/MONITOR'S REPORT NUMBER(S)								
12. DISTRIBUTION/AVAILABILITY STATEMENT Approved for public release; distribution is unlimited.												
13. SUPPLEMENTARY NOTES												
14. ABSTRACT This report describes research that focuses on the influence of particle shape on the inherent optical properties (IOPs) of marine particles. The main result is that significant improvement in modeling IOPs of marine particles can be obtained by using particle models that are similar in shape to the gross morphology of the particles in question. As an example, the spectral shape and magnitude of the backscattering cross section of the coccolithophored <i>E. huxleyi</i> was successfully reproduced with the particle modeled grossly as a parallel pair of thin disks in random orientation.												
15. SUBJECT TERMS Extinction, scattering, backscattering, particle shape												
16. SECURITY CLASSIFICATION OF: <table border="1" style="width: 100%; border-collapse: collapse;"> <tr> <td style="width: 33%; padding: 2px;">a. REPORT</td> <td style="width: 33%; padding: 2px;">b. ABSTRACT</td> <td style="width: 33%; padding: 2px;">c. THIS PAGE</td> </tr> <tr> <td style="height: 40px;"></td> <td></td> <td></td> </tr> </table>			a. REPORT	b. ABSTRACT	c. THIS PAGE				17. LIMITATION OF ABSTRACT		18. NUMBER OF PAGES 67	
a. REPORT	b. ABSTRACT	c. THIS PAGE										
					19a. NAME OF RESPONSIBLE PERSON Howard Gordon							
					19b. TELEPHONE NUMBER (Include area code) 305-284-2323-1							

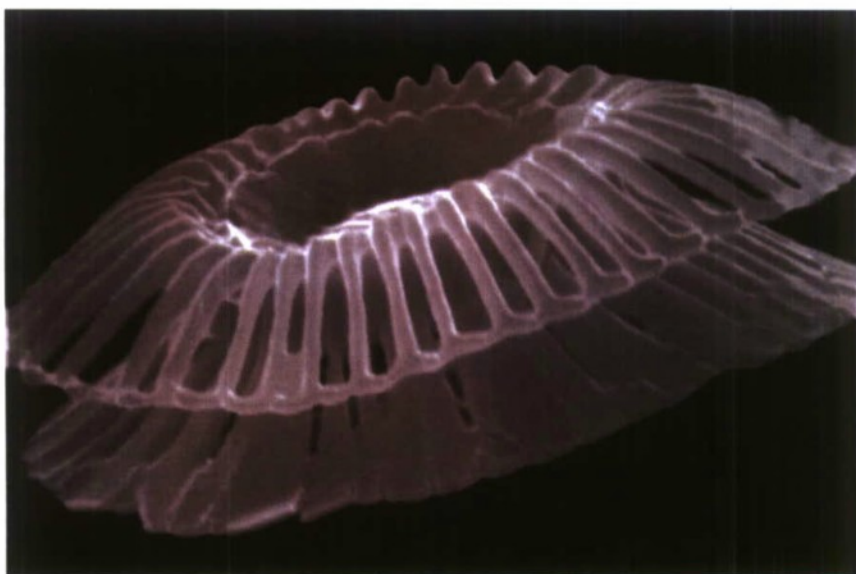
Abstract

Typically, explanation/interpretation of observed light scattering and absorption properties of marine particles is based on assuming a spherical shape and homogeneous composition. Although this approach has been fruitful, the next logical step in modeling marine particles is to abandon the normally-employed spherical approximation and use more realistic approximations to their shape. The advent of computer codes capable of handling more complex shapes, and the increased computational speeds now available, suggest that particle modeling employing simple non-spherical shapes, e.g., disks, rods, etc., could become routine. This report describes research by the author that focuses on the influence of shape on the inherent optical properties (IOPs) of marine particles.

Summary

A. Modeling backscattering of *E. huxleyi* coccoliths

Much of this work was motivated by a desire to build a physical model of coccoliths detached from the coccolithophored *E. huxleyi*. The purpose of the model was to see how well it, when coupled with a light scattering code capable of handling such complex shapes, could reproduce the observed spectral backscattering of detached coccoliths [Gordon and Du, 2001]. The spectral backscattering coefficient is central to the remote sensing of natural waters in the visible, as the water-leaving radiance at a given wavelength is proportional to (b_b/a) , where b_b is the backscattering coefficient and a is the absorption coefficient of the water and its constituents [Gordon and Morel, 1983]. An example of a detached coccolith is provided in the figure below.



In the figure above, the diameter of the disks is $\sim 3 \mu\text{m}$, and the thickness of each plate is $\sim 50 - 100 \text{ nm}$, and the material is calcite. The structures resembling spokes of a wheel are nearly periodic, but not exactly periodic.

In an earlier work I examined the influence of small-scale periodic structures on the backscattering of disk-like particles. The principal result of that work was that when the scale of the periodicity was $> \lambda/4$ (where λ is the wavelength of the light in the water) the backscattering was significantly enhanced over that for smaller scaled periodicities. Here, we build on the earlier work by examining the backscattering of similar particles with small-scale aperiodic structures. The aperiodic structure was formed by randomly perturbing a periodic structure. Although the backscattering cross section σ_{bb} for individual realizations of an aperiodic disk can differ significantly from that of its periodic counterpart, averaging over several realizations brings the two into confluence, unless the aperiodicity is too large. The computations provided in **Appendix 1** suggest that using disks with perfectly periodic (as opposed to quasi-periodic) fine structure for modeling the backscattering of detached coccoliths from *E. huxleyi* is justified.

In earlier work [Gordon, 2006] I showed that the curvature of the disk-like plates is likely to make only a negligible contribution to their spectral backscattering. Thus, I modeled detached coccoliths as a set of two parallel disks with periodic angular sectors joined by a hollow cylinder. **Appendix 2** describes in detail the parameters of the model and the comparison between the model-coccolith's light scattering properties and the experimentally-determined spectral backscattering of detached coccoliths. Briefly, we used *in-situ* radiance/irradiance profiles to retrieve profiles of the spectral backscattering coefficient for all particles in an *E. huxleyi* coccolithophore bloom off the coast of Plymouth, UK. At high detached coccolith concentrations the spectra of backscattering all showed a minimum near ~ 550 to 600 nm . Using flow cytometry estimates of the detached coccolith concentration, and assuming all of the backscattering (over and above the backscattering by the water itself) was due to detached coccoliths, we determined the upper limit of the backscattering cross section (σ_{bb}) of individual coccoliths to be $0.123 \pm 0.039 \mu\text{m}^2/\text{coccolith}$ at 500 nm . The physical model of a detached coccoliths (described above) was combined with the discrete dipole approximation to light scattering [Draine, 1988; Draine and Flatau, 1994] to compute the average backscattering cross section in random orientation. The result was $\sigma_{bb} = 0.092 \mu\text{m}^2$ at 500 nm , with the computed σ_{bb} displaying a spectral shape similar to the measurements. When σ_{bb} was computed on a per mole of calcite, rather than a per coccolith basis, it agreed reasonably well with that determined for acid-labile backscattering at 632 nm averaged over several species of cultured calcifying algae. Intact coccolithophore cells were taken into account by arguing that coccoliths attached to coccolithophore cells (forming a "coccosphere") backscatter in a manner similar to free coccoliths in random orientation. Estimating the number of coccoliths per coccosphere and using the observed number of coccolithophore cells resulted in an apparent backscattering cross section at 500 nm of $0.114 \pm 0.013 \mu\text{m}^2/\text{coccolith}$, in satisfactory agreement with the measured backscattering.

B. Light scattering by cylinders

Success with modeling scattering by *E. huxleyi* suggested more questions regarding the scattering of particles having more complex shapes. Of particular interest to me was the

scattering by particles showing extreme deviation from spheres, e.g., cylinders with large aspect ratios. This shape resembles that of long-chain phytoplankton. How do their scattering and absorption properties depend on the length, diameter, refractive index and internal structure of the cylinders? How do they depend on orientation? How do they compare to the scattering and absorption by spheres containing the same volume of material and absorbing pigment?

A principal result of the study (detailed in **Appendix 3**) is that the extinction, absorption, and scattering efficiencies, and the backscattering probability of randomly oriented, homogeneous and structured, cylinders become nearly independent of the aspect ratio (AR) when $AR > \sim 3$ -5, for refractive indices characteristic of marine particles (organic and inorganic). This applies to cylinders with diameters in the range 0.25 to 1.5 μm when illuminated with visible light (wavelength, 400-700 nm). Some long-chain phytoplankton, e.g., *Prochlorotrix hollandica*, fall in this size range. A limited number of computations for prolate spheroids suggest that the observations apply equally well to particles with this shape. This should simplify the inclusion of AR -distributions in the characterization of scattering by marine particles.

A second, and important result, was obtained from our simulation of the use of the equal-volume-sphere assumption in the analysis of extinction and absorption coefficient data for cylindrically-shaped particles obtained along with assumed measurements of particle volume to obtain the particle refractive index [Bricaud and Morel, 1986]. It was found that when this equal-volume-sphere assumption was used to try to estimate the complex refractive index of cylindrically shaped particles, the absorption index (imaginary part of the complex refractive index) could be determined with reasonable accuracy, i.e., $\sim \pm 20\%$, when the real part (m_r) was low, but m_r is usually underestimated. This is important as the absorption index of many species of phytoplankton have been estimated in this manner [Jonasz and Fournier, 2007]. When m_r is high, e.g., 1.20, the method fails completely. For the low index case, using the index retrieved through the equal-volume-sphere assumption, and computing backscattering cross section σ_{bb} for the equal-volume sphere, can lead to an underestimation ($\sigma_{bb}^{(Cyl)} > \sigma_{bb}^{(Sph)}$) of cylinder backscattering by a significant factor, largely because of the inaccuracy in the estimated value of m_r ; however, if the correct value of the refractive index is known, the error is significantly decreased. For the high-index case (for which the equal-volume-sphere analysis fails), given the correct value of the refractive index, the equal-volume sphere backscatters more than the cylinder, i.e., $\sigma_{bb}^{(Cyl)} < \sigma_{bb}^{(Sph)}$. Thus, prediction of σ_{bb} by this method for low index particles could account for some of the "missing" backscattering suggested for marine particles [Stramski et al., 2004]; however, when the correct index is used in the computations, the underestimation is greatly reduced or eliminated completely.

C. Observations regarding Rayleigh-Gans scattering

In earlier work [Gordon, 2006], it was discovered that the simple Rayleigh-Gans approximation (RGA) to scattering and backscattering of a thin disk compared favorably to the "exact" discrete dipole approximation (DDA). I was curious to see how well this approximation worked for particles of more complex shape, e.g., model coccoliths [Gordon and Du, 2001] or thin disks with small-scale periodic structure [Gordon, 2007].

It was found (details in **Appendix 4**) that as long as the thickness of the individual disks is approximately 20% of the wavelength (or less), the RGA agrees reasonably well quantitatively with the DDA even for disks with diameters much greater than the wavelength. Thus, the comparisons showed that the RGA is sufficiently accurate to be useful as a quantitative tool for exploring the backscattering features of disk-like particles with complex structure. It was used to show that, at least in lowest order, the neglect of birefringence on modeling the backscattering of detached coccoliths from *E. huxleyi*, would lead to error $< \text{about } \pm 10\%$ in the computed backscattering.

References

- A. Bricaud and A. Morel, Light attenuation and scattering by phytoplanktonic cells: a theoretical modeling, *Applied Optics*, **25**, 571—580 (1986)
- B.T. Draine, “The discrete-dipole approximation and its application to interstellar graphite grains,” *Astrophys. J.*, **333**: 848—872 (1988).
- B.T. Draine, and P. Flatau, “Discrete dipole approximation for scattering calculations,” *J. Opt. Soc. Am.*, **A11**, 1491–1499 (1994).
- H.R. Gordon, Backscattering of light from disk-like particles: is fine-scale structure or gross morphology more important?, *Applied Optics*, **45**(27), 7166-7173 (2006).
- H.R. Gordon, Backscattering of light from disk-like particles with aperiodic angular fine structure. *Optics Express*, **15**(25), 16424-16430 (2007).
- H.R. Gordon and Tao Du, Light scattering by nonspherical particles: application to coccoliths detached from *Emiliania huxleyi*, *Limnology and Oceanography*, **46**, 1438—1454, 2001.
- H.R. Gordon and A.Y. Morel, *Remote Assessment of Ocean Color for Interpretation of Satellite Visible Imagery: A Review*, Springer-Verlag, New York (1983) 114 pp.
- M. Jonasz and G. R. Fournier, *Light Scattering by Particles in Water, Theoretical and Experimental Foundations*, Academic Press (2007).
- D. Stramski, E. Boss, D. Bogucki, and K.J. Voss, “The role of seawater constituents in light backscattering in the ocean,” *Prog. Oceanogr.*, **61**, 27-56 (2004).

Appendix 1

“Backscattering of light from disk-like particles with aperiodic angular fine structure.” *Optics Express*, **15(25)**, 16424–16430 (2007).

Backscattering of light from disk-like particles with aperiodic angular fine structure

Howard R. Gordon

Department of Physics, University of Miami, Coral Gables, FL 33214.

Abstract: Recent computations of the backscattering cross section (σ_b) of randomly-oriented disk-like particles (refractive index, 1.20) with small-scale periodic angular internal structure, have been repeated for similarly sized particles, but with the periodic structure replaced by an *aperiodic* structure. The latter is formed by randomly perturbing a periodic structure. Although σ_b for individual realizations of an aperiodic disk can differ significantly from that of its periodic counterpart, averaging over several realizations brings the two into confluence, unless the aperiodicity is too large. These computations suggest that using disks with perfectly periodic (as opposed to quasi-periodic) fine structure for modeling the backscattering of detached coccoliths from *E. huxleyi* is justified.

© 2007 Optical Society of America

OCIS codes: (010.4450) Ocean optics; (290.1350) Backscattering.

References

1. H.R. Gordon and A.Y. Morel, *Remote Assessment of Ocean Color for Interpretation of Satellite Visible Imagery: A Review* (Springer-Verlag, 1983).
2. D. Stramski, E. Boss, D. Bogucki, and K.J. Voss, "The role of seawater constituents in light backscattering in the ocean," *Prog. Oceanogr.* **61**, 27-56 (2004).
3. M.I. Mishchenko, L.D. Travis, and A.A. Lacis, *Scattering, Absorption, and Emission of Light by Small Particles* (Cambridge, 2002).
4. H.R. Gordon and Tao Du, "Light scattering by nonspherical particles: application to coccoliths detached from *Emiliania huxleyi*," *Limnol. Oceanogr.* **46**, 1438-1454 (2001).
5. H.R. Gordon, "Backscattering of light from disk-like particles: is fine-scale structure or gross morphology more important?," *Appl. Opt.* **45**, 7166-7173 (2006).
6. B.T. Draine, "The discrete-dipole approximation and its application to interstellar graphite grains," *Astrophys. J.* **333**: 848-872 (1988).
7. B.T. Draine, and P. Flatau, "Discrete-dipole approximation for scattering calculations," *J. Opt. Soc. Am. A* **11**, 1491-1499 (1994).
8. H.R. Gordon, "Rayleigh-Gans scattering approximation: surprisingly useful for understanding backscattering from disk-like particles," *Opt. Express* **15**, 5572-5588 (2007).

1. Introduction

Interpretation of the light backscattered out of natural waters requires understanding the backscattering properties of their constituents [1]. However, the backscattering coefficient of marine particles is arguably the poorest known of the inherent optical properties of natural waters [2], and much effort is being focused on remedying this situation. The backscattering properties of marine particles are most-often modeled as homogeneous spheres using Mie theory. The advent of computer codes capable of handling more complex shapes [3], and the increased computational speeds now available, suggest that particle modeling employing simple non-spherical shapes, e.g., disks, rods, etc., will become routine. For example, Gordon and Du [4] used a two-disk model to try to reproduce the backscattering by coccoliths detached from *E. huxleyi*, which has a well-defined shape (resembling a disk or two roughly parallel disks) and a known composition (Calcite, refractive index relative to water ~ 1.20). (See Ref. 5 for scanning electron micrographs of *E. huxleyi* coccoliths.) However, *E. huxleyi*

in fact has a rather complex fine structure that might influence backscattering and should be addressed. I tried to examine this in an earlier paper [5], in which I computed the backscattering of light from thin micrometer-sized disks with periodic angular fine structure using the discrete-dipole approximation [6, 7]. The periodic fine structure was achieved by dividing the disk into equal-angle sectors of angle $\Delta\alpha = 2\pi/2^n$, and removing the dipoles from alternate sectors. In that study the diameter of the disks ranged from 1.50 to 2.75 μm and the thickness from 0.05 to 0.15 μm . The values used for n were 4, 5, 6, and 7, providing pinwheel-looking objects (Fig. 1) with 8, 16, 32, and 64 vanes, respectively. The principal result of the study was that when the scale of the periodicity, s (defined to be the length of an open or closed sector measured along the circumference of the disk), was $< \lambda/4$, where λ is the wavelength of the light in the medium (water) the backscattering was found to be nearly identical to that of a homogeneous disk possessing a reduced refractive index. In contrast, significant increases in backscattering were observed when the scale of the periodicity was greater than $\lambda/4$, reaching a maximum when the scale becomes $\sim \lambda/2$ [8]. However images of individual coccoliths [5] suggests that their "angular periodic" structure is not precisely periodic. This raises the question: how much does this aperiodicity influence the backscattering, or alternatively, how large must the deviation from periodic be in order to significantly influence the backscattering? I examine this question here by comparing the backscattering cross section of pinwheels with precisely periodic structure with that for pinwheels in which random variations in the angle $\Delta\alpha$ of individual sectors are introduced.

2. Model of an aperiodic pinwheel

The aperiodic pinwheel is formed by a perturbation of the purely periodic pinwheel effected in the following manner. First, the disk is divided into purely periodic sectors, the angular boundaries of which are designated by the 2^n angles α_p . The individual boundary angles are then perturbed to α_i according to

$$\alpha_i = \alpha_p + \varepsilon \frac{2\pi}{2^n} \rho,$$

where $0 \leq \varepsilon \leq 1$ is a constant and $-1/2 \leq \rho \leq 1/2$ is a random number with a uniform probability density. Then, the material of the disk is removed from ever other sector, yielding a pinwheel with a quasi-periodic structure. Four realizations (each based on a difference sequence of pseudorandom numbers) of such pinwheels for $n = 5$ are provided in Fig. 1 for $\varepsilon = 0.5$ and 1.0. Defining Σ_i to be the standard deviation in the angle α_i , we find $\Sigma_i = 12^{-1/2} \varepsilon \Delta\alpha \approx 0.3\varepsilon \Delta\alpha$, where $\Delta\alpha = 2\pi/2^n$. Likewise defining $\Sigma_{\Delta\alpha}$ to be the standard deviation of the removed (or occupied) sector angles, $\Sigma_{\Delta\alpha} = 6^{-1/2} \varepsilon \Delta\alpha \approx 0.4\varepsilon \Delta\alpha$. Thus, for $\varepsilon = 0.5$ and 1.0, the relative standard deviation in angle of the removed (or occupied) sectors is 20 and 40%, respectively. I examined two aperiodic pinwheels. The first has a diameter (D) of 1.50 μm , a thickness (t) of 0.15 μm , and $n = 5$ (Fig. 1). The second has $D = 2.75 \mu\text{m}$, $t = 0.05 \mu\text{m}$, and $n = 6$. The larger disk is similar in size to the distal shield of individual *E. huxleyi* coccoliths [5].

This method of creating aperiodic pinwheels does not yield structures with the same volume (mass) as the associated periodic pinwheel. The volumes of the four realizations of aperiodic pinwheels studied here are provided in Table 1. The individual realizations are labeled by the one minus the position in a string of pseudorandom numbers where the sampling for ρ begins. Thus, for realization 0000 the sampling begins with the first number, for realization 1000 it

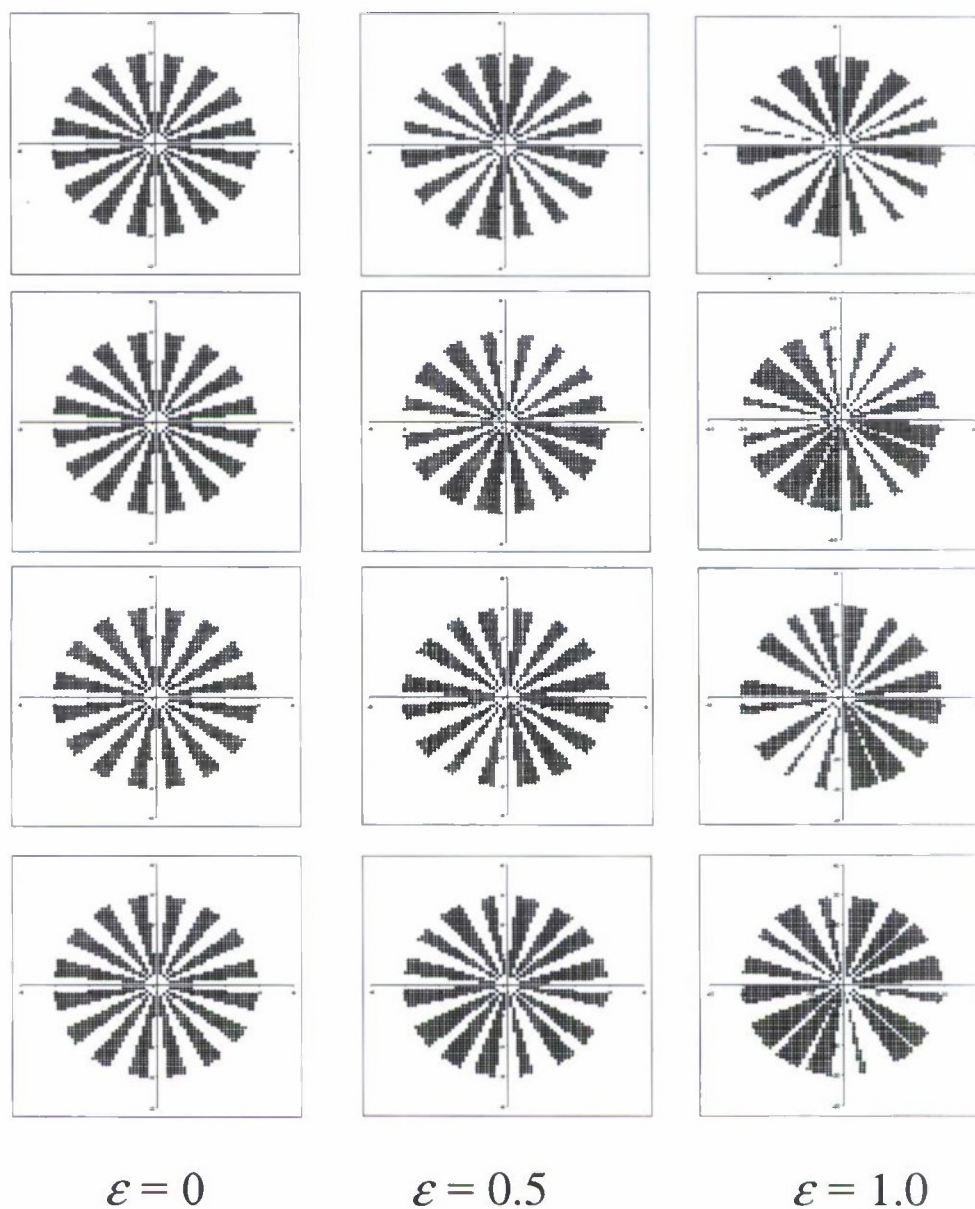


Fig. 1. The individual rows provide four realizations of the aperiodic pinwheels for $n = 5$ and various values of ε . Periodic pinwheels are shown in the first column.

begins with the 1001th number, etc. The variation of the volume for a given ε can be as much as 25% for the smaller ($D = 1.5 \mu\text{m}$, $n = 5$) and 7% for the larger ($D = 2.75 \mu\text{m}$, $n = 6$) pinwheels. The reduction in dispersion from the smaller to the larger is due to the increase in

n , which doubles the number of sectors, increasing the probability that the individual realizations have a volume closer to the mean.

3. Operation of the discrete-dipole scattering code

The scattering computations were carried out using the discrete-dipole approximation (DDA) [6, 7]. The accuracy of the DDA for randomly oriented particles is governed by two issues: (1) employing a sufficient number of dipoles to solve the electromagnetic scattering problem for a given orientation; and (2) employing a sufficient number of orientations for performing the orientational average. A measure of the number of dipoles is related to d , the spacing between the dipoles. One wants d to be substantially smaller than the wavelength.

Table 1. The volume (μm^3) of the two aperiodic pinwheels examined. The associated volumes for the periodic pinwheel ($\varepsilon = 0$) are $0.1325 \mu\text{m}^3$ and $0.1485 \mu\text{m}^3$ for the 1.5 and 2.75 μm diameter pinwheels, respectively. D is the diameter and t is the thickness of the associated disk.

ε	$D = 1.50 \mu\text{m}, t = 0.15 \mu\text{m}, n = 5$				$D = 2.75 \mu\text{m}, t = 0.05 \mu\text{m}, n = 6$			
	Realization				Realization			
	0000	1000	2000	3000	0000	1000	2000	3000
0.5	0.1221	0.1359	0.1319	0.1389	—	—	—	—
1.0	0.1119	0.1400	0.1285	0.1459	0.1383	0.1490	0.1472	0.1470

The smaller d , the more dipoles are required to fill the volume of the particle. A convenient measure of the spacing in regard to the wavelength is $|m|kd$, where m is the refractive index and $k = 2\pi/\lambda$. The orientation of a disk-like object is specified by three angles: θ the angle the axis of the disk makes with the incident beam, ϕ , the azimuth of the axis relative to a laboratory-fixed plane containing the incident beam, and β , the angle of rotation around the axis required to place the disk in a specified orientation given θ and ϕ . In general, for an object with no rotational symmetry, e.g., an aperiodic pinwheel, $0^\circ \leq \theta \leq 180^\circ$, $0^\circ \leq \phi \leq 360^\circ$ and $0^\circ \leq \beta \leq 360^\circ$; however, the high symmetry of a uniform disk reduces these to $0^\circ \leq \theta \leq 90^\circ$, $0^\circ \leq \phi \leq 180^\circ$, and requires only one value of β , e.g., $\beta = 0$. For periodic pinwheels ($\varepsilon = 0$) the angle β is required, however, its range need only be enough to completely cover one open sector and one adjacent occupied sector. The DDA code performs orientational averaging by computing the scattering at discrete angles equally spaced in ϕ and β , while the angle θ is divided in uniform increments of $\cos\theta$. An important consideration in the averaging is that the computation time is roughly proportional to the number of angles ($N_\theta \times N_\phi \times N_\beta$) used in the averaging.

Gordon and Du [8] showed that for a homogeneous disk with $D = 2.7 \mu\text{m}$ using ~ 5000 orientations ($N_\theta = 51$, $N_\phi = 99$, $N_\beta = 1$) for the orientational average, the error in the backscattering cross section (σ_b) was of the order of 5% for $|m|kd < 0.5$, and decreased rapidly for smaller values of $|m|kd$. In the present work, I have always used enough dipoles to keep $|m|kd < 0.5$ (and often < 0.4) and a number of orientations that would provide approximately the same averaging accuracy as the uniform disk with $D = 2.7 \mu\text{m}$. For the periodic pinwheels I used $N_\theta = 51$, $N_\phi = 99$ and $N_\beta = 4$. The four β increments were equally spaced over one open sector and an adjacent occupied sector. Because of the symmetry, this would be equivalent to choosing $N_\beta = 128$ and $0^\circ \leq \beta \leq 360^\circ$. For the aperiodic pinwheels (with $\varepsilon = 1$), I used $N_\theta = 101$, $N_\phi = 99$ and $N_\beta = 9$. These latter orientations were chosen by extensive testing in which I examined the differential scattering cross section for scattering angles $\Theta > 90^\circ$. The region $120^\circ \leq \Theta \leq 180^\circ$, the phase functions of periodic and aperiodic pinwheels ($D = 2.75 \mu\text{m}$) are highly oscillatory in Θ , and for the above choice of the orientational averaging, the observed oscillations in the periodic and aperiodic cases were similar, facilitating a fair comparison

between the two. Actually, σ_b appears to become stable with smaller values of N_θ , N_ϕ and N_β , where the orientationally-averaged phase function becomes more strongly dependent on the number of orientations, providing confidence that a sufficient number of orientations have been used. In the final analysis, the choice of the number of orientations must be balanced against computational time required.

4. Results of the computations

Figures 2 and 3 provide the results of the backscattering cross section computations for the smaller and larger pinwheels, respectively. Also shown for comparison is the result for a homogeneous disk of the same size (D and t). Note that the homogeneous disk has twice the volume (mass) of the periodic pinwheel ($\varepsilon = 0$) and approximately twice the volume of the aperiodic pinwheels ($\varepsilon > 0$).

Consider first the periodic pinwheels. For these, $s = \lambda/4$ occurs when $t/\lambda = 0.255$ for the smaller and 0.093 for the larger pinwheel. For t/λ larger than these values, the backscattering increases rapidly with decreasing λ and then undergoes a series of maxima and minima with progressively increasing backscattering at each maximum. The backscattering at the maxima for the smaller pinwheel is, in magnitude, approximately that at the maxima for the homogeneous disk (twice the volume or mass of the pinwheel). For the larger pinwheel, it is approximately 75% of the maxima for a uniform disk. These pinwheel maxima are the result of interference of the fields scattered by the individual vanes of the pinwheel as they occur in the Rayleigh-Gans approximation as well (although only the first maximum occurs at the

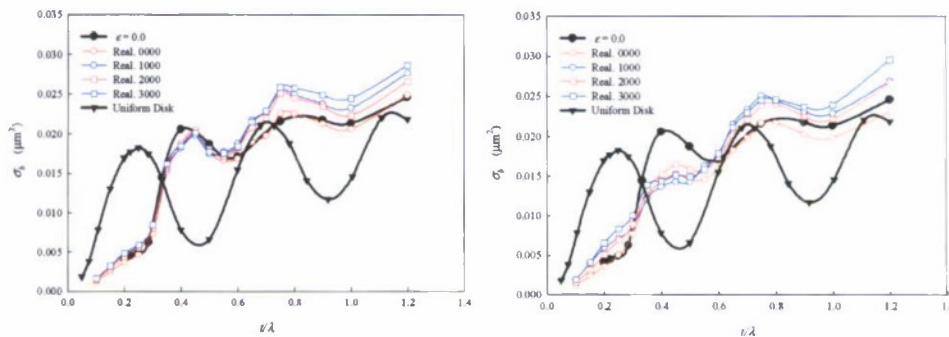


Fig. 2. The backscattering cross section of four realizations of the aperiodic pinwheels shown in Fig.1 ($D = 1.5 \mu\text{m}$) compared with that for a periodic pinwheel and for a homogeneous disk of the same size. The left panel is for $\varepsilon = 0.5$ and the right panel is for $\varepsilon = 1.0$.

same position [8]). In the case of the smaller aperiodic pinwheel, when $\varepsilon = 0.5$ its backscattering closely follows the periodic pinwheel, with the dispersion of backscattering reaching 20% at the smallest wavelength, while when $\varepsilon = 1.0$ there is more significant deviation from the periodic case, and the dispersion is somewhat larger. Recalling that $\Sigma_{\Delta\alpha} \approx 0.4\varepsilon \Delta\alpha = 0.4 \times 2\pi\varepsilon/2^n$, we note that the smaller pinwheel with $\varepsilon = 0.5$ ($n = 5$) has the same value of $\Sigma_{\Delta\alpha}$ as the larger pinwheel with $\varepsilon = 1.0$ ($n = 6$). Interestingly, Figs. 2 (Left Panel) and 3 show that the behavior of σ_b with decreasing λ up to its first minimum are similar in the two cases ($\varepsilon = 0.5$, $n = 5$ and $\varepsilon = 1.0$, $n = 6$): there are only minor deviations from the periodic pinwheels; and there is small dispersion between the various realizations of the aperiodic pinwheels. In contrast, when ε is increased from 0.5 to 1.0 for the smaller pinwheel, the

dispersion increases, and σ_b near its first maximum ($t/\lambda \approx 0.4$) shows a significant decrease from the $\varepsilon = 0$ and 0.5 cases. This behavior would be expected under the hypothesis that the maxima in the periodic case results from constructive interference of light interacting with the individual vanes of the pinwheel – when the spacing and angular size of the vanes

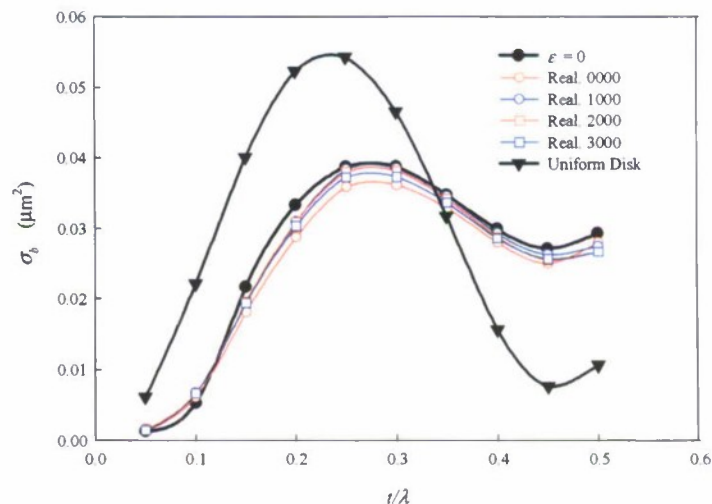


Fig. 3. The backscattering cross section of four realizations of the aperiodic pinwheels with $\varepsilon = 1.0$, $D = 2.75 \mu\text{m}$ and $n = 6$ compared with that for the associated periodic pinwheel.

becomes random the constructive interference is reduced.

Close examination of Fig. 2 at the smaller wavelengths reveals that σ_b for the several realizations is ordered with increasing volume, i.e., the realization with the smallest σ_b has the smallest volume, etc. However, with increasing λ (decreasing t/λ) the order can reverse, particularly near the first maximum near $t/\lambda \approx 0.4$. Thus, there is no way to try to reduce the dispersion throughout the whole wavelength range by normalizing for volume differences. In the Rayleigh-Gans domain, $t/\lambda < 0.2$ [8], for particles with identical shape, the volume effect on σ_b is proportional to the square of the volume. This would explain the envelope of the variation near $t/\lambda = 0.2$ in Fig. 2.

Although the volume effect cannot be removed, it is important to understand that real biological particles (e.g., *E. huxleyi* coccoliths) would display similar variations in volume. In fact, if pinwheels were to represent real biological particles, samples would be expected to consist of a number of realizations of their aperiodicity. In this regard, the average σ_b (denoted by $\langle \sigma_b \rangle$) is more important than that for any given realization. Figure 4 compares the $\langle \sigma_b \rangle$ for the four realizations of the aperiodicity examined here with the associated periodic pinwheel. It clearly shows that the main difference between $\langle \sigma_b \rangle$ for the small periodic and aperiodic pinwheels (left panel) occurs near the maxima in the backscattering, and that near the first maximum (but not the second) the difference increases as deviation from periodicity increases (i.e., as ε increases). Considering the large departures from periodicity for the $\varepsilon = 1$ realizations in Fig. 1, it is remarkable that, when averaged over realizations, their $\langle \sigma_b \rangle$ is so close to that of periodic pinwheels ($\varepsilon = 0$). As suggested in Fig. 3, Fig. 4 (right panel) shows that the $\langle \sigma_b \rangle$ for the large aperiodic pinwheel is very close to its periodic counterpart.

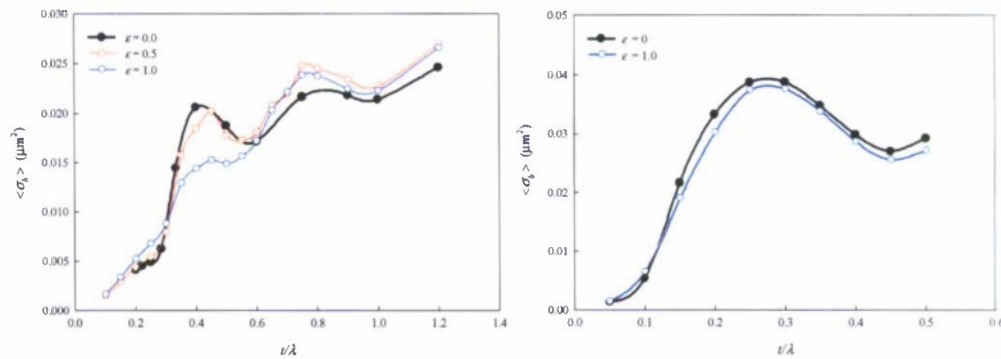


Fig. 4. The backscattering cross section $\langle \sigma_b \rangle$ of an equal-number mixture of the four realizations of the aperiodic pinwheels compared with that for a periodic pinwheel ($\epsilon = 0$): left panel $D = 1.5 \mu\text{m}$, $t = 0.15 \mu\text{m}$ and $n = 5$; right panel $D = 2.75 \mu\text{m}$, $t = 0.05 \mu\text{m}$ and $n = 6$.

5. Discussion

With only two examples of periodic pinwheels and their aperiodic counterparts, it is difficult to make concrete conclusions regarding the effects of aperiodicity. However, it does appear that some general conclusions are possible. First, Figs. 2 and 3 show that in the transition from the periodic to the aperiodic pinwheel σ_b changes much less than compared to the transition from uniform disk to periodic pinwheel. Second, the dispersion in σ_b among realizations of the aperiodic pinwheels is associated with the dispersion in $\Delta\alpha$ (or s), which increases with increasing ϵ . Third, the aperiodic $\langle \sigma_b \rangle$ will usually be somewhat smaller than the periodic σ_b , at least near the position of the first (long-wave) maximum, and this decrease increases with increasing aperiodicity (ϵ).

Finally, I examined the deviation in the angular spacing of the “spokes” in the distal shield of the individual coccoliths provided in Fig. 2 of reference [8]. For this particular coccolith, $\Sigma_{\Delta\alpha}/\Delta\alpha \sim 0.27$, and there were 40 open angular sectors. This coccolith shield is similar in size and shape to the larger ($2.75 \mu\text{m}$) pinwheel ($n = 6$, 32 open sectors) examined here. The computations for the larger pinwheel show that, for the purpose of computing backscattering, the periodic pinwheel is a good approximation to aperiodic pinwheel as long as $\Sigma_{\Delta\alpha}/\Delta\alpha \leq 0.4$ ($\epsilon \leq 1$). This suggests that replacing the aperiodic fine structure of the distal shield of *E. huxleyi* coccoliths with a strictly periodic fine structure will not degrade the modeling of their backscattering, especially for natural samples containing large numbers of coccoliths.

Acknowledgments

The author is indebted to K. Voss for many useful discussions, B. Draine and P. Flatau for providing their DDA code, and the Office of Naval Research for support under Grant Number N000140710226.

Appendix 2

“Light scattering by coccoliths detached from *Emiliana huxleyi*,” *Applied Optics*, **48**, 6059–6073 (2009).

Light scattering by coccoliths detached from *Emiliania huxleyi*

Howard R. Gordon,^{1,*} Timothy J. Smyth,² William M. Balch,³
G. Chris Boynton,¹ and Glen A. Tarran²

¹Department of Physics, University of Miami, Coral Gables, Florida 33124, USA

²Plymouth Marine Laboratory, Prospect Place, Plymouth, Devon, PL1 3DH, UK

³Bigelow Laboratory for Ocean Sciences, POB 475, West Boothbay Harbor, Maine 04575, USA

*Corresponding author: hgordon@miami.edu

Received 30 June 2009; revised 7 October 2009; accepted 9 October 2009;
posted 9 October 2009 (Doc. ID 113499); published 28 October 2009

We used *in situ* radiance/irradiance profiles to retrieve profiles of the spectral backscattering coefficient for all particles in an *E. huxleyi* coccolithophore bloom off the coast of Plymouth, UK. At high detached coccolith concentrations the spectra of backscattering all showed a minimum near ~550 to 600 nm. Using flow cytometry estimates of the detached coccolith concentration, and assuming all of the backscattering (over and above the backscattering by the water itself) was due to detached coccoliths, we determined the upper limit of the backscattering cross section (σ_b) of individual coccoliths to be $0.123 \pm 0.039 \mu\text{m}^2/\text{coccolith}$ at 500 nm. Physical models of detached coccoliths were then developed and the discrete dipole approximation was used to compute their average backscattering cross section in random orientation. The result was $0.092 \mu\text{m}^2$ at 500 nm, with the computed σ_b displaying a spectral shape similar to the measurements, but with less apparent increase in backscattering toward the red. When σ_b is computed on a per mole of calcite, rather than a per coccolith basis, it agreed reasonably well with that determined for acid-labile backscattering at 632 nm averaged over several species of cultured calcifying algae. Intact coccolithophore cells were taken into account by arguing that coccoliths attached to coccolithophore cells (forming a "coccosphere") backscatter in a manner similar to free coccoliths in random orientation. Estimating the number of coccoliths per coccosphere and using the observed number of coccolithophore cells resulted in an apparent backscattering cross section at 500 nm of $0.114 \pm 0.013 \mu\text{m}^2/\text{coccolith}$, in satisfactory agreement with the measured backscattering. © 2009 Optical Society of America

OCIS codes: 010.4450, 290.5850, 000.1430, 280.4991.

1. Introduction

Understanding the optical properties of marine particles is important in oceanographic studies ranging from using light attenuation to determine and monitor sediment transport [1], to the estimation of the energy available for photosynthesis [2] and the efficiency with which photosynthetic organisms can utilize the available energy [3], to the interpretation of the color of the water as observed from space [4]. In

the past, much effort has been expended in modeling the absorption and scattering properties of marine particles in terms of their chemical and physical properties, such as size, pigment composition, refractive index, etc. [5–7]. In most studies the particles are assumed to be spherically symmetric. The focus of this work is modeling the scattering by single marine particles: coccoliths detached from the coccolithophorid *Emiliania huxleyi*. The goal is to understand the extent to which complex particle shape must be considered to properly model light scattering by marine particles.

The fundamental inherent optical properties (IOPs) of a suspension of particles are the absorption coefficient a and the volume scattering function (VSF) $\beta(\Theta)$. When a parallel beam of light power P_0 propagates a distance $\Delta\ell$ through the suspension, an amount of radiant power ΔP_a is lost through absorption and an amount $\Delta^2 P_s(\Theta)$ is removed through scattering into a solid angle $\Delta\Omega$ around a direction making an angle Θ (the scattering angle) with the original direction of propagation. The absorption coefficient and the VSF are defined through

$$a = \frac{1}{P_0} \frac{\Delta P_a}{\Delta\ell} \quad \text{and} \quad \beta(\Theta) = \frac{1}{P_0} \frac{\Delta^2 P_s(\Theta)}{\Delta\Omega \Delta\ell}. \quad (1)$$

The total scattering coefficient b relates to the total power lost by scattering in all directions:

$$b = \frac{1}{P_0} \frac{\Delta P_s}{\Delta\ell} = 2\pi \int_0^\pi \beta(\Theta) \sin \Theta d\Theta, \quad (2)$$

where it has been implicitly assumed that the scattering is independent of the azimuth angle around the beam propagation direction, i.e., if the propagation is in the z direction, the power scattered in the x direction is the same as that scattered in the y direction, etc., and requires that if the particles are nonspherical they be in random orientation. The backscattering coefficient b_b relates to the power lost through scattering in the angular range $\pi/2 \leq \Theta \leq \pi$:

$$b_b = 2\pi \int_{\pi/2}^\pi \beta(\Theta) \sin \Theta d\Theta. \quad (3)$$

If the particles in the suspension are all identical, the total scattering cross section (σ) and the backscattering cross section (σ_b) of an individual particle are given by

$$b = N\sigma \quad \text{and} \quad b_b = N\sigma_b, \quad (4)$$

where N is the number density (number per unit volume) of particles in the suspension. If there are n species of particles present, the IOPs are linearly additive over the species, i.e., $b = \sum_{i=1}^n b_i$, etc. Because of its importance in ocean remote sensing (the solar radiation backscattered out of the water toward a remote sensor is $\propto b_b/a$), our focus will be mostly on b_b (actually σ_b).

The IOPs of marine particles are most often modeled assuming that they are homogeneous spheres. Although this approach has been fruitful for several decades, the next logical step in modeling marine-particle optics is to abandon the spherical assumption and use more realistic approximations to their shape. Clavano *et al.* [8] provide an excellent discussion of scattering by nonspherical particles with refractive indices similar to those of marine particles.

They focused on spheroids and found significant differences between the scattering by equal-volume spheroids and spheres, particularly in the backscattering cross sections.

Microscopic examination of marine particles reveals inhomogeneous particles of various shapes, with the larger particles often having shapes with extreme aspect ratios, e.g., long, thin cylinders, etc., and a very inhomogeneous structure. The particles that are of organic origin also contain pigments that are absorbing in the visible. Separating the effects of shape from those of absorption and inhomogeneity in such complex particles presents a very difficult problem. Thus, to test the viability of modeling light scattering by marine particles using more realistic approximations to their shape, it is important to find a particle for which light absorption is unimportant, so the influence of shape is expected to be the dominant effect in modeling its light scattering. Such particles are the detached coccoliths from the coccolithophorid *E. huxleyi*. This particle is ideal as a case study for shape effects in marine light-scattering modeling for a variety of reasons. First, it is homogeneous and its composition is known (calcite), providing its refractive index. Second, its gross shape is known (it resembles a disk or two parallel disks), although, it does have complex, quasi-periodic internal structure at the sub-visible-wavelength scale that must be addressed. Next, although coccolithophore cells absorb light, the detached coccoliths are nonabsorbing, so the problem of unraveling absorption effects from shape effects is circumvented. Finally, *E. huxleyi* is important in biogeochemical processes as it is ubiquitous in the world oceans and contributes significantly to the ballasting of marine particulate matter, hence the vertical transport of both organic and inorganic carbon from the surface waters to the sediments. In addition, when a large *E. huxleyi* bloom occurs and large numbers of coccoliths are detached from the parent cells, it is easily observed from space and therefore amenable to ocean color remote sensing techniques as a means of estimating the concentration and eventually its global impact on the carbon cycle [9]. Because of the importance of backscattering in remote sensing (and the absence of coccolith absorption), the backscattering of detached coccoliths is arguably their most important optical property.

It is now possible to efficiently compute the absorption and scattering properties of homogeneous particles of many simple shapes using the T -matrix method [10]. A less efficient method of computation, the discrete-dipole approximation (DDA), can be used to compute the absorption and scattering properties of particles of any shape [11]; however, the computations are time consuming. Gordon and Du [12] used the DDA to model the scattering by detached coccoliths using simple disklike shapes. They found that the spectral shape of backscattering by detached coccoliths in the blue-green could be reasonably well reproduced using a shape consisting of two parallel

disks (diameter $\sim 2.75\ \mu\text{m}$ and thickness $0.05\ \mu\text{m}$) separated by $0.3\ \mu\text{m}$, but the absolute magnitude of the backscattering cross section of an individual coccolith was significantly smaller than observed (factor of 2 to 3). Further modeling required more complete measurement of the backscattering properties of detached coccoliths. The difficulty in obtaining such data is the fact that coccolith blooms, although somewhat frequent in certain areas, are ephemeral in nature, making it difficult to plan a field program for sampling, even with the timely availability of satellite imagery.

A unique dataset for a better understanding of the optical properties of detached coccoliths presents itself through the measurements carried out by Smyth *et al.* [13] in a coccolithophore bloom off the coast of Plymouth, England during July 1999. In this field experiment, detailed in-water optical measurements were carried out in an intense bloom. In addition, imagery from the ocean color sensor SeaWiFS [14] is available for the same bloom [15]. In this report, these data are used to extend the light-scattering modeling of detached coccoliths started by Gordon and Du [12].

The structure of the paper is as follows. First, we describe the data set acquired by Smyth *et al.* [13]. Second, we validate the inverse radiative transfer method for deriving the absorption and backscattering coefficient profiles (to be used with coccolith profiles) from profiles of the downwelling irradiance and the upwelling radiance within an artificial coccolithophore bloom (a turbid chalk suspension). Third, we apply the inversion algorithm to the Plymouth bloom and derive spectra of the absorption coefficient (a) and the backscattering coefficient (b_b) as a function of the concentration of detached coccoliths. Fourth, we present the absorption and backscattering coefficients retrieved from the SeaWiFS imagery at the same locations as a demonstration of the fidelity of the in-water inversions. Fifth, we develop an advanced physical model of a coccolith and use the DDA to deduce its scattering properties. Sixth, we attempt to model the influence of intact coccolithophore cells on the apparent backscattering cross section of detached coccoliths. Finally, we compare the modeled spectral backscattering cross section to the measurements and discuss the results.

2. The Data Set

The in-water data used in this paper are those reported by Smyth *et al.* [13]. Briefly, they include profiles of the upwelling radiance (propagating toward the zenith), $L_u(\lambda)$, and the downwelling irradiance, $E_d(\lambda)$, obtained at $\lambda = 412, 443, 490, 510, 555, 620$, and $685\ \text{nm}$ using radiometers engineered by Satlantic following SeaWiFS protocols [16]. The concentration of coccolithophore cells and detached coccoliths were determined from water samples in two ways: direct manual counting of samples preserved in buffered formalin; and flow cytometry of fresh (live) samples. The detached coccolith counts in the pre-

served samples differed by approximately a factor of two from the flow cytometrically derived values. This is believed to be due to the fact that cells preserved in buffered formalin for manual counting were observed to shed their coccoliths in storage. (This difference between preserved and fresh samples is discussed more thoroughly in Section 4.) The optics of the blooms was dominated by detached coccoliths with as many as 235 coccoliths observed for each intact coccolithophore cell. Embedded within parts of the bloom were red patches of *Gymnodinium mikimotoi* that were apparent from SeaWiFS imagery recorded on the same day, observed by other mariners (and one of us, T. Smyth, from a cruise a week earlier), but none were apparent at the stations described here.

The Station locations are labeled 1–4 in order of increasing coccolith concentration. Their locations can be found on Fig. 1 of Gordon *et al.* [15] or Smyth *et al.* [13]. Station 1 was believed to be out of the bloom (and usable for background optical properties); however the *in-situ* samples revealed that coccoliths were present, albeit at a concentration that was an order of magnitude lower near the surface than the other stations. Because the $L_u(\lambda)$ sensor saturated near the surface, due to the intense backscattering, complete depth profiles are not available. At $555\ \text{nm}$ the usable $L_u(\lambda)$ measurements start at 3, 3, and $4\ \text{m}$ for Station 2, 3, and 4, respectively [13].

In addition to the in-water data, imagery from the ocean color scanner SeaWiFS is also available. The SeaWiFS overpass was coincident with Station 3. Gordon *et al.* [15] used this SeaWiFS image to estimate the coccolith concentration in the bloom in question. (It should be noted that the remote and *in-situ* coccolith concentrations in Gordon *et al.* [15] are roughly double the counts stated in Smyth *et al.* [13] because manual counts of buffered formalin-preserved samples were used in [15], as well as for the empirical relationship between backscattering and number density.)

3. Validation of the Inversion Algorithm for Backscattering

The spectral backscattering coefficient is to be retrieved from the field data using the inversion algorithm developed by Gordon and Boynton [17]. The Gordon and Boynton algorithm uses vertical profiles of L_u and E_d to estimate vertical profiles of a and b_b . Briefly, trial profiles of $a(z)$ and $b_b(z)$, where z is depth, are introduced into the radiative transfer equation (RTE), which is solved to provide estimates of $L_u(z)$ and $E_d(z)$. These estimates are compared with their measured counterparts, and based on the differences, the a and b_b profiles are adjusted and re-introduced into the RTE, which is again solved for $L_u(z)$ and $E_d(z)$. This process continues iteratively until a satisfactory agreement between the measured and calculated $L_u(z)$ and $E_d(z)$ is obtained, and the resulting $a(z)$ and $b_b(z)$ are the “retrieved” quantities. As Gordon [18] has shown that $L_u(z)$

and $E_d(z)$ are insensitive to b , the resulting values of $b(z)$ are discarded; however, the $b_b(z)$ profile is retained.

The solution of the RTE between each iteration, requires a scattering phase function for the medium. Here, we use the phase function measured by Petzold [19,20]. Gordon and Boynton [17] show, using simulations in which synthetic irradiance-radiance data were created with forward radiative transfer using a phase function with backscattering probability equal to 0.036, that the depth-averaged error in the inversion-retrieved backscattering coefficient when the correct phase function was used in the retrieval was $\lesssim 2\%$ while, if an incorrect phase function (one with a backscattering probability equal to 0.011) was used, the error was usually $< 8\%$.

In the adjustment of the trial $b_b(z)$ from one iteration of the algorithm to the next, a relationship between $b_b(z)/a(z)$, $L_u(z)/E_d(z)$, and the depth derivative of $L_u(z)/E_d(z)$ is used to relate $b_b(z)/a(z)$ at depth z to that at greater depths, and accounts for the influence of vertical structure on the IOPs. Although newer approximations are available to account for the influence of vertical structure on $L_u(z)/E_d(z)$ [21,22], the Gordon and Boynton algorithm employs the earlier method of Gordon and Clark [23]. The validation of the algorithm described below will show that use of the older Gordon and Clark method does not lead to excessive error except, possibility in the depth range over which backscattering is changing rapidly with depth.

In contrast to oligotrophic and mesotrophic waters [24], for which the inversion error in $b_b(z)$ compared to *in-situ* measurements is $\sim 8\%$, the inversion algorithm has not been validated for the case of highly-scattering waters. To effect a validation, we used spectral backscattering and absorption data obtained in conjunction with vertical profiles of $L_u(\lambda)$ and $E_d(\lambda)$ obtained during the Chalk-Ex experiment [25]. In Chalk-Ex, a turbid patch resembling a coccolithophore bloom, was created at $39.79^\circ\text{N} \times 67.77^\circ\text{W}$, on 15 November 2001, by mixing $2\mu\text{m}$ particles of ground Cretaceous chalk (calcite) into surface seawater. The strong correlation between particle backscattering and chalk mass allowed the fate of the chalk to be tracked spatially over time scales of several days. Figure 1 shows the resulting patch, which began as a 3 km^2 feature (which quantitatively and qualitatively resembled a coccolithophore bloom in terms of its color and quantity of reflected light). Note, due to small-scale physical processes, the feature was not horizontally homogeneous but showed heterogeneities consistent with Langmuir circulation [25]. For the data presented here, from the initial stages of the deployment, the chalk feature was confined to approximately the top 15 m of the water column. Measurements of $L_u(\lambda)$ and $E_d(\lambda)$ were obtained with a Satlantic Ocean Color Profiler (OCP) at seven visible wavelengths. Optical profiles were made ± 2 hours of local apparent noon. The OCP instrument was slightly nega-

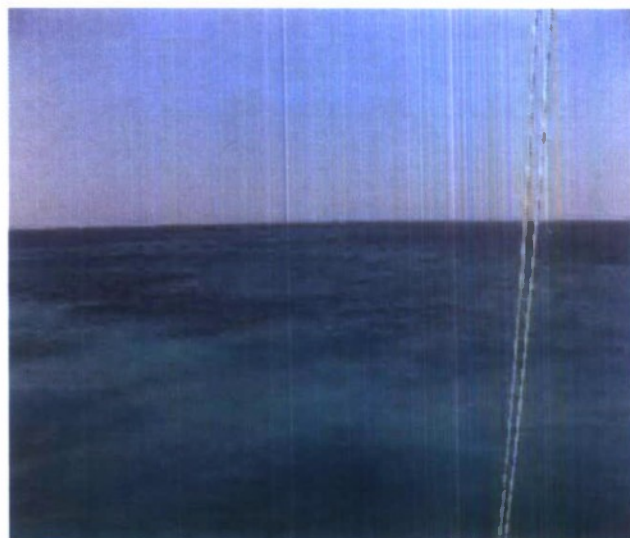


Fig. 1. (Color online) Chalk-Ex campaign: The synthetic "bloom" resulting from the deployment of finely ground chalk particles (mean diameter, $2\mu\text{m}$). Note the horizontal inhomogeneity.

tively buoyant and was deployed by hand, behind the ship, (oriented such that the Sun was aft of the ship, which was steaming at $\sim 25\text{ cm s}^{-1}$). This orientation avoided ship shadow. Once the OCP trailed 100 m aft of the ship, the cable to the OCP was released so the instrument could sink vertically over the top 100 m at a velocity of 1 m s^{-1} . The measurement of $b_b(\lambda)$ was made at two wavelengths using a HoboLabs Hydroscat-II (470 and 676 nm) calibrated according to the manufacturer. Although the particles in this artificial bloom are neither the same shape nor size of detached coccoliths (they are somewhat smaller and irregular in shape), they do provide what is needed to validate the inversion algorithm: a high concentration of nonabsorbing particles.

The $L_u(\lambda)$ and $E_d(\lambda)$ Chalk-Ex data were introduced into the Gordon and Boynton [17] inversion code and vertical profiles of $a(z)$ and $b_b(\lambda)$ were retrieved. This code version could be used with confidence because both Rayleigh and Raman scattering by the water itself are negligible compared to the scattering by the chalk particles; however, in the before-dispersal case the low backscattering may require additional consideration. Figures 2 and 3 compare the measured $b_b(470\text{ nm})$ with the retrieved $b_b(490\text{ nm})$ both before and after the chalk dispersal. In the chalk-free retrieval, the retrieved $b_b(490\text{ nm})$ appears to be about 10–20% lower than the measured $b_b(470\text{ nm})$. Part of this difference is likely due to the fact that the backscattering of water is significant and the Boynton and Gordon [26] version of the algorithm would be more appropriate for this case. The significant difference seen just near the surface is likely due to the influence of surface waves on the irradiance measurements. The after-dispersal results (Fig. 3) show roughly an order of magnitude more backscattering in a layer extending from the surface to about 15 m. The difference between the up and down casts reflects the horizontal inhomogeneity

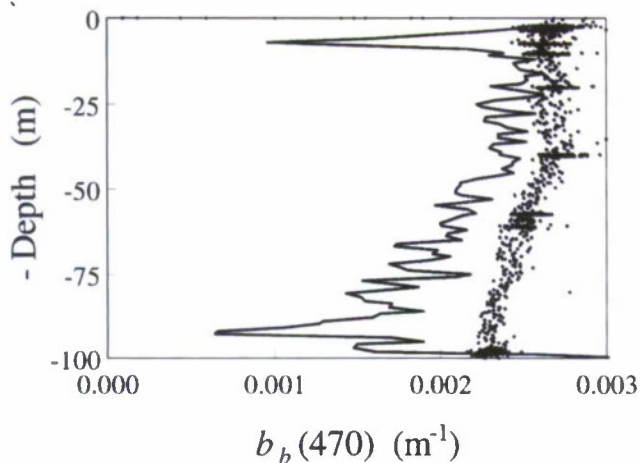


Fig. 2. Measured backscattering coefficient at 470 nm at the Chalk-Ex site (given in the text) before dispersal of the chalk (points) and retrieved backscattering at 490 nm using the inversion algorithm (continuous curve).

of the chalk patch. The retrieved $b_b(490 \text{ nm})$ in the high-concentration layer appears to differ from the measured $b_b(470 \text{ nm})$ by about $\pm 25\%$; however, some of this difference is due to the inhomogeneity of the patch. These retrievals suggest that the error in the retrieved $b_b(490 \text{ nm})$ should be less than $\pm 25\%$ in the high-concentration portions of the patch.

As an additional test of the performance of the retrieval algorithm, we examine the retrieved absorption coefficients before and after dispersal of the chalk. The absorption coefficients before and after dispersal should be the same because the chalk was nonabsorbing. Comparison of the average retrieved spectral absorption coefficients in the region of the high concentration of the chalk before and after dispersal is provided in Fig. 4. Clearly, there is no significant difference in the quality of the performance of the algorithm in retrieving the absorption coefficient induced by the addition of the chalk to the water.

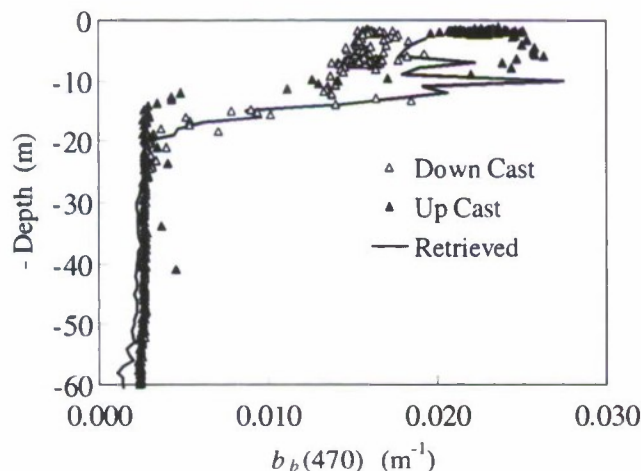


Fig. 3. Measured backscattering coefficient at 470 nm at the Chalk-Ex site after the dispersal of the chalk (points) and retrieved backscattering at 490 nm using the inversion algorithm (continuous curve).

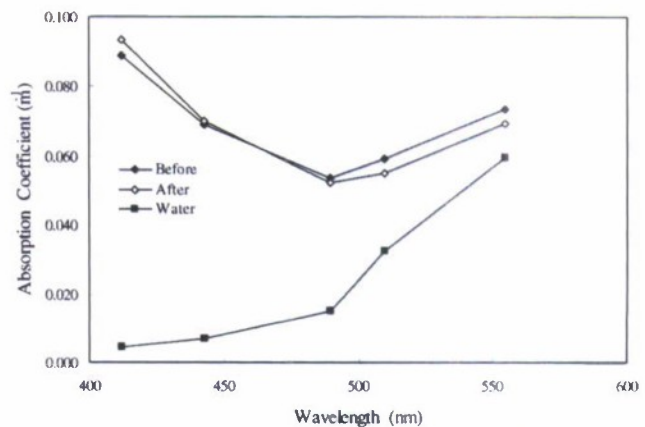


Fig. 4. Retrieved absorption coefficient at the Chalk-Ex site before and after dispersal of the chalk over the depth range of high concentrations of chalk (top $\sim 20 \text{ m}$).

Based on the Chalk-Ex retrievals, we believe that the retrieved backscattering coefficients in the high-concentration parts of the coccolithophore blooms we examine will be in error by certainly no more than $\pm 25\%$ and probably substantially less, as coccolithophore blooms are much more spatially uniform than the Chalk-Ex patch.

4. Results of the Inversion of Coccolithophore Bloom Data

Here we first provide the examples of the retrieved spectra of $a(\lambda)$ and $b_b(\lambda)$, then use the SeaWiFS imagery to support the validity of the retrievals, and finally, estimate the backscattering cross section ($\sigma_b \equiv b_b/N_{\text{Coccolith}}$, where $N_{\text{Coccolith}}$ is the concentration of detached coccoliths in the water).

A. Retrieval of $a(\lambda)$ and $b_b(\lambda)$ from the In-Water Measurements

The inversion algorithm was applied to the $L_u(\lambda)$ and $E_d(\lambda)$ depth profiles to retrieve depth profiles of $a(\lambda)$ and $b_b(\lambda)$. The retrieved values of $a(\lambda) - a_w(\lambda)$ and $b_b(\lambda)$ at a depth of 5 m are provided in Figs. 5 and 6. In Fig. 5, the value at 685 nm is omitted because it is negative in half the stations. The average absolute value in $a(685) - a_w(685)$ is 0.06 m^{-1} , while $a_w(685) = 0.486$, which suggests the retrieval error in $a(685)$

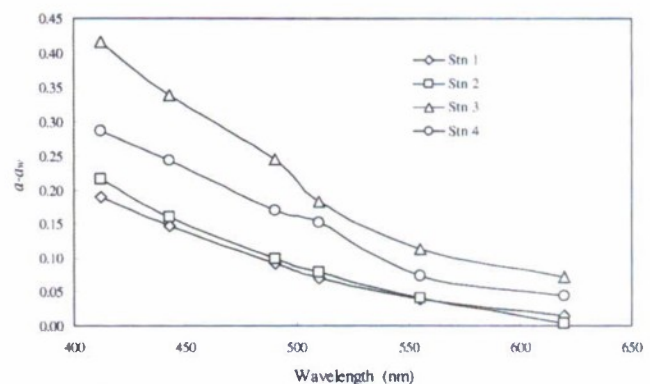


Fig. 5. Retrieved absorption coefficient minus that of water (a_w) at the Stations 1–4 in the Plymouth bloom at 5 m depth.

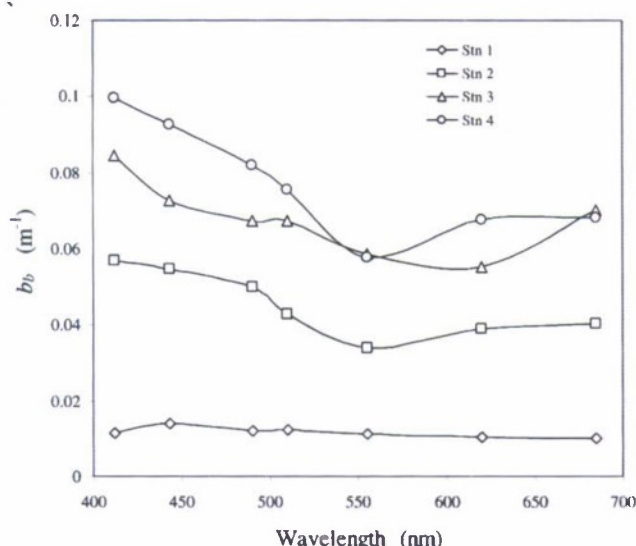


Fig. 6. Retrieved backscattering coefficient at Stations 1–4 in the Plymouth bloom at 5 m depth.

is less than $\sim \pm 15\%$. The retrieval error in a at the other wavelengths is likely to be about the same. The absorption (after removal of that of pure water) was found to vary exponentially with wavelength, i.e., $\propto \exp[-S\lambda]$, with $S = 0.011 \text{ nm}^{-1}$, suggesting significant absorption by detrital material. At the stations at which the detached coccoliths clearly dominate the scattering, Fig. 6 shows that the retrieved backscattering coefficients all have similar spectral shapes, i.e., maximum b_b in the blue decreasing toward the green, a minimum near 550–620 nm, and then increasing into the red. It clearly is *not* proportional to λ to some power (i.e., a “power law”) over the entire visible spectrum.

B. Retrieval of $a(443)$ and $b_b(443)$ from SeaWiFS Imagery

As mentioned earlier, SeaWiFS imagery is available on the same day for which the in-water data were obtained. We used a version of the spectral optimization algorithm (SOA) [27] modified for operation in Case 2 waters with high backscattering [28,29]. Proper operation of this algorithm requires site-specific bio-optical parameters; however, in the absence of such parameters for the area in question, we used the Case 1 water parameters used by Chomko *et al.* [27] but with the Case 2 high-backscattering modification. The SOA retrieves the concentration of

Chlorophyll a , the absorption coefficient of detrital material (dissolved and particulate) at 443 nm and the backscattering coefficient at 443 nm. From the retrieved Chlorophyll a , the absorption coefficient of phytoplankton is obtained. Thus, the absorption coefficient minus that of water at 443 nm, a_{pd} , and the backscattering coefficient of particles b_{bp} at 443 nm are obtained from the imagery. Table 1 compares these retrievals with the associated values obtained through the in-water radiance/irradiance data. The SeaWiFS retrieval at Station 4 is not included because the backscattering coefficient exceeded the upper limit allowed in the SOA code ($b_{bp} = 0.1 \text{ m}^{-1}$). When this happens, none of the other retrieved parameters are viable.

Comparison between the inverted- and the SeaWiFS-derived scattering and absorption properties at 443 nm suggest that both are dependable, and that the retrieved $b_{bp}(\lambda)$ is likely to be uncertain to less than the $\pm 25\%$ upper limit to the error suggested on the basis of the Chalk-Ex retrievals in Section 3.

C. Estimate of the Backscattering Cross Section of Detached Coccoliths at 500 nm

We wish to estimate the backscattering cross section of an individual detached coccolith. For a given backscattering coefficient b_b , this is given by $\sigma_b \equiv b_b/N_{\text{Coccolith}}$, where $N_{\text{Coccolith}}$ is the number concentration (number per unit volume) of detached coccoliths, provided in Table 2. As it is critical in understanding the accuracy of the resulting σ_b , we first discuss the uncertainties in $N_{\text{Coccolith}}$. As mentioned earlier, we use the flow cytometry (FC) measurements of fresh (unpreserved) samples rather than manual counting of samples preserved in buffered formalin because coccolithophore cells are observed to shed coccoliths when stored in this manner. Several experiments were carried out to estimate the uncertainty in $N_{\text{Coccolith}}$. First, two different flow cytometers were used to measure $N_{\text{Coccolith}}$ for the same samples fixed in buffered formalin. The two flow cytometers differed by $\sim 20\%$. This is a measure of the uncertainty in the flow cytometer methodology used in this paper. Second, the FC comparisons (made with the two flow cytometers) with manual microscopic counts (taken as the “gold standard”) of the same samples showed that the manual-count concentration was $\sim 1.38\times$ that determined by FC. Thus, the FC concentrations are about

Table 1. Comparison of the SeaWiFS Retrieved Backscattering and Absorption Parameters at 443 nm with those Derived from Inversion of the In-Water Radiance/Irradiance Data^a

Station	$a_{pd}(\text{m}^{-1})$ SeaWiFS	$a_{pd}(\text{m}^{-1})$ Inverted	$b_{bp}(\text{m}^{-1})$ SeaWiFS	$b_{bp}(\text{m}^{-1})$ Inverted	Chl $a(\text{mg}/\text{m}^3)$ SeaWiFS	Chl $a(\text{mg}/\text{m}^3)$ <i>In Situ</i>
1	0.207	0.148	0.0138	0.0139	2.003	1.375
2	0.189	0.160	0.0533	0.0548	2.051	1.972
3	0.325	0.339	0.0615	0.0726	4.238	3.340

^aThe “Inverted” values are from a depth of five meters. The SeaWiFS values are derived assuming the constituent concentrations are uniform.

Table 2. Coccolith Concentration ($N_{\text{Coc}} = N_{\text{Coccolith}}$ in ml^{-1}) and the Ratio of Coccolith to Coccospheres ($N_{\text{Coc}}/N_{\text{Cell}}, N_{\text{Cell}} = N_{\text{Coccosphere}}$) as a Function of Depth (z in m) for the Four Stations Examined

z	Station 1		Station 2		Station 3		Station 4	
	N_{Coc}	$N_{\text{Coc}}/N_{\text{Cell}}$	N_{Coc}	$N_{\text{Coc}}/N_{\text{Cell}}$	N_{Coc}	$N_{\text{Coc}}/N_{\text{Cell}}$	N_{Coc}	$N_{\text{Coc}}/N_{\text{Cell}}$
0					424,921	64	541,007	130
2	40,524	92	436,037	215				
5	42,138	52	258,898	110	309,152	67	459,848	129
10	57,990	128	306,134	139	494,196	206	434,959	149
15	16,371	46	244,986	125	378,991	235	92,060	50
20	19,243	45	214,669	113	384,170	158	104,427	70
25	32,263	75	244,864	183	269,391	236		

28% too low. Finally, comparison between the FC concentrations (with two flow cytometers) of fresh (unpreserved, live) samples and those preserved in buffered formalin showed that the preserved samples had approximately twice (1.94 \times) the number of detached coccoliths. Summarizing, these experiments suggest that (1) the inherent error in our FC methodology is $\sim 20\%$, (2) our FC measurements yield concentrations that should be multiplied by 1.38 to provide those that would be measured by microscopic counting of fresh samples, and (3) coccolithophores in samples that are stored in formalin for later counting lose coccoliths, so the resulting coccolith concentrations are too high by approximately a factor of two. Thus, in determining σ_b , we take the FC-measured concentrations and multiply them by 1.38 to get $N_{\text{Coccolith}}$, the result that would be obtained for manual microscopic counting of fresh samples. We estimate the uncertainty in $N_{\text{Coccolith}}$ to be $\pm 20\%$, and combined with an uncertainty of $\pm 25\%$ in b_b (but likely significantly less), the uncertainty in the final σ_b will be $\sim \pm 32\%$.

Figure 7 shows σ_b as a function of $N_{\text{Coccolith}}$. Note, in this figure $b_b(500)$ is actually pooled data consisting of $b_b(490)$ and $b_b(510)$. In preparing this graph, data from all stations and all depths at which retrievals were actually obtained at 490 and 510 nm are

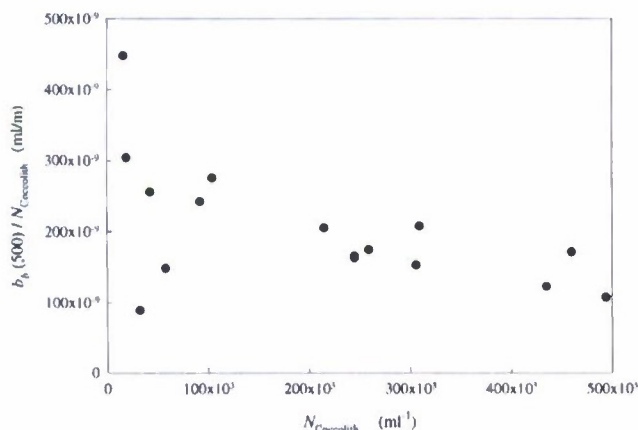


Fig. 7. Backscattering at 500 nm divided by the detached coccolith concentration as a function of the detached coccolith concentration as measured by flow cytometry. This is an estimate of σ_b . Note, $1 \text{ ml/m} = 10^6 \mu\text{m}^2/\text{coccolith}$, so $100 \times 10^{-9} \text{ ml/m} = 0.100 \mu\text{m}^2/\text{coccolith}$.

included. Since detached coccoliths are not the only constituent of the water—there are also coccolithophore cells, other phytoplankton (e.g., possibly the dinoflagellate, *G. mikimotoi*), as well as detrital particles—such a determination will only yield an upper limit to the average σ_b , as it is implicitly assumed that *all* of the backscattering is due to detached coccoliths. As the coccolith concentrations increase, detached coccoliths increasingly dominate seawater backscattering, thus the estimate of $\sigma_b(500)$ becomes better as $N_{\text{Coccolith}}$ becomes larger. This is clearly seen in the figure as the general trend is a decreasing $\sigma_b(500)$ as $N_{\text{Coccolith}}$ increases.

We can try to compensate for other particles in the water by using Station 1 (originally thought to be outside the bloom) to estimate the background backscatter by other particles. Thus, in Fig. 8 we have plotted $[b_b(500) - b_b(500, \text{Station 1})] / [N_{\text{Coccolith}} - N_{\text{Coccolith}}(\text{Station 1})]$ as a function of $N_{\text{Coccolith}} - N_{\text{Coccolith}}(\text{Station 1})$. Averaging the three data points with $N_{\text{Coccolith}} - N_{\text{Coccolith}}(\text{Station 1}) > 350,000$ per ml, we estimate the *upper limit* to $\sigma_b(500)$ is approximately $0.123 \mu\text{m}^2/\text{coccolith}$. We stress that this is the upper limit, because there is still a component of the scattering due to intact coccolithophore cells (and possibly other particles) that

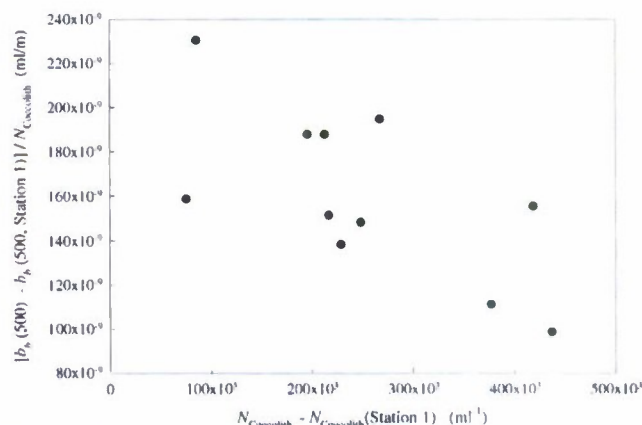


Fig. 8. Backscattering at 500 nm (minus that at Station 1) divided by the detached coccolith concentration (minus that at Station 1) as a function of the detached coccolith concentration (minus that at Station 1) as measured by flow cytometry. This is an estimate of σ_b . Note, $1 \text{ ml/m} = 10^6 \mu\text{m}^2/\text{coccolith}$, so $100 \times 10^{-9} \text{ ml/m} = 0.100 \mu\text{m}^2/\text{coccolith}$.

may not be removed by subtracting the background. Combining the $\pm 20\%$ error in FC counting and the $\pm 25\%$ error in $b_b(500)$, we estimate that the maximum error in $\sigma_b(500)$ to be $\sim \pm 32\%$, but because the uncertainty estimate for b_b is likely too large, the uncertainty in σ_b is likely smaller.

This backscattering cross-section estimate is similar to those determined by other investigators on natural samples or on laboratory cultures: $0.1 \mu\text{m}^2/\text{coccolith}$ by Balch *et al.* [30]; $0.135 \mu\text{m}^2/\text{coccolith}$ by Balch *et al.* [31]; and $0.13\text{--}0.16 \mu\text{m}^2/\text{coccolith}$ by Voss *et al.* [32]. The ultimate goal of the modeling in this paper is to be able to reproduce both the spectral shape of σ_b and its absolute magnitude at 500 nm.

5. Physical Model for a Detached Coccolith

The physical model we used for a detached coccolith is a modified “fishing reel” model from Gordon and Du [12]. In this model, the coccolith is modeled as two parallel disks (the proximal and distal shields) joined by a hollow cylinder. The modifications were based on the computations presented by Gordon [33,34].

First, noting that the distal shield or disk (further from the cell interior) has a periodic fine structure resembling the “spokes” of a wheel, Gordon [33] investigated the influence on backscattering of such a periodic disklike structure. It was found for disks with refractive index similar to calcite, that if the scale of the periodicity (arc length of the space between the spokes at the rim of the wheel) is greater than one-quarter of a wavelength of the light (in the medium), the backscattering is significantly enhanced. The distal shield of *E. huxleyi* coccoliths have a periodicity such that the quarter-wave limit could be exceeded in the blue to blue-green region of the spectrum, which could enhance the backscattering.

Second, noting that the distal shield of *E. huxleyi* coccoliths is not precisely periodic, Gordon [34] examined the influence of aperiodic effects on disklike structures and found that, in the range of aperiodicity displayed by the individual coccoliths, the backscattering did not differ significantly from that of their perfectly periodic counterparts.

Third, taking into consideration the possible effects of periodicities on backscattering, the distal shield is modeled as a periodic pinwheel structure [33] with alternating occupied and unoccupied sectors. The relative refractive index of the distal shield is taken to be 1.20.

Fourth, the proximal shield also has a quasi-periodic structure of thin radial slits; however, these have a width much less than a quarter of a wavelength. Gordon [33] showed that such a periodic structure scatters like a solid disk, albeit with an effective (reduced) refractive index. Thus, in our model coccolith, the proximal shield is modeled as a solid disk with a refractive index of 1.19.

As in Gordon and Du [12] the two disklike structures are joined by a hollow cylinder. The resulting

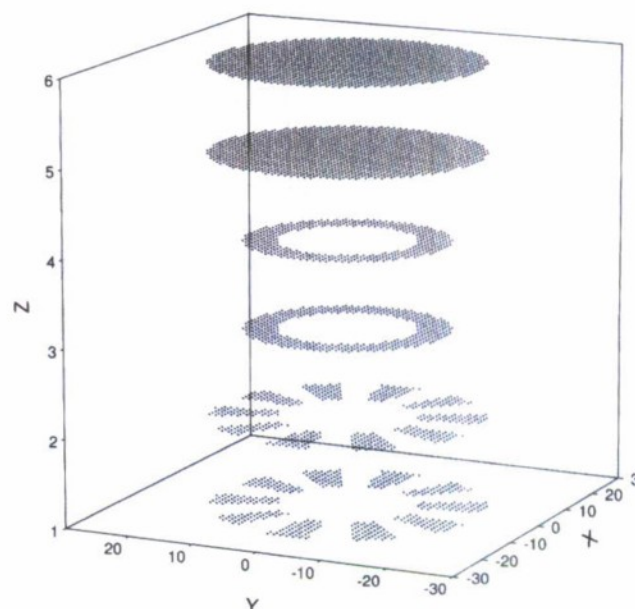


Fig. 9. Schematic of the model of the position of the individual dipoles comprising the body of a detached coccolith. The top two disks are the proximal shield. They have a diameter of $3.5 \mu\text{m}$. The thickness of this disk ranges from 0.04 to $0.06 \mu\text{m}$. The two central “washer-shaped” disks represent the cylinder joining the proximal and distal shields. This cylinder has an inner diameter of $1.38 \mu\text{m}$ and an outer diameter of $1.58 \mu\text{m}$. The “pinwheel” at the bottom represents the distal shield, and is shown here with 10 “vanes.” In the actual coccolith model, the distal shield has 40 “vanes.” The separation between the distal and proximal shields is 0.30 to $0.35 \mu\text{m}$. In the figure, the bottom four objects have a refractive index of 1.20, while the top two objects have an index of 1.19. The maximum number of layers (6 are shown here) of dipoles in the actual coccolith model is up to 24, corresponding to a layer spacing of $\sim 0.02 \mu\text{m}$.

structure is similar to the schematic in Fig. 9. The individual points in Fig. 9 represent the positions of the individual dipoles in the DDA. The two disklike objects have diameters (D) of $3.5 \mu\text{m}$. This size was chosen based on the mean diameters of *E. huxleyi* coccoliths given by Young and Ziveri [35]. The thickness (t) of the individual disks ranges from 0.04 to $0.06 \mu\text{m}$, as estimated from scanning electron microscope (SEM) images of individual coccoliths (but unfortunately not from the bloom under consideration here). The cylinder joining the shields has an inner diameter of $1.38 \mu\text{m}$ and an outer diameter of $1.58 \mu\text{m}$. The “pinwheel” at the bottom represents the distal shield, and is shown with 10 “vanes.” In the actual coccolith model, the distal shield has 40 “vanes.” The separation (“gap” or t_{gap}) between the distal and proximal shields is 0.30 to $0.35 \mu\text{m}$ (also estimated from SEM images). The volume of the individual coccoliths ranges from $0.69 \mu\text{m}^3$ (for a gap of $0.30 \mu\text{m}$ and a shield thickness of $0.04 \mu\text{m}$) to $0.98 \mu\text{m}^3$ (for a gap of $0.35 \mu\text{m}$ and a shield thickness of $0.06 \mu\text{m}$). These compare favorably with an estimate of $0.9 \mu\text{m}^3$ for “normally calcified” coccoliths provided by Young and Ziveri [35].

Finally, a valid criticism of this model is that the gross morphology is that of a disk while the shields

are actually sections of spheres, i.e., they fit nicely to form the spherical coccolithophore (the “coccosphere”). However, Gordon [33] showed that a section of a sphere backscatters in a manner that is nearly identical to the tangent disk of the same diameter. Thus, we assume the curvature of the disks is unimportant in the present model.

It is well known that single crystals of calcite are birefringent. Likewise, coccoliths are uniaxial birefringent structures with the “C axis” (the optical axis) radial from the center of the coccolith [36]. We know of no highly-accurate light-scattering computer code that is presently capable of handling such birefringence. However, using the Rayleigh–Gans approximation to light scattering, Gordon [37] assessed the influence of birefringence on light scattering by disk-like structures with a radial optical axis and concluded that the error in backscattering introduced by ignoring birefringence was of the order of 10% or less. Since the Rayleigh–Gans approximation has been shown to be a reasonable approximation to scattering by disklike particles in the coccolith size range, we conclude that ignoring birefringence will lead to backscattering errors of the order of 10% or less.

6. Scattering and Backscattering of the Model Coccoliths

Computations of the light-scattering properties of the model coccoliths were carried out using the discrete-dipole approximation (DDA) [11,38] DDSCAT Version 6.1. DDSCAT code was run on an 80-

processor cluster using the built-in message passing interface (MPI) features. As the scattering from a structure as complex as that shown in Fig. 9 is strongly dependent on orientation, proper orientation averaging is critical to deriving orientationally-averaged optical properties. The number of orientations that must be averaged to obtain the IOPs for randomly oriented particles is dependent on the IOP in question. The total scattering cross section requires the least number and the back scattering cross section calculation requires a higher number of orientations. Based on extensive testing, for σ and σ_b we averaged over approximately 80,000 orientations, which, considering the symmetry of the particle (with 40 vanes, rotation about the cylinder axis by 9° returns the particle a position equivalent to its original position), would correspond to 3,200,000 orientations for a particle with no symmetry.

Figure 10 provides the orientationally averaged spectral backscattering for the model coccolith. It is separated into panels with each panel representing a given shield thickness, and one panel providing the mean of the nine model coccoliths (the “model mean”). The points joined with dashed lines on the panel with the model-mean backscattering cross section correspond to the measured spectra normalized to $0.085 \mu\text{m}^2$ at 510 nm to approximately match the model mean at 500 nm of $0.092 \mu\text{m}^2$. Note that the computed σ_b spectra for all of the model coccoliths have essentially the same shape—a decreasing backscattering from 500 to 600 nm followed by a nearly constant backscattering in the near infrared. Only

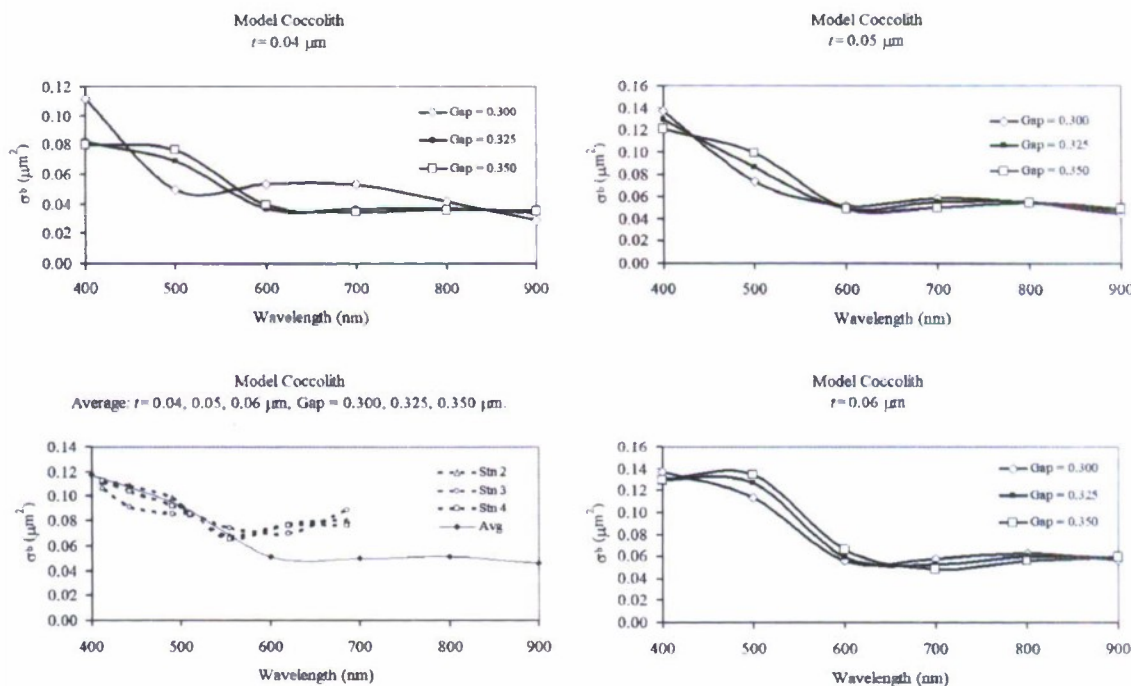


Fig. 10. Backscattering cross section σ_b of the model coccoliths. The panels clockwise starting from the upper left are for shield diameters $D = 3.5 \mu\text{m}$ and thicknesses $t = 0.04, 0.05$, and $0.06 \mu\text{m}$, with each panel containing three different separations between the proximal and distal shields in μm (“Gap”). The fourth panel is the σ_b averaged over the other three. The dashed lines in the fourth panel correspond to the measured spectra normalized to $0.085 \mu\text{m}^2/\text{coccolith}$ at 510 nm. To get σ_b specific to a mole of calcite (in units m^2/mole of calcite) multiply the ordinate scale on the lower right panel by $44.2 \text{ m}^2/\text{mole}$, i.e., at 600 nm $\sigma_b = 2.26 \text{ m}^2/\text{mole}$.

the spectrum for the smallest $t(0.04\ \mu\text{m})$ coupled with the smallest gap ($0.30\ \mu\text{m}$) shows the opposite trend in the visible. Interestingly, as one might expect, the averaged spectrum is close to that of the “average” model coccolith: $t = 0.05\ \mu\text{m}$ and gap = $0.325\ \mu\text{m}$. The σ_b spectra for the model-mean coccolith agrees well with the retrieved spectra over the range 400 nm to about 550 nm; however, in the red and infrared the model backscattering is too low. It should be noted that when normalized to the calcite concentration, rather than the coccolith concentration, the average σ_b at 600 nm ($2.26\ \text{m}^2/\text{mole}$) agrees well with the Balch *et al.* [39] measurements of the acid-labile backscattering at 632 nm averaged over several species of cultured calcifying algae ($2.77\ \text{m}^2/\text{mole}$). For completeness, Fig. 11 provides

the associated backscattering probability, $\sigma_b = \sigma_b/\sigma$, for each of the model coccoliths and the average σ_b ÷ the average σ .

For a measure of the influence of the diameter of the shields on the scattering properties, we computed the optical properties for the “average” model coccolith ($t = 0.05\ \mu\text{m}$ and gap = $0.325\ \mu\text{m}$) with the diameter varied from 2.5 to $4.0\ \mu\text{m}$. The resulting spectra for σ , σ_b , $\tilde{\sigma}_b$, and σ_b/D^2 are presented in Fig. 12. The $\tilde{\sigma}_b$ spectra show that the increase in backscattering with diameter over the range 600 to 900 nm can be completely explained by the increase in total scattering σ with diameter, while in the range 400–600 nm the backscattering increases faster with diameter than the total scattering. Also,

one might expect scattering properties to be proportional to D^2 (i.e., approximately the cross sectional area of the particle) as D becomes large or λ becomes small. The σ_b/D^2 spectra (Fig. 12, lower-right panel) confirm this for $D \geq 3\ \mu\text{m}$ and $\lambda \leq 900\ \text{nm}$. Thus, in this regime $\sigma_b \propto D^2$ and Fig. 10 can then be used to estimate σ_b for any $D \geq 3\ \mu\text{m}$.

Finally, it is interesting to note that the spectra in the upper-left panel of Fig. 12 can be fit well to the formula $\sigma = k\lambda^{-n}$ with $n = 2$ and k a constant. This is generally the case for disklike objects as was found by Gordon and Du [12].

7. Influence of Intact Cells on the Estimated σ_b for Coccoliths

The estimates of σ_b for coccoliths in Subsection 4.C were obviously influenced by the backscattering from intact coccolithophore cells. Although the detached coccoliths outnumber the intact cells by factors of 45 to 235 (Table 2) in the flow cytometer measurements, the intact cells (from which coccoliths have yet to detach, henceforth referred to as “coccospheres”) can make a contribution by virtue of the fact that they backscatter much more strongly than coccoliths, i.e., by a factor of the order of 40 [32]. In this Section we attempt to estimate the effect of coccospheres on the retrieved σ_b . This is accomplished by (1) estimating the backscattering by coccospheres, and (2) assessing the influence of their presence on the apparent value of $\sigma_b(500)$ for detached coccoliths.

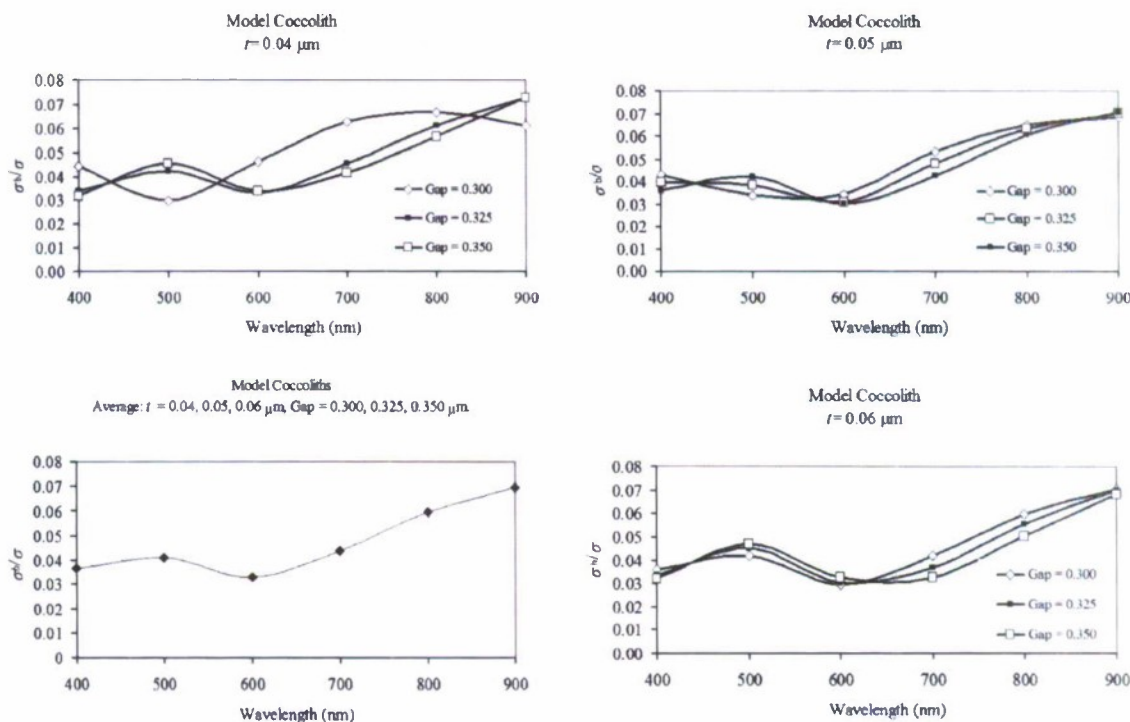


Fig. 11. Backscattering probability of the model coccoliths. The panels clockwise starting from the upper left are for shield diameters $D = 3.5\ \mu\text{m}$ and $t = 0.04, 0.05$, and $0.06\ \mu\text{m}$, with each panel containing three different separations between the proximal and distal shields in μm (“Gap”). The fourth panel is the backscattering probability averaged over the other three, i.e., the average of σ_b divided by the average of σ .

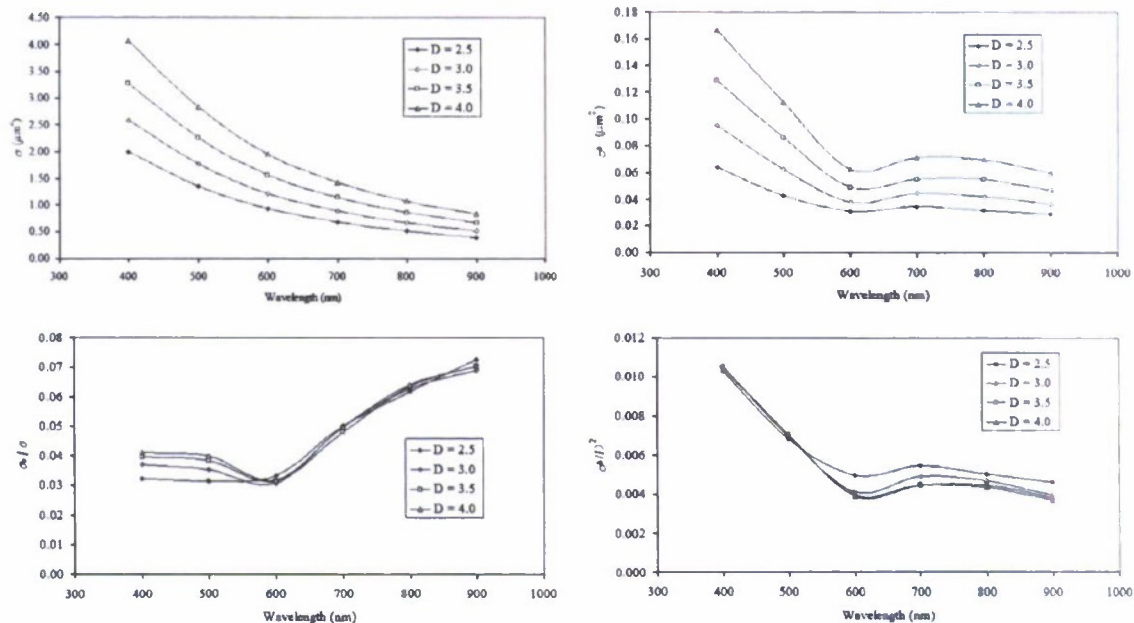


Fig. 12. Spectral scattering properties of the “average” model coccolith ($t = 0.05 \mu\text{m}$ and gap $= 0.325 \mu\text{m}$) as a function of the diameter (D) of the shields, as the diameter is varied from varied from 2.5 to 4.0 μm . Clockwise from the lower left, the spectra are for σ_b/σ , σ , σ_b , and σ_b/D^2 , respectively. (D is in μm .)

A. Light-Scattering Model of a Coccosphere

There is no feasible method available today of modeling a coccolithophore cell with any precision. However, we believe that it is reasonable to expect that coccoliths on the surface of coccolithophore cells backscatter in a manner similar to free detached coccoliths in random orientation. We arrive at this expectation through the following reasoning.

A single layer of coccoliths (each resembling two parallel disks of thickness t separated by a gap of thickness t_{gap}) packed around a spherical core approaches a spherical structure consisting of an outer spherical shell of thickness t , a gap of thickness t_{gap} , and a concentric inner shell of thickness t . Although there are no freely available computer codes for dealing with multishell objects with spherical symmetry, there are approximations with which one can compute their backscattering to within a few tens of percent. Gordon [37] has shown that computations of the backscattering of thin disklike structures in random orientation using the Rayleigh–Gans approximation (RGA) compare favorably with those computed using the DDA, as long as the thickness of the disk divided by the wavelength of the light (in water) was less than 0.2. Further, it was shown that if two such disks meeting this criterion are arranged in a parallel structure (similar to a coccolith) the RGA provides an excellent approximation to the DDA backscattering. This suggests that the backscattering by a single spherical shell may also be reasonably well computed using the RGA. To test this hypothesis we compared the exact backscattering by a spherical shell (computed using the code supplied in Bohren and Huffman [40]) with that computed using the RGA. Over the visible spectrum, for a spherical shell of

radius 4 μm , thickness 0.05 μm , and refractive index 1.20, the ratio (exact- σ_b) \div (RGA- σ_b) varied between 1.3 and 1.4 with an average of 1.36, suggesting that the RGA underestimates the backscattering by $\sim 35\%$ in this case. The fact that the RGA also works well for parallel disks in random orientation [37] suggests that it should also work well for concentric spherical shells. We computed the backscattering cross section of concentric spherical shells, each of thickness $t = 0.05 \mu\text{m}$, separated by a gap $t_{\text{gap}} = 0.325 \mu\text{m}$ (similar to the “average” coccolith model’s shield thickness and gap thickness), for overall outer radii of 1.5 to 5.0 μm using the RGA. The results are provided in Fig. 13. We note that these spectra have a

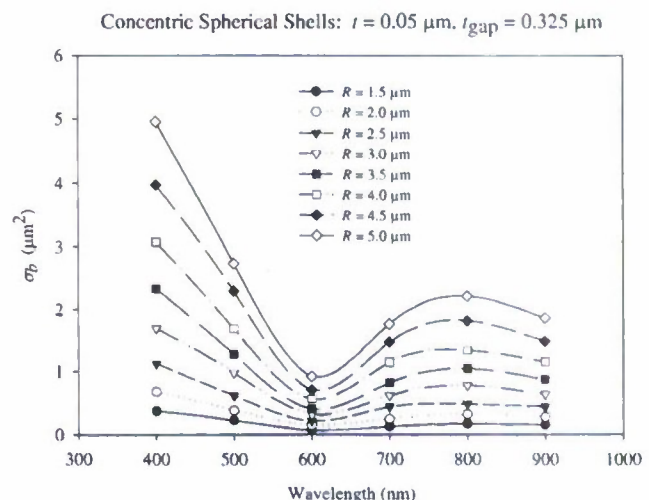


Fig. 13. Backscattering cross section of a particle consisting of two concentric spherical shells as a function of the overall particle radius (R).

shape similar to the spectra of our model coccoliths, i.e., they display a minimum backscattering near 600 nm. When the spectra are normalized at 600 nm (Fig. 14) they are all similar, which suggests that the shell thickness and the gap between the shells, and not the overall size, determines the spectral shape. In addition, we computed the spectral backscattering in the RGA by two parallel disks (disk diameter of $3.50\text{ }\mu\text{m}$, disk thickness of $0.05\text{ }\mu\text{m}$, and disk separation of $0.325\text{ }\mu\text{m}$) in random orientation. This spectrum (normalized at 600 nm) is also plotted in Fig. 14. Note the similarity of the spectral variation of backscattering between the disk and the sphere, suggesting that the backscattering of concentric spherical shells can be modeled as a collection of some number of independent parallel disks with the same thickness and separation, in random orientation.

Examination of SEM images of *E. huxleyi* coccospheres suggests that their diameter is approximately twice the diameter of the distal shield of the coccolith (see images in [33]). Since most of our computations were for coccoliths with $3.5\text{ }\mu\text{m}$ shields, we took the overall diameter of the coccosphere to be $7.0\text{ }\mu\text{m}$. If we imagine the two concentric shells to be a layer of coccoliths, then when the outer radius of the outer shell is $3.5\text{ }\mu\text{m}$ and the diameter of the individual coccoliths is also $3.5\text{ }\mu\text{m}$, the area of approximately 12 coccoliths equals the area of the sphere on which they reside (radius $3.075\text{ }\mu\text{m}$ for the "average" coccolith model). In reality it would require more than 12 coccoliths because they would have to overlap to cover the entire sphere. If we assume maximum overlap, i.e., the coccolith shields are packed in contact with the central core structure, then it would take ~ 20 coccoliths to cover the sphere. At 500 nm, σ_b computed for the "average" model coccolith in random orientation is $0.086\text{ }\mu\text{m}^2$, while Fig. 13 provides $1.28\text{ }\mu\text{m}^2$ for the concentric shells. The ratio

(concentric shells- σ_b) \div (coccolith- σ_b) is ~ 14 , in reasonable agreement with the two estimates of the number of coccoliths required for coverage. (Actually, the Fig. 13 estimate of σ_b is likely to be low by 30–40%, so the estimated number is likely to be higher than 14 by 30–40%). Thus, we henceforth assume that the coccoliths on a coccosphere scatter *independently* and in the same manner as detached coccoliths in random orientation.

SEM imagery also suggests that the coccosphere consists of at most three layers, but more typically one or two layers of coccoliths. Using our average coccolith model (disk diameter of $3.50\text{ }\mu\text{m}$, disk thickness of $0.05\text{ }\mu\text{m}$, and disk separation of $0.325\text{ }\mu\text{m}$), the first layer would be covering a sphere of radius $3.075\text{ }\mu\text{m}$, the second a sphere of radius $2.65\text{ }\mu\text{m}$, and the third a radius of $2.225\text{ }\mu\text{m}$, having areas of approximately 119, 88, and $62\text{ }\mu\text{m}^2$, respectively. These are in the ratio 1.00:0.74:0.52, so the number of coccoliths required per coccosphere would be 12–20 (for 1 layer), 21–35 (for 2 layers), and 27–45 (for 3 layers) depending on packing. The average between the smallest (12) and the largest (45) is 29 coccoliths per coccosphere. For 29 coccoliths per coccosphere, $\sigma_b(\text{coccosphere}) = 29 \text{ coccoliths/coccosphere} \times 0.086\text{ }\mu\text{m}^2$ or $\sim 2.5\text{ }\mu\text{m}^2/\text{coccosphere}$ with an overall range of ~ 1 to $4\text{ }\mu\text{m}^2/\text{coccosphere}$ at 500 nm, depending on packing and the number of layers.

B. Apparent σ_b for Coccoliths when Coccosphere Backscattering is Included

We now compute the apparent σ_b at 500 nm in a mixture of coccoliths and coccospheres. If $N_{\text{Coccolith}}$ and $N_{\text{Coccosphere}}$ are the number concentration of coccoliths and coccospheres, respectively, then when coccospheres contribute to the backscattering the apparent coccolith backscattering is given by

$$\sigma_b(\text{apparent}) = \sigma_b(\text{coccolith}) + \frac{N_{\text{Coccosphere}}}{N_{\text{Coccolith}}} \sigma_b(\text{coccosphere}). \quad (5)$$

Using $\sigma_b(\text{coccolith}) = 0.092\text{ }\mu\text{m}^2/\text{coccolith}$ (the model-mean) and $\sigma_b(\text{coccosphere}) = 2.5\text{ }\mu\text{m}^2/\text{coccosphere}$ at 500 nm, we find an average $\sigma_b(\text{apparent}) = 0.114 \pm 0.013\text{ }\mu\text{m}^2/\text{coccolith}$ at 500 nm for Stations 2–4 (high coccolith concentrations). Comparison of $\sigma_b(\text{apparent})$ and the retrieved upper limit for $\sigma_b(500)$ from Section 4 of $0.123\text{ }\mu\text{m}^2/\text{coccolith}$ with an estimated error of $\pm 32\%$ (but likely less) reveals excellent agreement between the two, with coccospheres contributing about 20% of the observed backscattering.

8. Discussion

The modeling discussed above has the virtue that it reproduces reasonably well the spectral variation of backscattering of particles in the Plymouth coccolithophore bloom. In addition, the apparent backscattering cross section at 500 nm of coccoliths

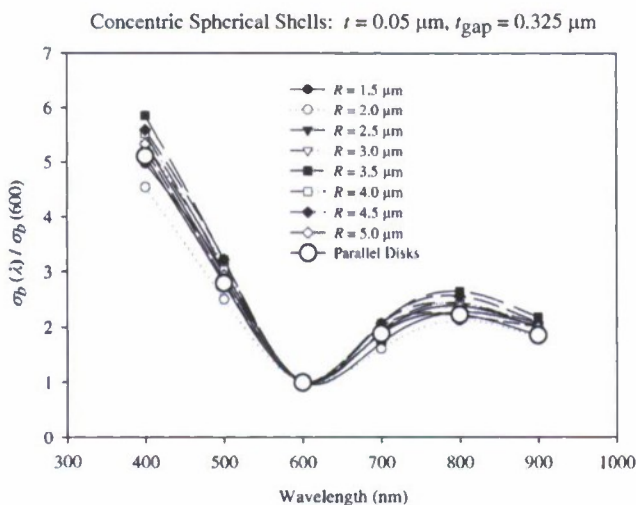


Fig. 14. Same as Fig. 13, except the results are normalized at 600 nm, and the backscattering of two parallel disks (disk diameter of $3.50\text{ }\mu\text{m}$, disk thickness of $0.05\text{ }\mu\text{m}$, and disk separation of $0.325\text{ }\mu\text{m}$) in random orientation has been included as well.

when coccospheres are included ($0.114 \pm 0.013 \mu\text{m}^2/\text{coccolith}$) compares favorably with the measured value ($0.123 \pm 0.039 \mu\text{m}^2/\text{coccolith}$). One goal of the present work is to ascertain the complexity of the model required to understand the backscattering of detached coccoliths. To that end, we simplified the model by replacing the pinwheel used for the distal shield (Fig. 9) by a solid disk and by using a refractive index of 1.20 for the entire model structure. These changes increased $\sigma_b(\text{coccolith})$ at 500 nm from 0.092 to $0.114 \mu\text{m}^2/\text{coccolith}$, and $\sigma_b(\text{apparent})$ to $0.143 \pm 0.016 \mu\text{m}^2/\text{coccolith}$, and although the agreement with $\sigma_b(\text{apparent})$ is poorer, it is still within the uncertainty estimates. Thus, to better constrain the modeling, backscattering data with less uncertainty are needed.

One way to obtain such data is through experimentation with laboratory cultures. However, coccolithophores have been grown before in batch culture and coccoliths harvested using flow cytometry for bulk scattering measurements. The $\sigma_b(632)$ within multiple clones of a single species, *E. huxleyi*, was shown to have a coefficient of variation of $\pm 30\%$ ([39], see their Table 4). Presumably, this variability was from changes in the morphology of the coccoliths as growth rates changed within the batch cultures. A much more laborious, but precise, way to control growth and calcification would be to grow them using nutrient-limited chemostats. The optical scattering of coccoliths has not been examined in steady-state growth to our knowledge, but also might show significant variability as a function of growth rate. This is because the ratio of calcification to photosynthesis increases as growth rate increases [41]. That is, coccolithophore cells could either increase their calcification rate by producing more coccoliths (which presumably would not change the coccolith scattering cross section), or increase coccolith diameter or thickness (which would change their particle-specific scattering cross section). This will have to await more experimentation.

It remains to consider the possible contamination from other phytoplankton (*G. mikimotoi*), i.e., can *G. mikimotoi* backscatter enough to make a significant contribution to $\sigma_b(\text{apparent})$ at 500 nm? To try to get an estimate of the possible contribution of *G. mikimotoi*, we considered backscattering by a sphere of 20 μm diameter (Nakamura *et al.* [42] give the "equivalent spherical diameter" of *G. mikimotoi* to be $\sim 19 \mu\text{m}$). Using Mie theory [43], computation of $\sigma_b(500)$ yielded 0.28, 0.98, 3.7, and $6.0 \mu\text{m}^2/\text{cell}$, for assumed refractive indices of 1.03, 1.04, 1.05, and 1.06, respectively. Noting that nonspherical particles can backscatter significantly more than equal-volume spheres [8], we assume $\sigma_b(500) \approx 10 \mu\text{m}^2/\text{cell}$, i.e., almost double the largest Mie estimate of $\sigma_b(500)$, as an order-of-magnitude estimate for *G. mikimotoi*. Then, in order for these cells to contribute $0.01 \mu\text{m}^2/\text{coccolith}$ to $\sigma_b(\text{apparent})$ for coccoliths, $N_{G.\text{mikimotoi}}/N_{\text{Coccolith}}$ would be required to be of the order of $\sim 10^{-3}$, so the *G. mikimotoi* concentration

would have to be about 1/20 to 1/4 of the coccosphere concentration. It is hard to imagine that cells at this concentration would not be detected. The coarseness of this computation notwithstanding, it seems unlikely that inclusion of *G. mikimotoi* cells in the mix of particles could make a significant contribution to the backscattering, as the required concentration would be quite detectable but their presence was not apparent at the stations used in this study.

Finally, we have assumed throughout that the detached coccolith particles are in random orientation. If the particles have a preferred orientation the influence on backscattering as measured in the inversions could be large because of the way that $\sigma_b(\text{apparent})$ was obtained. If the particles have even a slight tendency to align with coccolith plates oriented predominantly horizontally, the measured backscattering would be significantly greater because the upwelling light in the water would be preferentially backscattered from the flat shields. However, if the particles are embedded in a turbulent flow, in which the turbulence is isotropic, one would expect they would have random orientation. In addition, if they were initially aligned by some manner, Brownian motion would randomize the alignment with a relaxation time of ~ 1 s. The only sources of alignment that we can envisage would be a shear flow [44] or non-isotropic turbulence. As far as we know, there are no data concerning particle orientation in the surface waters of the ocean, so we have no basis on which to assume any orientation other than random.

9. Summary and Concluding Remarks

We used *in situ* radiance/irradiance profiles to estimate profiles of the sum of the spectral backscattering coefficient for all particles in an *E. huxleyi* coccolithophore bloom off the coast of Plymouth, UK. The inversion algorithm for retrieval of b_b was validated through comparison with direct measurements in the Chalk-Ex experiment. The validation exercise suggested the error in the retrieved b_b should be less than 25%. The retrieved spectra of backscattering all showed a minimum near ~ 550 to 600 nm. Given flow cytometry estimates of the detached coccolith concentration, and assuming all of the backscattering (over and above the backscattering of the water itself) was due to detached coccoliths, we determined the backscattering cross section (σ_b) of a coccolith to be $0.123 \pm 0.039 \mu\text{m}^2/\text{coccolith}$ at 500 nm. We then developed a physical model of a coccolith and computed its backscattering cross section (in random orientation) to be $0.092 \mu\text{m}^2/\text{coccolith}$ at 500 nm. The computed σ_b also displayed a spectral shape similar to the measurements, but with less apparent increase in the red. However, on a "per mole of CaCO_3 " rather than "per coccolith" basis, $\sigma_b(600)$ agreed reasonably well with that determined by Balch *et al.* [39] for the acid-labile backscattering at 632 nm averaged over several species of cultured calcifying algae (Fig. 10).

Knowing that there were also intact coccolithophore cells that have a much larger backscattering cross section than free coccoliths, and given their concentrations, we tried to account for their effect on the derived coccolith cross section. Arguing that coccoliths attached to coccospheres backscatter in a manner similar to free coccoliths, estimating the number of coccoliths per coccosphere, and using the observed number of coccospheres, we found σ_b (apparent) to be $0.114 \pm 0.013 \mu\text{m}^2/\text{coccolith}$ at 500 nm in good agreement with the measured $0.123 \pm 0.039 \mu\text{m}^2/\text{coccolith}$.

Although the inversion method yielded rather large uncertainty on the backscattering coefficient as validated in the Chalk-Ex experiment, we believe that the uncertainty is significantly smaller than 25% [24], and the major source of error may be estimating the coccolith concentrations. The major weakness of this study is the fact that neither the precise nature (size) of the detached coccoliths nor the coccospheres were determined through SEM measurements. Thus, we had to assume the dimensions of an average coccolith as provided by Young and Ziveri [35]. A second weakness is our inability to precisely model the backscattering by coccospheres.

This research was supported by grant N00014-07-1-0226 from the Office of Naval Research/Environmental Optics Program (HRG). T. Smyth and G. Tarran are supported under the NERC Oceans 2025 program. The Chalk-Ex work was supported by grants from the Office of Naval Research/Environmental Optics Program (awards N000140110042 and N00014-05-1-0111) and NASA/Ocean Biology and Biogeochemistry (NNG04G111G, NNX08AC27G, NNG04HZ25C). Bruce Bowler (Bigelow Laboratory) helped in processing the Chalk-ex OCP data. The backscattering inversion algorithm was developed under ONR grant numbers N00014-97-1-0069 and N00014-99-1-0007 (HRG). We are grateful to B. Draine and P. Flatau for making DDSCAT 7.1 available to the community, and to two anonymous reviewers, whose comments considerably improved this work.

References

1. S. G. Ackleson, "Optical determinations of suspended sediment dynamics in western Long Island Sound and the Connecticut River plume," *J. Geophys. Res.* **111**, C07009 (2006).
2. A. Morel, "Optical modeling of the upper ocean in relation to its biogenous matter content (Case I waters)," *J. Geophys. Res.* **93C**, 10,749–10,768 (1988).
3. A. Bricaud, A. Morel, and L. Prieur, "Optical efficiency factors of some phytoplankters," *Limnol. Oceanogr.* **28**, 816–832 (1983).
4. H. R. Gordon and A. Y. Morel, *Remote Assessment of Ocean Color for Interpretation of Satellite Visible Imagery: A Review* (Springer-Verlag, 1983).
5. D. Stramski and D. A. Kiefer, "Light scattering by microorganisms in the open ocean," *Prog. Oceanogr.* **28**, 343–383 (1991).
6. N. Hoepffner and S. Sathyendranath, "Determination of major groups of phytoplankton pigments from absorption spectra of total particulate matter," *J. Geophys. Res.* **98**, 22789–22803 (1993).
7. D. Stramski, E. Boss, D. Bogucki, and K. J. Voss, "The role of seawater constituents in light backscattering in the ocean," *Prog. Oceanogr.* **61**, 27–56 (2004).
8. W. R. Clavano, E. Boss, and L. Karp-Boss, "Inherent optical properties of non-spherical marine-like particles—from theory to observations," in *Oceanography and Marine Biology: An Annual Review*, R. N. Gibson, R. J. M. Atkinson, and J. D. M. Gordon, eds. (CRC, 2007), Vol. 45, pp. 1–38.
9. W. M. Balch, H. R. Gordon, B. C. Bowler, D. T. Drapeau, and E. S. Booth, "Calcium carbonate measurements in the surface global ocean based on moderate-resolution imaging spectroradiometer data," *J. Geophys. Res.* **110**, C07001 (2005).
10. *Light Scattering by Nonspherical Particles*, M. I. Mishchenko, J. W. Hovenier, and L. D. Travis, eds. (Academic, 2000).
11. B. T. Draine, "The discrete-dipole approximation and its application to interstellar graphite grains," *Astrophys. J.* **333**, 848–872 (1988).
12. H. R. Gordon and T. Du, "Light scattering by nonspherical particles: application to coccoliths detached from *Emiliania huxleyi*," *Limnol. Oceanogr.* **46**, 1438–1454 (2001).
13. T. J. Smyth, G. F. Moore, S. B. Groom, P. E. Land, and T. Tyrrell, "Optical modeling and measurements of a coccolithophore bloom," *Appl. Opt.* **41**, 7679–7688 (2002).
14. S. B. Hooker, W. E. Esaias, G. C. Feldman, W. W. Gregg, and C. R. McClain, "An overview of SeaWiFS and ocean color," of SeaWiFS Tech. Rep. Series, Tech. Memo. 104566, Vol. 1, S. B. Hooker and E. R. Firestone, eds., NASA, Greenbelt, MD, 1992.
15. H. R. Gordon, G. C. Boynton, W. M. Balch, S. B. Groom, D. S. Harbour, and T. J. Smyth, "Retrieval of coccolithophore calcite concentration from SeaWiFS imagery," *Geophys. Res. Lett.* **28**, 1587–1590 (2001).
16. J. L. Mueller and R. W. Austin, "Ocean optics protocols for SeaWiFS validation, rev. 1," of SeaWiFS Tech. Rep. Series, Tech. Memo. 104566, Vol. 25, S. B. Hooker and E. Firestone, eds., Nasa, Greenbelt, MD, 1995.
17. H. R. Gordon, and G. C. Boynton, "A radiance—irradiance inversion algorithm for estimating the absorption and backscattering coefficients of natural waters: stratified water bodies," *Appl. Opt.* **37**, 3886–3896 (1998).
18. H. R. Gordon, "The sensitivity of radiative transfer to small-angle scattering in the ocean: a quantitative assessment," *Appl. Opt.* **32**, 7505–7511 (1993).
19. T. J. Petzold, "Volume scattering functions for selected natural waters," *SIO Ref. 72–78* (Scripps Institution of Oceanography, 1972).
20. C. D. Mobley, *Light and Water; Radiative Transfer in Natural Waters* (Academic, 1994).
21. J. R. V. Zaneveld, A. Barnard, and E. Boss, "Theoretical derivation of the depth average of remotely sensed optical parameters," *Opt. Express* **13**, 9052–9061 (2005).
22. J. Piskozub, T. Neumann, and L. Wozniak, "Ocean color remote sensing: choosing the correct depth weighting function," *Opt. Express* **16**, 14683–14688 (2008).
23. H. R. Gordon and D. K. Clark, "Remote sensing optical properties of a stratified ocean: an improved interpretation," *Appl. Opt.* **19**, 3428–3430 (1980).
24. H. R. Gordon, M. R. Lewis, S. D. McLean, M. S. Twardowski, S. A. Freeman, K. J. Voss, and G. C. Boynton, "Spectra of particulate backscattering in natural waters," *Opt. Express* **17**, 16192–16208 (2009).
25. W. M. Balch, A. J. Plueddemann, B. C. Bowler, and D. T. Drapeau, "Chalk-Ex—the fate of CaCO_3 particles in the mixed layer: evolution of patch optical properties," *J. Geophys. Res.* **114**, C07020 (2009).

26. G. C. Boynton and H. R. Gordon, "An irradiance inversion algorithm for absorption and backscattering coefficients: improvement for very clear waters," *Appl. Opt.* **41**, 2224–2227 (2002).
27. R. M. Chomko, H. R. Gordon, S. Maritorena, and D. A. Siegel, "Simultaneous retrieval of oceanic and atmospheric parameters for ocean color imagery by spectral optimization: a validation," *Remote Sens. Environ.* **84**, 208–220 (2003).
28. C. P. Kuchinke, H. R. Gordon, and B. A. Franz, "Spectral optimization for constituent retrieval in Case 2 waters. I: implementation and performance," *Remote Sens. Environ.* **113**, 571–587 (2009).
29. C. P. Kuchinke, H. R. Gordon, L. W. Harding, Jr., and K. J. Voss, "Spectral optimization for constituent retrieval in Case 2 waters II: validation study in the Chesapeake Bay," *Remote Sens. Environ.* **113**, 610–621 (2009).
30. W. M. Balch, P. Holligan, S. Ackleson, and K. Voss, "Biological and optical properties of mesoscale coccolithophore blooms in the Gulf of Maine," *Limnol. Oceanogr.* **36**, 629–643 (1991).
31. W. M. Balch, K. Kilpatrick, P. M. Holligan, D. Harbour, and E. Fernandez, "The 1991 coccolithophore bloom in the central north Atlantic II: relating optics to coccolith concentration," *Limnol. Oceanogr.* **41**, 1684–1696 (1996).
32. K. J. Voss, W. M. Balch, and K. A. Kilpatrick, "Scattering and attenuation properties of *Emiliania huxleyi* cells and their detached coccoliths," *Limnol. Oceanogr.* **43**, 870–876 (1998).
33. H. R. Gordon, "Backscattering of light from disk-like particles: is fine-scale structure or gross morphology more important?," *Appl. Opt.* **45**, 7166–7173 (2006).
34. H. R. Gordon, "Backscattering of light from disk-like particles with aperiodic angular fine structure," *Opt. Express* **15**, 16424–16430 (2007).
35. J. R. Young and P. Ziveri, "Calculation of coccolith volume and its use in calibration of carbonate flux estimates," *Deep Sea Res. II* **47**, 1679–1700 (2000).
36. J. R. Young, J. M. Didymus, P. R. Brown, B. Prins, and S. Mann, "Crystal assembly and phylogenetic evolution in heterococcoliths," *Nature* **356**, 516–518 (1992).
37. H. R. Gordon, "Rayleigh-Gans scattering approximation: surprisingly useful for understanding backscattering from disk-like particles," *Opt. Express* **15**, 5572–5588 (2007).
38. B. T. Draine, and P. Flatau, "Discrete dipole approximation for scattering calculations," *J. Opt. Soc. Am. A* **11**, 1491–1499 (1994).
39. W. M. Balch, D. T. Drapeau, T. L. Cucci, R. D. Vaillancourt, K. A. Kilpatrick, and J. J. Fritz, "Optical backscattering by calcifying algae: separating the contributions of particulate inorganic and organic carbon fractions," *J. Geophys. Res.* **104**, 1541–1558 (1999).
40. C. F. Bohren and D. R. Huffman, *Absorption and Scattering of Light by Small Particles* (Wiley, 1983).
41. W. M. Balch, J. J. Fritz, and E. Fernandez, "Decoupling of calcification and photosynthesis in the coccolithophore *Emiliania huxleyi* under steady-state light limited growth," *Mar. Ecol. Prog. Ser.* **142**, 87–97 (1996).
42. Y. S. Nakamura, S.-Y. Suzuki, and J. Hiromi, "Development and collapse for a *Gymnodinium mikimotoi* red tide in the Seto Inland Sea," *Aquat. Microb. Ecol.* **10**, 131–137 (1996).
43. H. C. van de Hulst, *Light Scattering by Small Particles* (Wiley, 1957).
44. L. Karp-Boss and P. A. Jumars, "Motion of diatom chains in steady shear flow," *Limnol. Oceanogr.* **43**, 1767–1773 (1998).

Appendix 3

“Light scattering by randomly-oriented cylinders: Dependence on aspect ratio for refractive indices applicable for marine particles,” *Optics Express*, **19**, 4673–4691 (2011).

Light scattering and absorption by randomly-oriented cylinders: dependence on aspect ratio for refractive indices applicable for marine particles

Howard R. Gordon^{1,*}

¹Department of Physics, University of Miami, Coral Gables, Florida, USA

*hgordon@miami.edu

Abstract: Typically, explanation/interpretation of observed light scattering and absorption properties of marine particles is based on assuming a spherical shape and homogeneous composition. We examine the influence of shape and homogeneity by comparing the optics of randomly-oriented cylindrically-shaped particles with those of equal-volume spheres, in particular the influence of aspect ratio ($AR = \text{length/diameter}$) on extinction and backscattering. Our principal finding is that when $AR > \sim 3-5$ and the diameter is of the order of the wavelength, the extinction efficiency and the backscattering probability are close to those of an infinite cylinder. In addition, we show the spherical-based interpretation of extinction and absorption can lead to large error in predicted backscattering.

©2011 Optical Society of America

OCIS codes: (010.1030) Absorption; (010.4450) Oceanic optics.

References and links

1. S. G. Ackleson, "Optical determinations of suspended sediment dynamics in western Long Island Sound and the Connecticut River plume," *J. Geophys. Res.* **111**(C7), C07009 (2006), doi:10.1029/2005JC003214.
2. N. Hoepffner, and S. Sathyendranath, "Determination of major groups of phytoplankton pigments from absorption spectra of total particulate matter," *J. Geophys. Res.* **98**(C12), 22789–22803 (1993).
3. H. R. Gordon, and A. Y. Morel, *Remote Assessment of Ocean Color for Interpretation of Satellite Visible Imagery: A Review* (Springer-Verlag, 1983).
4. D. Stramski, E. Boss, D. Bogucki, and K. J. Voss, "The role of seawater constituents in light backscattering in the ocean," *Prog. Oceanogr.* **61**(1), 27–56 (2004).
5. H. R. Gordon, and T. Du, "Light scattering by nonspherical particles: application to coccoliths detached from *Emiliania huxleyi*," *Limnol. Oceanogr.* **46**(6), 1438–1454 (2001).
6. A. Quirantes, and S. Bernard, "Light scattering methods for modeling algal particles as a collection of coated and/or nonspherical scatterers," *J. Quant. Spectrosc. Radiat. Transf.* **100**(1-3), 315–324 (2006).
7. W. R. Clavano, E. Boss, and L. Karp-Boss, "Inherent Optical Properties of Non-Spherical Marine-Like Particles - From Theory to Observations," *Oceanogr. Mar. Biol.* **45**, 1–38 (2007).
8. H. R. Gordon, T. J. Smyth, W. M. Balch, G. C. Boynton, and G. A. Tarran, "Light scattering by coccoliths detached from *Emiliania huxleyi*," *Appl. Opt.* **48**(31), 6059–6073 (2009).
9. H. R. Gordon, "Backscattering of light from disklike particles: is fine-scale structure or gross morphology more important?" *Appl. Opt.* **45**(27), 7166–7173 (2006).
10. H. R. Gordon, "Backscattering of light from disk-like particles with aperiodic angular fine structure," *Opt. Express* **15**(25), 16424–16430 (2007).
11. L.-X. Zhang, J.-Z. Lin, and T. L. Chan, "Orientation distribution of cylindrical particles suspended in turbulent pipe flow," *Phys. Fluids* **17**(9), 093105 (2005).
12. L. Karp-Boss, and P. A. Jumars, "Motion of diatom chains in steady shear flow," *Limnol. Oceanogr.* **43**(8), 1767–1773 (1998).
13. C. F. Bohren, and D. R. Huffman, *Absorption and Scattering of Light by Small Particles* (Wiley-Interscience, 1983).
14. H. C. Van de Hulst, *Light Scattering by Small Particles*, (Wiley, 1957).
15. G. R. Fournier, and B. T. Evans, "Approximations to extinction from randomly oriented circular and elliptical cylinders," *Appl. Opt.* **35**(21), 4271–4282 (1996).

16. L. N. M. Duysens, "The flattening of the absorption spectrum of suspensions, as compared to that of solutions," *Biochim. Biophys. Acta* **19**(1), 1–12 (1956).
17. A. Morel, and A. Bricaud, "Theoretical results concerning light absorption in a discrete medium, and application to specific absorption of phytoplankton," *Deep-Sea Res.* **28**(11), 1375–1393 (1981).
18. A. Bricaud, and A. Morel, "Light attenuation and scattering by phytoplanktonic cells: a theoretical modeling," *Appl. Opt.* **25**(4), 571–580 (1986).
19. J. R. V. Zaneveld, and J. C. Kitchen, "The variation of inherent optical properties of phytoplankton near an absorption peak as determined by various models of cell structure," *J. Geophys. Res.* **100**(C7), 13,309–13,320 (1995).
20. B. T. Draine, "The discrete-dipole approximation and its application to interstellar graphite grains," *Astrophys. J.* **333**, 848–872 (1988).
21. B. T. Draine, and P. Flatau, "Discrete dipole approximation for scattering calculations," *J. Opt. Soc. Am. A* **11**(4), 1491–1499 (1994).
22. R. D. Haracz, L. D. Cohen, and A. Cohen, "Scattering of linearly polarized light from randomly oriented cylinders and spheroids," *J. Appl. Phys.* **58**(9), 3322–3327 (1985).
23. G. R. Fournier, and B. T. Evans, "Approximation to extinction efficiency for randomly oriented spheroids," *Appl. Opt.* **30**(15), 2042–2048 (1991).
24. M. Jonasz, and G. R. Fournier, *Light Scattering by Particles in Water, Theoretical and Experimental Foundations* (Academic Press, 2007).

1. Introduction

The inherent optical properties (IOPs) of particles suspended in natural waters are of interest in several areas of marine science: sediment properties and transport [1]; marine photosynthesis [2]; and remote sensing of ocean color [3]. The IOPs include the absorption coefficient (a), the scattering coefficient (b), the extinction coefficient $c = a + b$, the volume scattering function $\beta(\Theta)$ (Θ is the scattering angle), and the backscattering coefficient (b_b). The extinction coefficient is particularly important in sediment studies, the spectral absorption coefficient in photosynthesis, and the backscattering coefficient in remote sensing (water-leaving radiance $\propto b_b/a$).

For many years, the interpretation of measurements of the IOPs of particles suspended in natural waters (in particular the estimation of their refractive indices) has usually employed the assumption that the particles are spherically symmetric [4]. The development of electromagnetic scattering codes for computing the scattering from particles with more complex shapes has stimulated interest in the influence of particle shape on the IOPs [5–7]. Gordon and Du [5] and Gordon et al. [8] showed that a complex shape was required to reproduce the spectral variation and absolute magnitude of the backscattering cross section of coccoliths detached from the coccolithophore *E. huxleyi*. Gordon [9,10] showed that small-scale structures (size $\leq \lambda/4$) had little influence on the backscattering of disk-like particles. Clavano et al. [7] carried out a comprehensive study of scattering by spheroid-shaped particles (ellipses of revolution) in random orientation with refractive indices characteristic of particles suspended in water. They showed that the computed IOPs for such particles deviated significantly from those computed for spheres having the same volume and refractive index. The deviations increased as the aspect ratio of the spheroids increased. They also reported data suggesting that the most frequent aspect ratio of living marine particles was ~ 5 .

In this work, I consider in detail the dependence of IOPs on aspect ratio. Rather than spheroids, I use homogeneous and structured cylinders as the study particle, but make comparisons with similarly-sized spheroids. I consider refractive indices that are within the range expected for marine particles. I also assume throughout that the particles are in random orientation; however, if the particles have a preferred orientation the influence on the IOPs will be large, particularly on backscattering. Generally, particles embedded in an isotropic turbulent flow, will have a random orientation. In contrast, if they are embedded in non-isotropic turbulence [11] or in a shear flow, there will be a tendency for the particles to align with the flow. This tendency will be particularly important in aligning particles with large aspect ratios, e.g., diatom chains [12]. In the absence of data concerning particle orientation in the natural waters, we have no basis on which to assume any orientation other than random.

As the principal focus is to study the influence of aspect ratio on the IOPs, the particle diameters are of necessity limited by the storage requirements of the computer code used in the computations. The largest particle that could be examined has a volume-equivalent spherical diameter of $\sim 3.6 \mu\text{m}$, and an aspect ratio of 10.

The principal result of the study is that the extinction, scattering, and absorption efficiencies, as well as the scattering phase function, $\beta(\Theta)/b$, and the backscattering probability, b_b/b , become nearly independent of the aspect ratio (length/diameter) when it becomes greater than $\sim 3-5$. This implies that the IOPs of longer cylindrical particles can be inferred from those of particles with aspect ratios in this range.

I begin by reviewing scattering and absorption concepts for finite and infinite cylinders. Next I provide computed absorption and extinction efficiencies and backscattering probability of homogeneous and structured cylinders as a function of their diameter, refractive index, and aspect ratio. These are then compared to those of equal-volume spheres, showing that the spherical assumption is particularly poor at even moderate aspect ratios. Finally, I briefly compare scattering by cylinders and spheroids.

2. Review of light scattering and absorption concepts

2.1. Finite cylinders

For a cylinder (or any particle) of finite extent, the differential scattering cross section, $d\sigma_b(\Theta, \Phi)$ is given by

$$d\sigma_b(\Theta, \Phi) = \frac{\left(\vec{S}_b(\Theta, \Phi) \right)_{\text{Avg}} \cdot \hat{r}(\Theta, \Phi) dA}{\left| \left(\vec{S}_{\text{Inc}} \right)_{\text{Avg}} \right|}, \quad (1)$$

where $\left(\vec{S}_b(\Theta, \Phi) \right)_{\text{Avg}}$ is the time-averaged Poynting vector (irradiance) of the scattered field at the position \vec{r} in the direction (Θ, Φ) , $\hat{r}(\Theta, \Phi)$ is a unit vector from the scattering center to the detector of area dA with its normal parallel to $\hat{r}(\Theta, \Phi)$, and $\left(\vec{S}_{\text{Inc}} \right)_{\text{Avg}}$ is the time averaged Poynting vector of the incident field. The angle Θ is the angle between the direction of the incident radiation and $\hat{r}(\Theta, \Phi)$, and Φ is the angle between the scattering plane (plane containing the incident direction and \hat{r}) and a laboratory-fixed reference plane containing the incident direction. Using the fact that the solid angle subtended by the detector at the particle is $d\Omega = dA/r^2$, where r is the distance from the detector to the particle, this gives the conventional definition of the differential scattering cross section:

$$\frac{d\sigma_b(\Theta, \Phi)}{d\Omega} = r^2 \frac{\left(\vec{S}_b(\Theta, \Phi) \right)_{\text{Avg}} \cdot \hat{r}(\Theta, \Phi) dA}{\left| \left(\vec{S}_{\text{Inc}} \right)_{\text{Avg}} \right|}. \quad (2)$$

Far from the scattering center the scattered fields are $\propto 1/r$, so the scattered Poynting vector is $\propto \hat{r}/r^2$, and the differential cross section is independent of r . The total scattering cross section is defined by

$$\sigma_b = \int_{\Phi=0}^{\Phi=2\pi} \int_{\Theta=0}^{\Theta=\pi} \frac{d\sigma_b(\Theta, \Phi)}{d\Omega} \sin\Theta d\Theta d\Phi, \quad (3)$$

the backscattering cross section by

$$\sigma_{bb} = \int_{\Phi=0}^{\Phi=2\pi} \int_{\Theta=\pi/2}^{\Theta=\pi} \frac{d\sigma_b(\Theta, \Phi)}{d\Omega} \sin\Theta d\Theta d\Phi, \quad (4)$$

and the scattering phase function by

$$P(\Theta, \Phi) \equiv \frac{1}{\sigma_b} \frac{d\sigma_b(\Theta, \Phi)}{d\Omega}. \quad (5)$$

Now, if we average over all orientations of the particle (to represent a collection of identical, randomly-oriented, particles) these relationships are replaced by

$$\left\langle \frac{d\sigma_b(\Theta, \Phi)}{d\Omega} \right\rangle = r^2 \frac{\left\langle \left(\vec{S}_b(\Theta, \Phi) \cdot \hat{r}(\Theta, \Phi) \right)_{Avg} \right\rangle}{\left| \left(\vec{S}_{Inc} \right)_{Avg} \right|}, \quad (6)$$

$$\langle \sigma_b \rangle = \int_{\Phi=0}^{\Phi=2\pi} \int_{\Theta=\pi/2}^{\Theta=\pi} \left\langle \frac{d\sigma_b(\Theta, \Phi)}{d\Omega} \right\rangle \sin\Theta d\Theta d\Phi, \quad (7)$$

$$\langle \sigma_{bb} \rangle = \int_{\Phi=0}^{\Phi=2\pi} \int_{\Theta=\pi/2}^{\Theta=\pi} \left\langle \frac{d\sigma_b(\Theta, \Phi)}{d\Omega} \right\rangle \sin\Theta d\Theta d\Phi, \quad (8)$$

$$\langle P(\Theta, \Phi) \rangle \equiv \frac{1}{\langle \sigma_b \rangle} \left\langle \frac{d\sigma_b(\Theta, \Phi)}{d\Omega} \right\rangle, \quad (9)$$

where $\langle X \rangle \equiv \sum_{i=1}^N X_i / N$, with the index i referencing one of N appropriately chosen orientations of the particle. Note that the resulting $\langle P(\Theta, \Phi) \rangle$ is actually independent of Φ . The volume scattering function, $\beta(\Theta)$, and the scattering coefficient, b , of a collection of such (randomly-oriented) particles are given by

$$\beta(\Theta) = n \left\langle \frac{d\sigma_b(\Theta, \Phi)}{d\Omega} \right\rangle \quad \text{and} \quad b = n \langle \sigma_b \rangle, \quad (10)$$

where n is the number of such particles per unit volume. The backscattering coefficient is

$$b_b = 2\pi \int_{\Theta=\pi/2}^{\Theta=\pi} \beta(\Theta) \sin\Theta d\Theta, \quad (11)$$

and the backscattering probability is $\tilde{b}_b \equiv b_b / b = \langle \sigma_{bb} \rangle / \langle \sigma_b \rangle$. The scattering efficiency Q_b is defined by $Q_b \equiv \langle \sigma_b \rangle / \langle A_p \rangle$, where $\langle A_p \rangle$ is the orientationally-averaged projected area (shadow) of the particle.

By computing the net flow of energy into a large sphere surrounding the particle, one can determine the power absorbed by the particle and thus the absorption cross section σ_a [13]:

$$\sigma_a = - \frac{\oint_A \left(\vec{S}_i(\Theta, \Phi) \right)_{Avg} \cdot \hat{r}(\Theta, \Phi) dA}{\left| \left(\vec{S}_{Inc} \right)_{Avg} \right|}, \quad (12)$$

where $(\bar{S}_i(\Theta, \Phi))_{\text{Avg}}$ is the time-averaged Poynting vector of the total field on the sphere: incident *plus* scattered. Similarly, performing the orientational averaging, $\langle \sigma_a \rangle \equiv \sum_{i=1}^N (\sigma_a)_i / N$. The absorption coefficient, a , is defined by $a = n \langle \sigma_a \rangle$, and the absorption efficiency by $Q_a \equiv \langle \sigma_a \rangle / \langle A_p \rangle$. Finally, by combining the absorption and scattering cross sections, we obtain, respectively, the extinction, absorption, and scattering cross sections given by $\langle \sigma_c \rangle \equiv \langle \sigma_a \rangle + \langle \sigma_s \rangle$, $c \equiv a + b$, and $Q_c \equiv Q_a + Q_b$. Equations (1)–(12) provide operational definitions for most of the inherent optical properties of interest in marine optics (c is usually referred to as the beam attenuation coefficient).

2.2 Infinite cylinders

The problem of scattering of a plane electromagnetic wave from an infinite cylinder can be solved by separation of variables in cylindrical coordinates [13,14]. If a detector is placed a distance r from the origin of coordinates (located somewhere on the axis of the cylinder), for a given orientation of the cylinder the quantities defined in Eqs. (1)–(4) can be formally computed in a straightforward manner. If r is sufficiently large, the scattered fields are $\propto \sqrt{r}$, so both the differential and the total cross sections are $\propto r$; however, the scattering phase function is independent of r . Thus, the cross sections defined in this way lose their meaning as characteristics of the particle (they depend on how they are measured, i.e., r). Nevertheless, by constructing a large-diameter coaxial cylindrical surface of some length around the cylindrical particle, one can show that the scattering, absorption, and extinction cross sections *per unit length* are finite [13], so one can define scattering, absorption, and extinction efficiencies such that the cross sections of a given length of particle are finite, e.g., $\sigma_a = Q_a L D \cos \zeta$, where $\pi/2 - \zeta$ is the angle between the cylinder axis and the direction of the incident beam ($L D \cos \zeta$ is A_p for the length L of the cylindrical particle).

For infinite cylinders the orientational averaging of various quantities cannot be carried out in the normal way. The difficulty is that if one were to try to use Eq. (6), regardless of how large r is made, there will be some orientations for which the detector is not in the far-field zone (or scattered field zone). Thus, the notion of the scattered field (fields $\propto \sqrt{r}$) is not applicable for all orientations and a fixed r . In contrast, quantities that are independent of r , i.e., the Q 's, can be averaged over orientation in a straightforward manner [15], e.g., for a length L of cylinder, $\langle Q_s \rangle = \langle \sigma_s \rangle / \langle A_p \rangle = \langle Q_s A_p \rangle / \langle A_p \rangle = \langle Q_s \cos \zeta \rangle / \langle \cos \zeta \rangle$, etc. The scattering phase function is also independent of r , and one can formally define the its orientational average through $\langle P(\Theta, \Phi) \rangle \equiv [1/N] \sum_{i=1}^N P(\Theta, \Phi)$; however, this has no real physical meaning, as it cannot be used to retrieve an orientationally-averaged differential cross section.

3. Cylinders examined in the present work

The cylinders studied in this work are shown schematically in Fig. 1. The upper cylinder is homogeneous with refractive index $m_r - im_i$, relative to water. The lower cylinder (coated) has the same outer diameter (D) as the homogeneous cylinder, however the core diameter is $D/2$ and the core index is $m_r - 4im_i$. The index of the outer layer is $m_r - 0i$, so this simulates a situation in which the mass of absorbing material (or the number of absorbing molecules) is the same in the upper and lower cylinder, and allows simulation of the influence of the distribution of absorbing pigments in cylindrically shaped particles. In marine optics, there are two phenomena that are referred to as the “package effect.” The first is the difference in absorption between equal quantities of absorbing material in solution or in particles suspended in the same volume [16–18]. The second is the difference in absorption between cells in which the absorbing molecules are uniformly distributed within the cell walls, and cells in

which the absorbing molecules are packaged in smaller structures, e.g., chloroplasts [6,19]. It is the second that we examine by considering the two cases in Fig. 1.

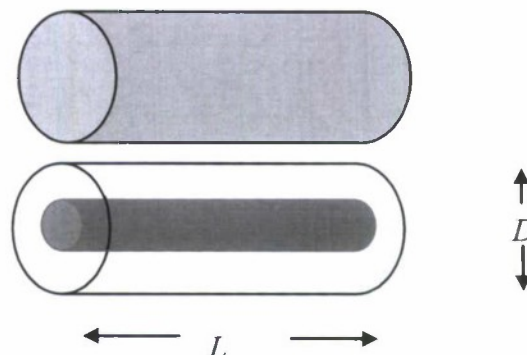


Fig. 1. Specifications of the cylinders examined in this study.

The computations were carried out for $D = 0.5, 1.0, 1.5, 2.0 \mu\text{m}$, $L = 0.5, 1.0, 3.0, 5.0, 7.0, 10.0, 15.0$, and $20 \mu\text{m}$, $\lambda = 400, 500, 600$, and 700 nm (in vacuum), and $m_r - im_i = 1.02, 1.05, 1.05 - 0.002i, 1.05 - 0.008i, 1.05 - 0.010i, 1.05 - 0.040i, 1.10, 1.15$, and 1.20 , relative to water. The discrete-dipole approximation code [20,21] DDSCAT 7.0 was used for most of the computations presented here. The orientational averaging was carried out in the manner prescribed in the DDSCAT code. This averaging is not optimum for scattering by a very long cylinder because for a given orientation the scattered light is in the form of a thin cone containing the incident beam and the axis of which cone is coincident with the axis of the cylinder [13]. The cone broadens as the cylinder's length decreases. A more robust formal of the averaging for long cylinders has been described by Haracz, et al. [22]; however, as we show later, we believe that averaging process in DDSCAT is sufficiently accurate for the cylinders studied here.

The computations were carried out on an 80 CPU cluster with a total memory of 160 GB. The dipole density was such that their lattice spacing was $\sim \lambda/18$ at 400 nm and $\sim \lambda/31$ at 700 nm. This insured that the backscattering cross section could be computed with an error $<$ about 5%. Even with the multi-processor cluster, the computations were very time consuming for the larger particles: ~ 10 days were required to compute the scattering (at 4 wavelengths) by a cylinder with $D = 1.5 \mu\text{m}$, $L = 15 \mu\text{m}$ and $m = 1.20$.

4. Extinction and absorption efficiencies

The extinction and absorption efficiencies were computed using from the orientationally-averaged extinction and absorption cross sections $\langle \sigma_c \rangle$ and $\langle \sigma_a \rangle$ through $Q_e \equiv \langle \sigma_c \rangle / \langle A_p \rangle$ and $Q_a \equiv \langle \sigma_a \rangle / \langle A_p \rangle$ where $\langle A_p \rangle = \pi D(L + D/2)/4$ is the orientationally-averaged projected area (shadow) of the particle. Using the computed efficiencies for finite-length cylinders, I asked several questions: (1) how do the efficiencies depend on the aspect ratio ($AR \equiv L/D$) and diameter of the cylinders?; (2) how do the efficiencies compare with those for an infinite cylinder with the same diameter?; and (3) how do the efficiencies depend on the distribution of absorbing material within the cylinders (Fig. 1)?

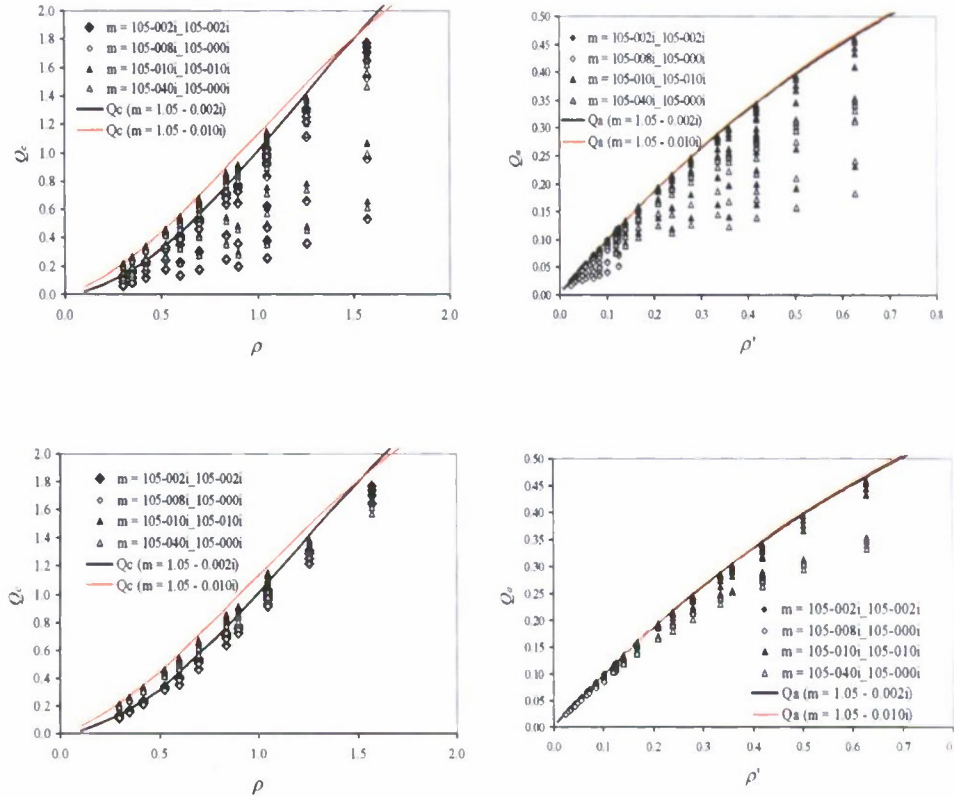


Fig. 2. Extinction and absorption efficiencies computed for randomly orientated, homogeneous or coated cylindrically shaped particles, given that their diameter and aspect ratio are known so that their orientationally-averaged projected area is $\pi D(L + D/2)/4$. Here, $\rho = 2\alpha(m_r - 1)$ and $\rho' = 4\alpha m_i$, where $m_r = im_i$, is the refractive index of the particle relative to water, and $\alpha = \pi D/\lambda$, with D the cylinder's (outer) diameter and λ the wavelength of light in the water. Solid lines are the exact computations for randomly orientated, infinite cylinders. The notation "m=1.05-0.040i_1.05-0.000i" indicates that the refractive index of the core is $1.05 - 0.040i$, and the refractive index of the coating is $1.05 - 0.000i$, etc. In the case of coated cylinders, ρ and ρ' are computed using the m_i of the associated homogeneous particle. Top: all aspect ratios (1/3 – 30). Bottom: all aspect ratios ≥ 3 .

Figure 2 provides the computed values of Q_c and Q_a for the all aspect ratios that were examined with absorbing cylinders ($m_i > 0$) and $m_r = 1.05$. The notation in the legend is explained in the figure caption. The upper two panels are for all aspect ratios (1/3 – 30) and the lower panels for $AR \geq 3$. The lines correspond to exact computations for infinite cylinders with the same diameter using the IPHASE code [15]. For the case with weaker absorption, the results clearly show that the efficiencies closely follow those for infinite cylinders as long as $AR \geq 3$, for both the coated and the homogeneous cylinders. For the case with stronger absorption, the "package effect," the decrease in absorption when the absorbing molecules are not uniformly distributed within the particle, results in lower absorption efficiency.

This packaging effect is displayed more clearly in Fig. 3, for which I provide the ratio of the absorption efficiencies Q_a for a coated cylinder with indices $m_{inside} = 1.05 - 0.040i$ and $m_{outside} = 1.05 - 0.000i$ ($Q_a(\text{Packaged})$) to that of a homogeneous cylinder $m_{inside} = m_{outside} = 1.05 - 0.010i$ ($Q_a(\text{Homo})$). Note that both cylinders contain the same number of absorbing

molecules. The figure shows that the effect of the absorbing pigment packaging is greatest in the blue region of the spectrum and for larger-diameter cylinders. The maximum decrease in Q_a due to the packaging is about 25%. Although the symbols do not differentiate between cylinder lengths, for a given diameter the packaging effect is smallest in the shortest cylinder and depends very little on the length once AR exceeds unity. In the case with less overall absorption, i.e., $m_{inside} = 1.05 - 0.008i$ and $m_{outside} = 1.05 - 0.000i$ compared to that of a homogeneous cylinder $m_{inside} = m_{outside} = 1.05 - 0.002i$, similar results are obtained; however, the maximum decrease in Q_a due to the packaging is only about 10% (Fig. 2.).

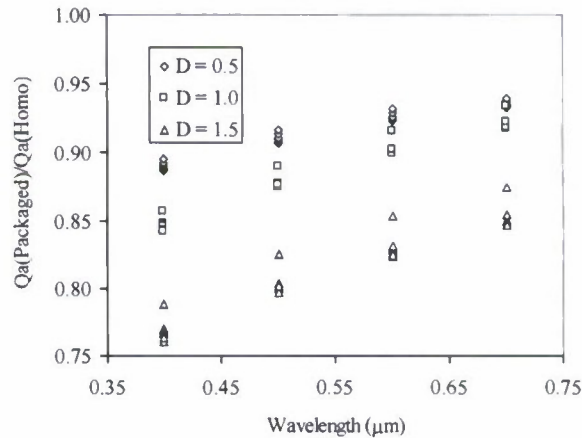


Fig. 3. This figure provides the ratio of absorption efficiencies (coated to homogeneous) of strongly absorbing cylinders as a function of wavelength. The diameter of the cylinder (in μm) is specified in the legend. For each diameter, the symbols refer to cylinder lengths ranging from 0.5 to 15 μm . The figure shows that the effect of the absorbing pigment packaging is greatest in the blue region of the spectrum and for larger-diameter cylinders. Although the symbols do not differentiate between cylinder lengths, for a given diameter the packaging effect is smallest in the shortest cylinder and depends very little on the length once the aspect ratio (length/diameter) exceeds unity.

The extinction efficiencies of finite cylinders with larger values of ρ are compared with those of infinite cylinders in Fig. 4. In this case the refractive index is 1.20 and since there is no absorption $Q_b = Q_c$. The figure clearly shows that for $AR \geq 3$, the extinction efficiency is again close to that of an infinite cylinder, with all cases except two differing by less than $\pm 10\%$ (RMS difference $\sim 5\%$).

Thus, it is clear that for homogeneous cylindrically-shaped particles with aspect ratios $>$ about 3, the extinction efficiency becomes close to that of an infinite cylinder, i.e., $Q_c(D, m, AR) \approx Q_c(D, m, \infty)$. This implies that $\langle \sigma_c(D, m, AR) \rangle \approx Q_c(D, m, \infty) \pi D^2 (AR + 1/2) / 4$, or for two aspect ratios AR and AR' (both $>$ about 3),

$$\frac{\langle \sigma_c(D, m, AR) \rangle}{(AR + 1/2)} \approx \frac{\langle \sigma_c(D, m, AR') \rangle}{(AR' + 1/2)}. \quad (13)$$

Similar expressions hold for the orientationally averaged absorption and scattering efficiencies. Although $Q_c(D, m, \infty)$ has not been computed for coated cylinders, presumably Eq. (15) should hold for such particles as well.

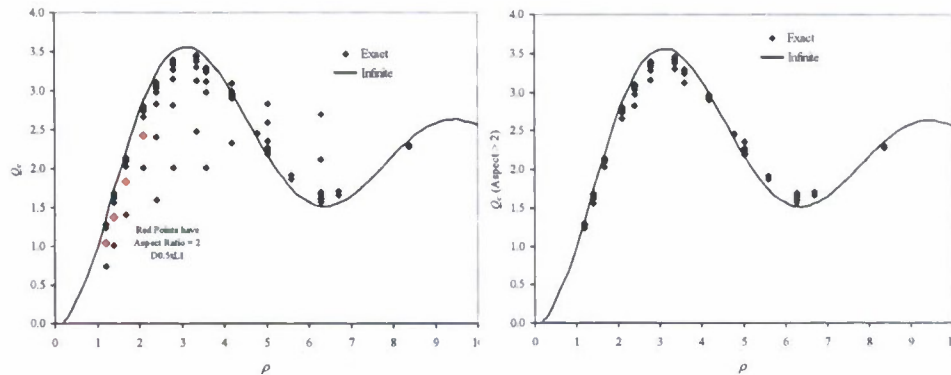


Fig. 4. Q_e as a function of ρ , computed for non-absorbing cylinders ($m = 1.20 - 0.000i$) with diameters (D) ranging from $0.5 \mu\text{m}$ to $2.0 \mu\text{m}$. Left: $0.25 \leq AR \leq 30$ (points colored in red are $AR = 2$). Right: $3 \leq AR \leq 30$. The solid curve is the extinction efficiency (for a unit length) of randomly-oriented infinite cylinders. As in Fig. 2, $\rho = 2\alpha(m-1)$ with $\alpha = \pi D/\lambda$.

5. Phase function and backscattering probability of cylinders

We have seen that the extinction and absorption efficiencies of micrometer-sized cylindrical particles depend little on the aspect ratios as long as $AR \geq 3$. Is this the case for the phase function and backscattering probability? I mentioned earlier that the default orientational-averaging scheme used in DDSCAT 7.0 was employed in the present computations. Is this default sufficient to provide orientational averaging for long cylinders? To examine this question, I computed the orientationally-averaged phase function (and \tilde{b}_b) for cylinders with small and large AR . To achieve the very large variation in AR , I used $D = 0.25 \mu\text{m}$. The results of this computation are shown in Fig. 5. One sees that with the exception of small scattering angles ($\Theta \leq 8^\circ$), as AR increases the computed phase function simply becomes “noisier.” This is what would be expected, as the scattering pattern (for a given orientation) degenerates into an infinitely thin cone as $L \rightarrow \infty$. Careful examination shows that there is a high correlation between the “noise” at $AR = 100$ and 200 , etc., as would be expected as the scattering cone thins. Since the thickness of the scattering cone depends mostly on λ / L (the thickness decreases as L increases), I conclude that for the values of L examined in this work ($\leq 25 \mu\text{m}$) the averaging procedure in DDSCAT is sufficiently accurate to yield reliable phase functions and backscattering probabilities.

Figure 6 provides another example of the weak dependence of the scattering phase function (and degree of linear polarization) on aspect ratio. Virtually the only differences in the phase function between $AR = 20$ and $AR = 3$ are the enhanced scattering near zero degrees and the deeper minima near 30° , 50° , 80° , and 130° for $AR = 20$. This weak dependence on aspect ratios as long as $AR \geq 5$ is also displayed by the backscattering probability as shown in Fig. 7 for a wide range of refractive indices and particle diameters.

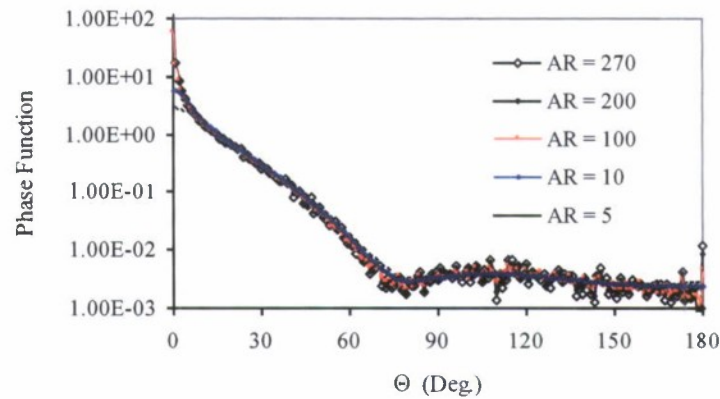


Fig. 5. Orientationally averaged scattering phase functions for long cylinders as a function of aspect ratio (AR). The values of the computed backscattering probabilities are 0.0212, 0.0212, 0.0209, 0.0218, and 0.0220, for $AR = 5, 10, 100, 200$, and 270 , respectively. The values of the extinction efficiency (Q_e) are 0.999, 1.007, 1.032, 1.033, 1.033, and 1.034 for $AR = 5, 10, 100, 200, 270$, and ∞ , respectively. The value of ρ for these efficiencies is 1.0472, so these computations fall very close to the continuous curve in Fig. 4. (Note, $L = 1.25, 2.50, 25.0, 50.0$, and $67.5 \mu\text{m}$ for $AR = 5, 10, 100, 200$, and 270 , respectively.) $D = 0.25 \mu\text{m}$, $m = 1.20$, $\lambda = 400 \text{ nm}$.

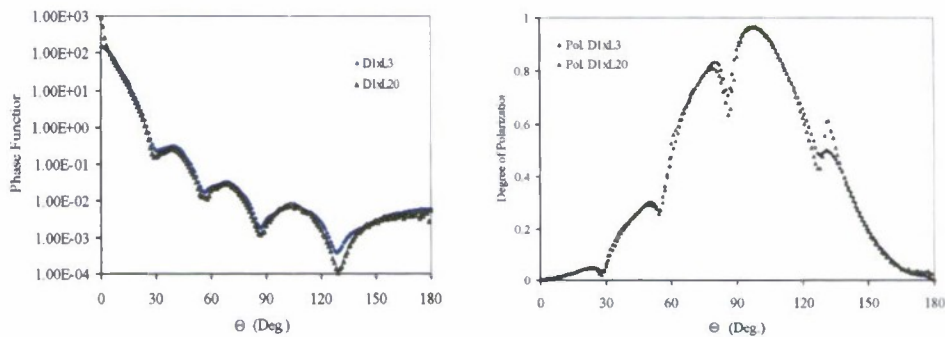


Fig. 6. Orientationally-averaged scattering phase functions (left) and degree of linear polarization (right) at 600 nm (vacuum) for homogeneous cylinders with a diameter of $1 \mu\text{m}$ and length of $3 \mu\text{m}$ ($D1 \times L3$) and $20 \mu\text{m}$ ($D1 \times L20$). The refractive index is $1.05 - 0.002i$. The oscillatory nature of the phase function is determined mostly by D/λ , but with some dependence on m .

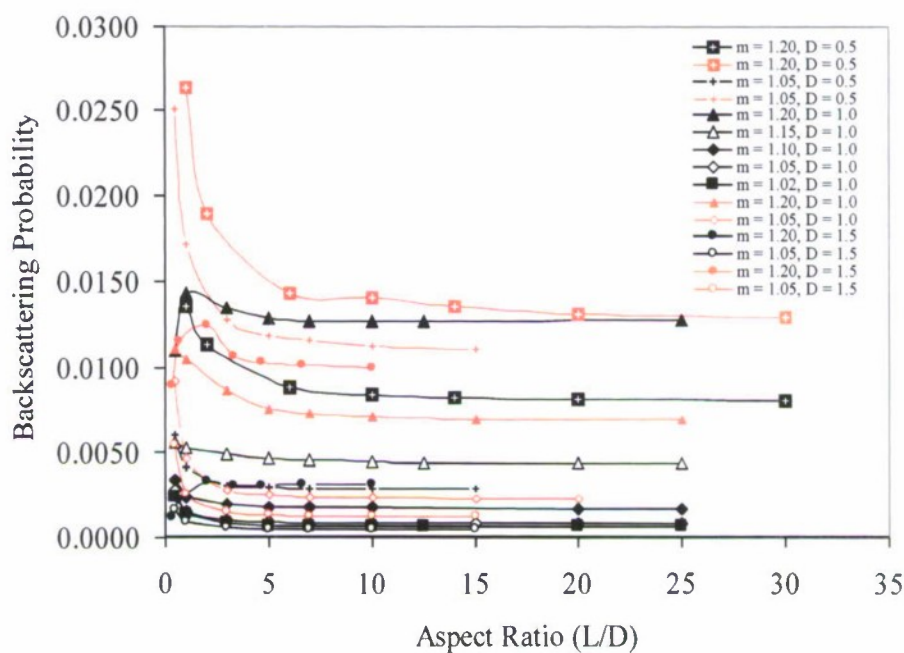
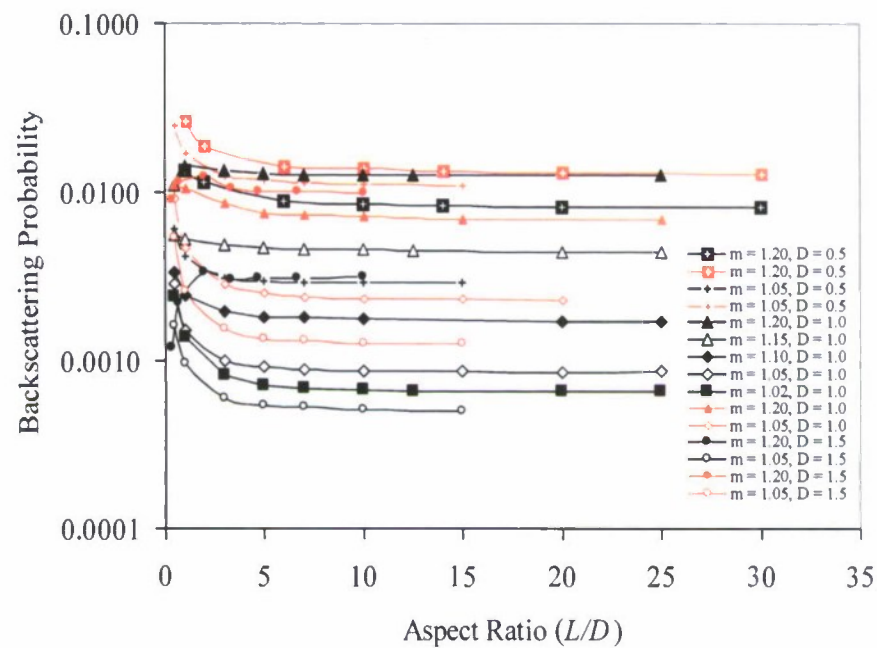


Fig. 7. Examples of the variation of the backscattering probability with aspect ratio for cylinder diameters between 0.5 and 1.5 μm and refractive indices ranging from 1.02 to 1.20. The black curves are for a vacuum wavelength of 400 nm and the red curves for 700 nm.

These computations show that when $AR >$ about 3–5, $\langle \sigma_{bb}(D, m, AR) \rangle \approx \bar{\sigma}_{bb}(D, m, \infty) \langle \sigma_b(D, m, AR) \rangle$, and in a manner similar to Eq. (13),

$$\frac{\langle \sigma_{bb}(D, m, AR) \rangle}{(AR+1/2)} \approx \frac{\langle \sigma_{bb}(D, m, AR') \rangle}{(AR'+1/2)}, \quad (14)$$

with both $AR' > AR \approx 3-5$ (Figs. 7 and 13). I used Eq. (14) to compute the orientationally averaged backscattering cross section for cylinders with $D = 1 \mu\text{m}$ and $AR' \geq 5$ from $AR = 3$ and for $AR' \geq 7$ from $AR = 5$ with $m = 1.05 - 0.010i$. The rms error was 2.5% for $AR = 3$ and 1.2% for $AR = 5$. Similar computations with $m = 1.20 - 0.000i$ resulted in rms errors of 8.1% and 2.6% for $AR = 3$, and 5, respectively.

6. Cylinders compared to equal-volume spheres

A well-known approach to estimating the complex refractive index of marine particles, e.g., phytoplankton, is to measure their extinction and absorption coefficients and the particle volume (e.g., with a Coulter Counter). The particles are then assumed to be homogeneous spheres and the extinction and absorption efficiencies are computed. Real and imaginary parts of the refractive index are then found which, for a spherical particle, would yield the same extinction and absorption efficiencies (see, for example, Ref. 18). I have tested this approach using the extinction and absorption cross sections described above for cylinders. Rather than using the exact computation of Q_c and Q_a for spheres, it is much simpler to use the analytical formulas of the van de Hulst anomalous diffraction approximation for the scattering and absorption efficiencies of a homogeneous sphere. These are [14]

$$Q_a(\rho') = 1 + 2 \frac{\exp(-\rho')}{\rho'} + 2 \frac{\exp(-\rho') - 1}{\rho'^2}, \quad (15)$$

and

$$Q_c(\rho) = 2 - 4 \exp(-\rho \tan \beta) \left[\frac{\cos \beta}{\rho} \sin(\rho - \beta) + \frac{\cos^2 \beta}{\rho^2} \cos(\rho - 2\beta) \right] + 4 \frac{\cos^2 \beta}{\rho^2} \cos(2\beta). \quad (16)$$

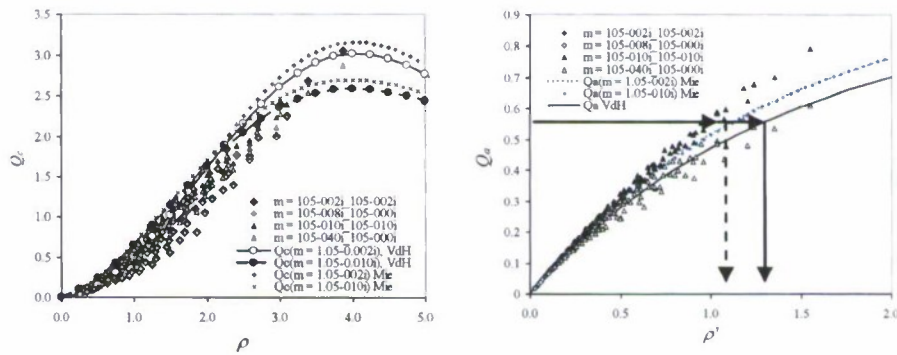


Fig. 8. The extinction (left) and absorption (right) efficiencies computed by dividing the associated cross sections by the projected area of a *volume-equivalent* sphere as a function of ρ and ρ' . Here, $\rho = 2\alpha(m_r - 1)$ and $\rho' = 4\alpha m_i$, where $m_r - im_i$ is the refractive index of the particle relative to water, and $\alpha = \pi d/\lambda$, where d is now the diameter of the *volume-equivalent* sphere. For a given experimentally-determined Q_a , the dashed vertical arrow provides the correct ρ' (and, hence m_i), while the solid vertical arrow provides the retrieved value of m_i .

where $\rho = 2\alpha(m_r - 1)$, $\rho' = 4\alpha m_i$, $\tan \beta = m_i/(m_r - 1)$, and $\alpha = \pi d/\lambda$, with d the sphere's diameter and λ the wavelength of light in the water. In this analysis, we take d to be the diameter of a sphere with the same volume as the cylinder, i.e., the *equal-volume sphere*. Fig. 8 provides the extinction and absorption efficiencies computed assuming the spherical shape, e.g., $Q_a \equiv 4\langle\sigma_a\rangle/\pi d^2$, along with Q_c and Q_a computed with the Van de Hulst anomalous diffraction theory (VdH), and with exact the Mie theory (MIE). There are three important observations to be made from Fig. 8: (1) the volume-equivalent sphere assumption is not very good in the case of Q_c (left figure) even if full Mie theory is used; (2) the volume-equivalent sphere assumption is better in the case of Q_a (right figure), especially if full Mie theory is used; and (3) the package effect, while relatively unimportant for Q_c , is important in Q_a (right figure) for the case with stronger absorption, but not for the case with weaker absorption.

How much error does the deviation of the derived Q_c and Q_a from Eqs. (18) and (19) make in estimating the refractive index? Given the volume of the particle, and assuming a spherical shape, d and α are determined. Calculations of the beam attenuation coefficient and absorption coefficients for coated cylinders were inserted into Eqs. (15) and (16) to find m_r and m_i . Figure 9 provides the resulting computations for a coated cylinder with indices $m_{\text{inside}} = 1.05 - 0.040i$ and $m_{\text{outside}} = 1.05 - 0.000i$, and all combinations of diameter and length. Recall that the package effect is larger for this case. Ideally one should derive an index of $1.05 - 0.010i$, based on the concentration of absorbing material. Clearly, m_i is retrieved to within $\pm 20\%$ with an average (over all sizes) close to 0.010, and the retrieved m_r appears to be too low in almost all cases, but averages ~ 1.044 . One notes that if the exact Mie theory were used in the retrieval of m_i (Fig. 8) the retrieved values would be about 10% larger than shown in Fig. 9 due to the

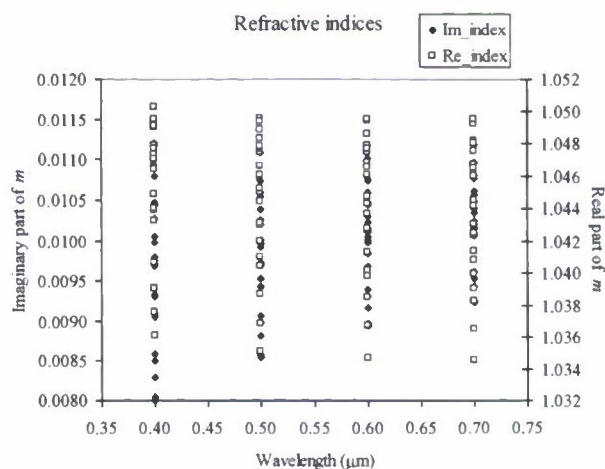


Fig. 9. An example of retrievals of the real and imaginary parts of the refractive index for coated cylinders for all the combinations of diameter and length, using the van de Hulst approximation. Ideally one should derive a real part of 1.05 and an imaginary part of 0.010. The scatter shows that m_i is retrieved to within $\pm 20\%$ (somewhat better in the red) with an average (over all sizes) close to 0.010, and that the retrieved m_r appears to be too low in almost all cases, but averages ~ 1.044 .

inaccuracy of the Van de Hulst approximation to Q_a [Eq. (15)]. However, the exact Mie results cannot actually be used because m_r is required, and as we see in the figure, it is strongly dependent on AR . Thus, it is clear that measuring particle volume and the extinction and absorption cross sections, assuming the particles are spherical, then applying Eqs. (15) and (16) does yield meaningful results for m_i even for particles with large aspect ratios;

however, the retrieved values of m_r depend strongly on the aspect ratio. It is interesting to note that if one employed the homogeneous infinite-cylinder assumption in the analysis of the cross sections (Fig. 2) for this example, the error in the retrieved m_i would actually be larger than for the equivalent-volume sphere approach: accurate retrieval would require consideration of the package effect, probably by using a coated infinite-cylinder retrieval model.

For larger values of the refractive index of the cylinder, this method fails completely when the cylinder becomes too large. A dramatic example of this failure is provided in Fig. 10, which shows Q_c for cylinders determined from the cross-sectional area of the equal-volume sphere (in a manner identical to that in Fig. 8), and ρ evaluated using the diameter of the equal-volume sphere. The thick solid line in the figure is the Van de Hulst approximation to Q_c . Note that for $\rho > \text{about } 3$, for most cases shown, there is no refractive index value for equal-volume spheres that can produce the associated extinction efficiency. Thus, this method often fails to provide *any* value for m .

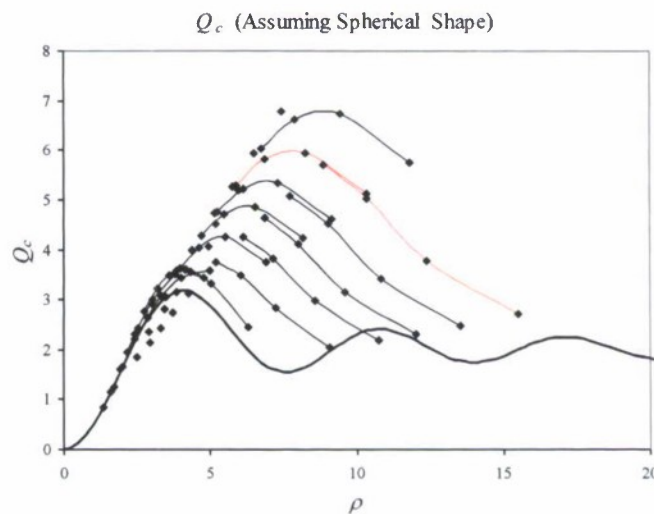


Fig. 10. The extinction efficiency computed by dividing the associated extinction cross section by the projected area of a *volume-equivalent* sphere as a function of ρ . Here, $\rho = 2a(m_r - 1)$ and $a = \pi d/\lambda$, where d is the diameter of the *volume-equivalent* sphere. Points for some given diameters and lengths are connected by smooth curves (for which λ varies from 400 to 700 nm). The red curves are for diameters of 1.0 and 1.5 μm with $AR = 10$. The thick curve is the Van de Hulst approximation to Q_c for spheres.

Given the values of m_r and m_i derived from measurements of the absorption and extinction efficiencies, the particle volume, and the assumption of sphericity (using the methodology described above, when it works, i.e., for low-index cylinders), how well does the predicted backscattering cross section reproduce the actual backscattering cross section of cylindrical particles? To shed light on this question, I used the retrieved refractive indices shown in Fig. 9 and Mie theory to compute $\sigma_{bb}^{(Sph)}$ for comparison with its cylindrical counterpart $\sigma_{bb}^{(Cyl)}$ for each wavelength and particle size. The ratio $R = \sigma_{bb}^{(Cyl)} / \sigma_{bb}^{(Sph)}$ shows some spectral variation, but to gain a better perspective on the influence of particle shape, I averaged R over the visible spectrum for each size. Figure 11 (black points/lines) shows the resulting R for particles with diameters ~ 1 -3 times the wavelength as a function of the aspect ratio. The red points/lines on the figure provide R values when the true value of the cylinder's refractive index is used to compute the backscattering the sphere, rather than that determined from particle extinction, absorption, and volume. We note that for cylinders in this size range, R is greater than 1 and

increases approximately linearly with aspect ratio. The large values of R when the index is retrieved from extinction, etc., is due to the increased error in the derived values of m_r as the aspect ratio increases (the retrieved m_r becomes smaller as the aspect ratio increases, and $\sigma_{bb}^{(Sph)}$ is a strong function of m_r). Thus, the extinction, absorption, volume, and sphericity-assumption methodology cannot yield reliable values of the backscattering cross section of cylindrically shaped particles with even moderate (>5) aspect ratios; however, if the correct refractive index is known and used in the computation, the backscattering of the equal-volume sphere is much closer to that of the cylinder.

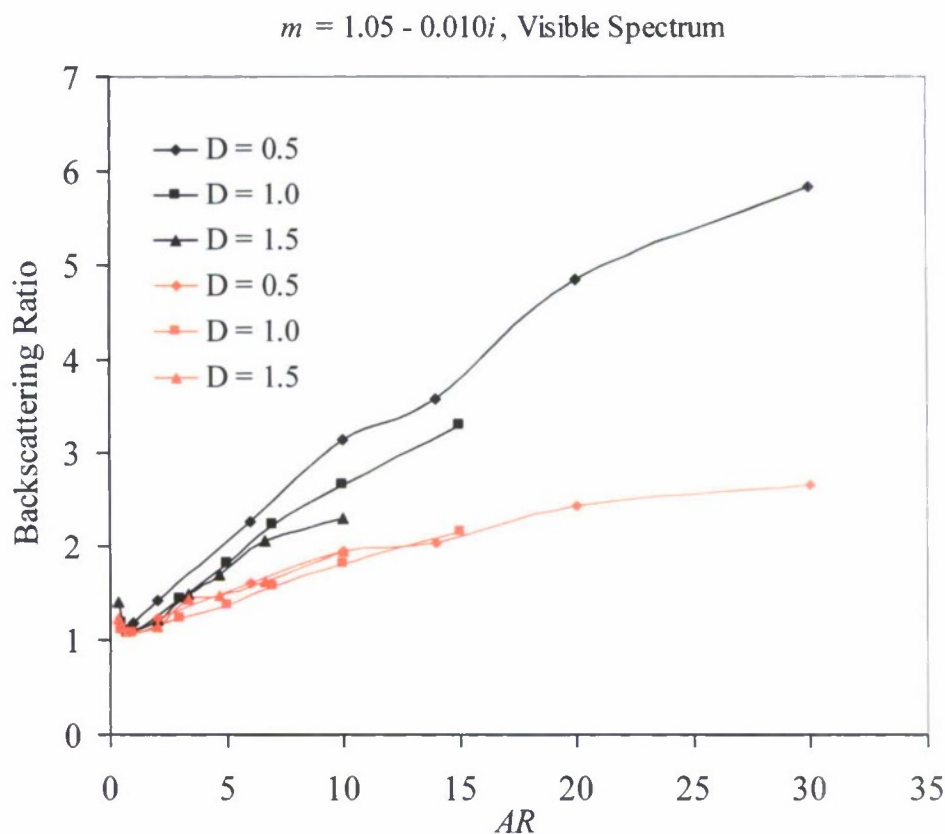


Fig. 11. Backscattering by a cylinder divided by backscattering by an equal-volume sphere. Black curves: refractive index in the computation of σ_{bb} for spheres is that derived using the refractive index determined from the extinction and absorption cross sections using the equivalent-volume sphere assumption. Red curves: refractive index in the computation of σ_{bb} for spheres is the same value used for the cylinders, i.e., the correct value. Diameter (D) is in micrometers, and the true value of the refractive index is $1.05 - 0.010i$.

The backscattering ratio R for the higher index ($1.20 - 0.000i$) is shown in Fig. 12. Note that in this case $\sigma_{bb}^{(Cyl)} < \sigma_{bb}^{(Sph)}$. Thus, in the size range examined here, backscattering by cylinders appears to be larger than equal-volume spheres at low refractive indices and smaller at high refractive indices.

Absorption appears to have only a small effect on the backscattering by cylinders; however, the packaging of the absorbing substance within the cylinder can have a significant effect, especially when the absorption is large. Figure 13 provides the backscattering probability for cylinders (homogeneous and packaged) for all cases studied with $m_r = 1.05$.

Note that when the absorption is weak ($m_i = 0.002$ with a homogeneous distribution of absorbing molecules, \blacksquare , or $m_i = 0.008$ with the absorbing molecules confined

$$m = 1.20 - 0.000i, \lambda = 400 \text{ nm}$$

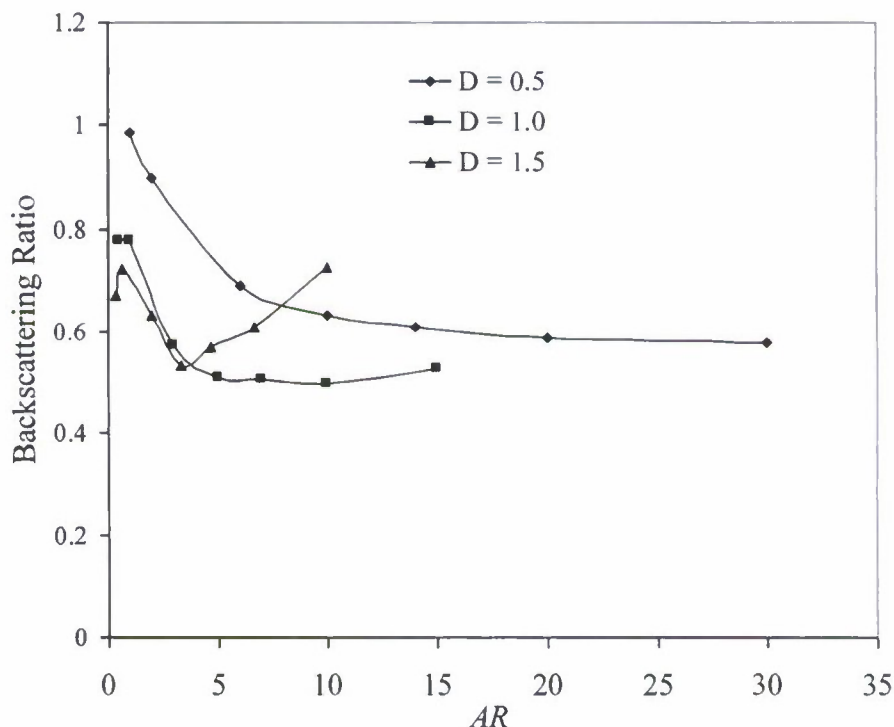


Fig. 12. Backscattering by a cylinder divided by backscattering by an *equal-volume* sphere. As the refractive index in this case cannot be derived from the extinction efficiency, in the computation of σ_{bb} for spheres m is the same value used for the cylinders. Diameter (D) is in micrometers, the wavelength is 400 nm, and the true value of the refractive index is $1.20 - 0.000i$.

to the inner cylinder of Fig. 1, \blacktriangle) there is little difference in the backscattering probability and that of a non-absorbing cylinder (\blacklozenge). In contrast, for the more strongly absorbing, homogeneous (\diamond) or packaged (\square), cylinders, absorption clearly influences the backscattering probability with larger values for the packaged case.

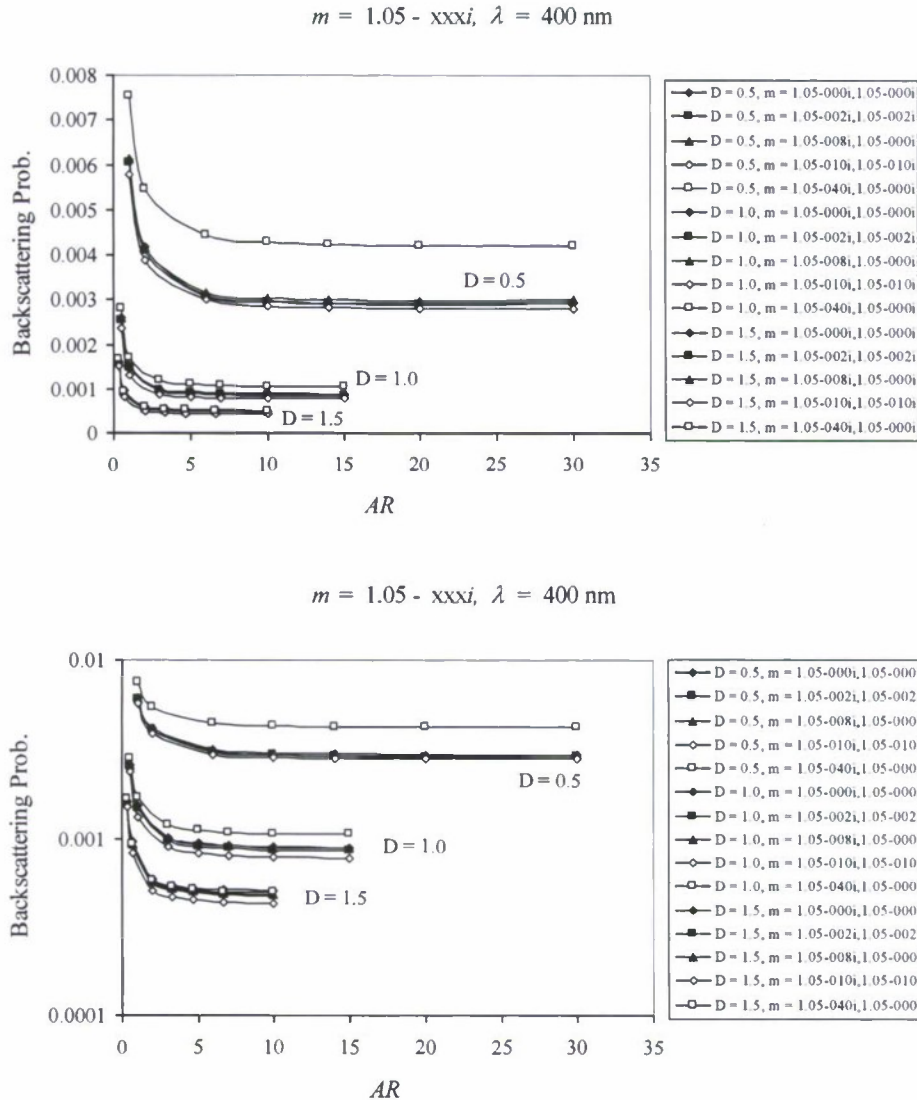


Fig. 13. Backscattering probability as a function of aspect ratio and the imaginary part of the refractive index for non-absorbing to strongly absorbing, homogeneous and structured cylinders. D is in micrometers.

7. Comparison with spheroids

A limited number of computations have been carried out for prolate spheroids to see if the conclusions regarding the influence of aspect ratio on light scattering by cylinders applies to spheroids. Fournier and Evans [23] have provided a highly accurate anomalous diffraction approximation to Q_c for spheroids. If one uses their relationships for a spheroid with minor axes D and major axis L ($AR = L/D$), it is seen that Q_c becomes almost independent of AR for $AR >$ about 3. I have carried out computations (using DDSCAT) for spheroids with $D = 0.5, 1.0$, and $1.5 \mu\text{m}$, and $AR = 3, 5$, and 10 , for $m = 1.05 - 0.010i$ and $m = 1.20 - 0.000i$. The resulting values of Q_c (and Q_a) are virtually independent of AR and agree well with the Fournier and Evans [23] result for large AR (e.g., $AR = 100$).

The independence of the backscattering probability on AR for $AR \geq 3$ for cylinders is also seen for spheroids of similar size. The results presented in Table 1 suggest that the backscattering probability for spheroids becomes essentially constant for $AR >$ about 5. Thus, our conclusions regarding the dependence

Table 1. The RMS the Backscattering Probability for Spheroids with Aspect Ratio $AR = 10$ to that for Spheroids with the Same Minor Axes but Aspect Ratio AR . $D = 0.5, 1.0$, and $1.5 \mu\text{m}$, and $\lambda = 400, 500, 600$, and 700 nm

m	$AR = 3$	$AR = 5$
$1.05 - 0.010i$	10.9	3.4
$1.20 - 0.000i$	18.6	2.5

of light scattering properties on AR for cylinders appear to apply equally well to spheroids.

It should be noted that when D and L are $\ll \lambda$, and the polarizabilities are determined in the electrostatic approximation (Rayleigh approximation [13,14]), the total scattering for spheroids is proportional to the square of the volume times a factor that is dependent on AR . This latter factor becomes nearly independent of AR for $AR > \sim 3$ for the refractive indices of interest here. In this case, $\sigma_b \propto (D^2 L)^2 = D^6 AR^2$, and

$$\frac{\langle \sigma_b(D, m, AR) \rangle}{AR^2} \approx \frac{\langle \sigma_b(D, m, AR') \rangle}{AR'^2}. \quad (17)$$

Equation (17) replaces Eq. (13) in this regime, and since $\bar{\sigma}_{bb} = 1/2$, independent of AR , a similar expression replaces Eq. (14). Again, similar expressions also apply to cylinders.

8. Concluding remarks

As stated in the abstract, I have shown the extinction, absorption, and scattering efficiencies, and the backscattering probability of randomly oriented, homogeneous and structured, cylinders become nearly independent of the aspect ratio when $AR > \sim 3$ –5, for refractive indices characteristic of marine particles (organic and inorganic). This applies to cylinders with diameters in the range 0.25 to $1.5 \mu\text{m}$ when illuminated with visible light (wavelength, 400 – 700 nm). Some long-chain phytoplankton, e.g., *Prochlorotrix hollandica*, fall in this size range [24]. It should also apply to much larger cylindrically-shaped particles, i.e., in sizes for which geometrical optics is applicable. Computational schemes for intermediate sized cylinders with high aspect ratios are not available; however, as the validity of the observation does not appear to depend on the actual diameter of the cylinders (Figs. 7 and 13) in the size ranges examined, one would expect that it would apply to intermediate sized particles as well. A limited number of computations for prolate spheroids suggest that the observations apply equally well to particles with this shape. This should simplify the inclusion of AR -distributions in the characterization of scattering by marine particles.

In order to interpret measured particle extinction and absorption cross sections to obtain the refractive index for single-species of phytoplankton, it is of course best to use a close approximation to the particle's shape in the necessary model calculations, i.e., there is no canonical shape that can be used for all particles. For cylindrical particles with aspect ratios greater than 3, it appears that infinitely-long cylinders (homogeneous or coated) with the same diameter (shorter dimension) are adequate for estimation of the refractive index. For other particles, other shapes will be appropriate; however, I expect that for particles that can be represented by "simple" shapes, e.g., spheroids, linear chains of spheres or spheroids (homogeneous or coated), etc., the cross sections will be proportional to the length, and the efficiencies will depend mostly on diameter for aspect ratios 3 or greater, as they do for cylinders. For the commonly used equivalent-volume-sphere approximation to obtain refractive index [18], we found that for cylinders the absorption index (m_i) can be determined with reasonable accuracy, i.e., $\sim \pm 20\%$, when m_r is low as it usually is for phytoplankton [24].

Remarkably, this approximation is actually better in retrieving m_i than using a homogeneous cylinder to model (incorrectly) a coated cylinder (Fig. 2). This suggests that in the absence of shape information, the equivalent-volume-sphere approximation is capable of yielding realistic estimates of m_i for low- m_r particles that deviate significantly from spheres. When m_r is high, the method fails completely (Fig. 10), and a more appropriate shape is required to interpret the observed cross sections.

In the case of backscattering, for the low index particles we examined, using the index retrieved through the equal-volume-sphere assumption, and computing σ_{bb} for the equal-volume sphere, can lead to an underestimation ($\sigma_{bb}^{(Cyl)} > \sigma_{bb}^{(Sph)}$) of cylinder backscattering by a significant factor (Fig. 11), largely because of the inaccuracy in estimation of m_r ; however, if the correct value of the refractive index is known, the error is significantly decreased. For the high-index case (for which the equal-volume-sphere analysis fails), given the correct value of the refractive index, the equal-volume sphere backscatters more than the cylinder, i.e., $\sigma_{bb}^{(Cyl)} < \sigma_{bb}^{(Sph)}$. Thus, prediction of σ_{bb} by this method for low index particles could account for some of the “missing” backscattering suggested for marine particles [4]; however, when the correct index is used in the computations, the underestimation is greatly reduced or eliminated completely.

Although the computations presented here represent a grossly inadequate span of cylinder sizes due to inadequate computer resources, they do suggest the manner in which particles with high aspect ratios can be included in scattering computations carried out at lower aspect ratios, particularly when the diameter of the particle is of the order of λ .

Acknowledgments

The author thanks Bruce Draine for providing the DDSCAT code used for most of the computations, and Georges Fournier for providing the IPHASE25 program for computing the scattering by infinite cylinders and the extinction of spheroids. This research was supported by the Office of Naval Research/ Environmental Optics Program, Grant Number N00014-07-1-0226.

Appendix 4

“Rayleigh-Gans scattering approximation: surprisingly useful for understanding backscattering from disk-like particles?” *Optics Express*, **15(9)**, 5572–5588 (2007).

Rayleigh-Gans scattering approximation: surprisingly useful for understanding backscattering from disk-like particles

Howard R. Gordon

Department of Physics, University of Miami, Coral Gables, FL 33214

Abstract: Recent computations of the backscattering cross section of randomly-oriented disk-like particles (refractive index, 1.20) with small-scale internal structure, using the discrete-dipole approximation (DDA), have been repeated using the Rayleigh-Gans approximation (RGA). As long as the thickness of the disks is approximately 20% of the wavelength (or less), the RGA agrees reasonably well quantitatively with the DDA. The comparisons show that the RGA is sufficiently accurate to be useful as a quantitative tool for exploring the backscattering features of disk-like particles with complex structure. It is used here to develop a zeroth-order correction for the neglect of birefringence on modeling the backscattering of detached coccoliths from *E. huxleyi*.

© 2007 Optical Society of America

OCIS codes: (010.4450) Ocean optics; (290.1350) Backscattering.

References and links

1. H. R. Gordon and A. Y. Morel, *Remote Assessment of Ocean Color for Interpretation of Satellite Visible Imagery: A Review* (Springer-Verlag, 1983).
2. D. A. Siegel, A. C. Thomas, and J. Marra, "Views of ocean processes from the Sea-viewing wide field-of-view sensor mission: introduction to the first special issue," *Deep Sea Res.* **11**, 51 1-3 (2004).
3. D. Stramski, E. Boss, D. Bogucki, and K. J. Voss, "The role of seawater constituents in light backscattering in the ocean," *Prog. Oceanogr.* **61**, 27-56 (2004).
4. M. I. Mishchenko, L. D. Travis, and A. A. Lacis (Cambridge, 2002).
5. H. R. Gordon and T. Du, "Light scattering by nonspherical particles: application to coccoliths detached from *Emiliania huxleyi*," *Limnol. Oceanogr.* **46**, 1438-1454 (2001).
6. W. M. Balch, P. M. Holligan, S. G. Ackleson, and K. J. Voss, "Biological and optical properties of mesoscale coccolithophore blooms in the Gulf of Maine," *Limnol. Oceanogr.* **34**, 629-643 (1991).
7. W. M. Balch, K. Kilpatrick, P. M. Holligan, D. Harbour and E. Fernandez, "The 1991 coccolithophore bloom in the central north Atlantic II: Relating optics to coccolith concentration," *Limnol. Oceanogr.* **41**, 1684-1696 (1996).
8. T. J. Smyth, G. F. Moore, S. B. Groom, P. E. Land and T. Tyrrell, Optical modeling and measurements of a coccolithophore bloom, *Appl. Opt.* **41**, 7679-7688 (2002).
9. H. R. Gordon, G. C. Boynton, W. M. Balch, S. B. Groom, D. S. Harbour, and T. J. Smyth, "Retrieval of Coccolithophore Calcite Concentration from SeaWiFS Imagery," *Geophys. Res. Lett.* **28**, 1587-1590, (2001).
10. W. M. Balch, H. R. Gordon, B. C. Bowler, D. T. Drapeau and E. S. Booth, "Calcium carbonate measurements in the surface global ocean based on Moderate-Resolution Imaging Spectroradiometer data," *J. Geophys. Res.* **110C**, C07001 (2005), doi:10.1029j2004JC002560.
11. H. R. Gordon, "Backscattering of light from disk-like particles: is fine-scale structure or gross morphology more important?" *Appl. Opt.* **45**, 7166-7173 (2006).
12. B. T. Draine, "The discrete-dipole approximation and its application to interstellar graphite grains," *Astrophys. J.* **333**, 848-872 (1988).
13. B. T. Draine and P. Flatau, "Discrete-dipole approximation for scattering calculations," *J. Opt. Soc. Am. A* **11**, 1491-1499 (1994).
14. C. F. Bohren and D. R. Huffman, *Absorption and Scattering of Light by Small Particles* (Wiley, 1983).
15. H. C. van de Hulst, *Light Scattering by Small Particles* (Wiley, 1957).
16. L. D. Cohen, R. D. Haracz, A. Cohen, and C. Acquista, "Scattering of light from arbitrarily oriented cylinders," *Appl. Opt.* **22**, 742-748 (1983).
17. K. Shimizu, "Modification of the Rayleigh-Debye approximation," *J. Opt. Soc. Am.* **73**, 504-507 (1983).

18. B. T. Draine and J. Goodman, Beyond Clausius-Mossotti: Wave propagation on a polarizable point lattice and the discrete dipole approximation, *Astrophys. J.* **405**, 685-697 (1993).
19. J. R. Young, J. M. Didymus, P. R. Brown, B. Prins, and S. Mann, "Crystal assembly and phylogenetic evolution in heterococcoliths," *Nature* **356**, 516-518 (1992).
20. E. Aas, Refractive index of phytoplankton derived from its metabolite composition, *J. Plankton Res.* **18**, 2223-2249 (1996).
21. J. M. Bennett and H. E. Bennett, "Polarization," in *Handbook of Optics*, W.G. Driscoll and W. Vaughan, eds., (McGraw-Hill, 1978).

1. Introduction

Satellite remote sensing of ocean color [1] is now a well-developed tool for studying phytoplankton dynamics on regional to global scales ([2], and papers therein). The term "ocean color" refers to the water-leaving spectral radiance, i.e., the radiance resulting from the backscattering of sunlight *out* of the water. This radiance is proportional to the ratio of the backscattering coefficient b_b (the differential scattering cross section per unit volume integrated over the backward *hemisphere*) and the absorption coefficient a of the medium (water plus constituents) [1], i.e., b_b/a . Thus, understanding the backscattering coefficient of the suspended constituents of the natural waters is a central problem in marine optics. However, the backscattering coefficient of marine particles is arguably the poorest known of the inherent optical properties of natural waters [3], and much effort is being focused on remedying this situation. The inherent optical properties of marine particles are most-often modeled as homogeneous spheres using Mie Theory. Although this approach has been fruitful, the next logical step in modeling marine particles is to abandon the normally-employed spherical approximation and use more realistic approximations to their shape. The advent of computer codes capable of handling more complex shapes [4], and the increased computational speeds now available, suggest that particle modeling employing simple non-spherical shapes, e.g., disks, rods, etc., could become routine. Gordon and Du [5] used a two-disk model to try to reproduce the backscattering by coccoliths detached from *E. huxleyi*. This particular marine particle was chosen for study because (1) its shape is rather precisely known, resembling a disk or two roughly parallel disks; (2) its composition is known (Calcite), providing its refractive index relative to water (~ 1.20); (3) its backscattering properties have been measured [6-8]; and (4) it is amenable to remote sensing [9,10]. They found that, while the resulting spectral variation of the backscattering cross section agreed with experiment, its magnitude was low by a factor of 2-3. Such simple shapes are still at best poor approximations to real particles. Thus, to try to understand this discrepancy, I asked [11] the following question: how far can the actual shape of a particle deviate from these simple shapes and still be realistically modeled by them? To shed some light on this issue, I used discrete dipole approximation (DDA) solutions [12, 13] to the scattering problem to investigate the backscattering by disk-like particles possessing periodic angular fine structure (disks divided into equal-angle sectors with alternate sectors removed), i.e., more closely resembling *E. huxleyi* coccoliths. When the scale of the periodicity (the length of an open or closed sector measured along the circumference of the disk) was $< \lambda/4$ (where λ is the wavelength of the light *in* the medium, i.e., water), I found the backscattering to be nearly identical to that of a homogeneous disk possessing a reduced refractive index. However, significant increases in backscattering were observed when the scale of the periodicity was greater than $\lambda/4$.

For many of the cases examined, I have also computed the backscattering cross section using the Rayleigh-Gans approximation (RGA) to scattering. The RGA is applicable when the relative refractive index of the particle (m) is close to unity, and the "size" is \ll the wavelength of light divided by $|m - 1|$ [14, 15]. Thus the size need not be \ll the wavelength. It is computationally fast when compared to any other method because analytical formulas are available for many particle shapes. Moreover, extension to particles of any shape is straightforward.

In this paper I compare backscattering by disk-like particles (with refractive index 1.20 relative to water) computed using the RGA with exact (DDA) computations. The comparisons show that the RGA is sufficiently accurate to be useful as a quantitative tool for exploring the backscattering features of disk-like particles with complex structure, e.g., disks with angular periodicities or detached coccoliths from the coccolithophored *E. huxleyi*. The validity of the RGA for such particles allows investigation of the influence of their birefringence on backscattering.

2. The Electromagnetic scattering problem

Conceptually, the electromagnetic scattering problem can be developed in a simple manner. If a particle is subjected to an incident electromagnetic field $\vec{E}^{(0)}(\vec{D}_i, t)$, then a volume element dV_i at a position \vec{D}_i within the particle (Fig. 1) will experience an electric field $\vec{E}(\vec{D}_i, t)$ given by

$$\vec{E}(\vec{D}_i, t) = \vec{E}^{(0)}(\vec{D}_i, t) + \sum_j C(\vec{D}_i, \vec{D}_j) \vec{E}(\vec{D}_j, t), \quad (1)$$

where the sum *excludes* $i=j$. The E 's on both sides of this equation are unknown, while $E^{(0)}$ and C are known functions of position and time. This electric field induces a dipole moment ($d\vec{p}$) in dV_i given by

$$d\vec{p}(\vec{D}_i, t) = \rho_n \alpha \vec{E}(\vec{D}_i, t) dV_i, \quad (2)$$

where α is the polarizability tensor and ρ_n is the number density of atoms (molecules). At a great distance \vec{r}_i from the particle the field due to the dipole moment induced in dV_i is

$$d\vec{E}^{(s)} = \frac{-1}{4\pi\epsilon_0 r_i} \vec{k} \times [\vec{k} \times d\vec{p}_i(\vec{D}_i, t - r_i/c)], \quad (3)$$

where \vec{k} is the vector shown in Fig. 1 ($|\vec{k}| = 2\pi/\lambda$, where λ is the wavelength of the incident field in the medium in which the particle is immersed, and $|\vec{k}| = |\vec{k}_0|$) and c is the speed of light. The vector \vec{r}_i is assumed to be sufficiently far from the origin (O) that it may be replaced by \vec{r} except where it occurs in a phase. The total field at \vec{r} , given by

$$\vec{E}^{(s)}(\vec{r}, t) = \int d\vec{E}^{(s)}(\vec{r}, t), \quad (4)$$

is the "scattered" field.

In the laboratory reference frame (x, y, z), the incident electric field propagating in the \vec{k}_0 direction is given by

$$\vec{E}^{(0)}(\vec{D}_i, t) = \vec{E}^{(0)} \exp[i(\vec{k}_0 \cdot \vec{D}_i - \omega t)], \quad (5)$$

where the field amplitude is resolved into components parallel and perpendicular to the

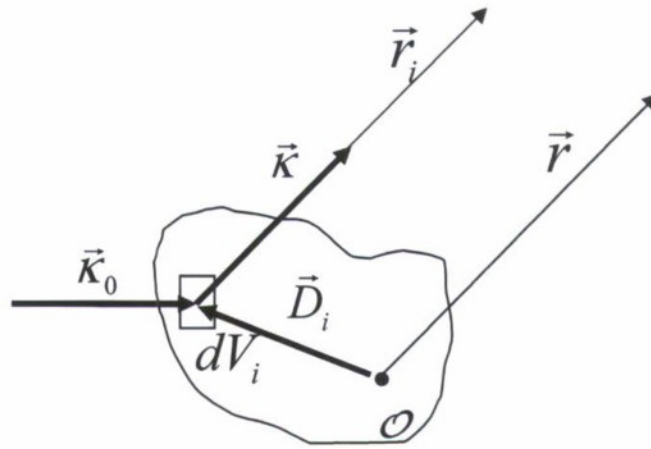


Fig. 1. A volume element dV_i , located at a point D_i from the origin of coordinates (O). The incident radiation is propagating in the κ_0 direction and the scattered radiation is propagating in the κ direction. The vector r_i is from the volume element dV_i , to a distant point at which the scattered field is measured. The vector r is from the origin to the same distant point, which is sufficiently far from the particle that the vectors r_i and r are considered to be parallel.

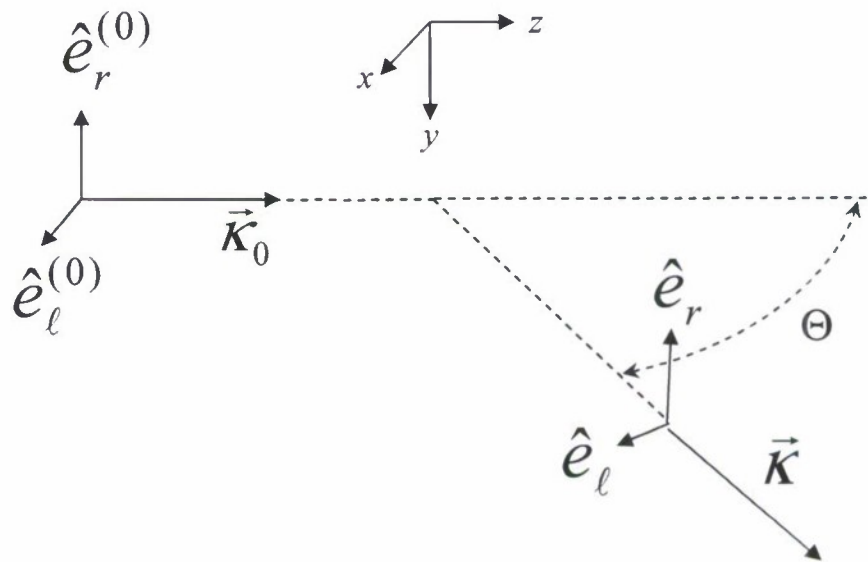


Fig. 2. The plane formed by the propagation vector $\vec{\kappa}_0$ of the incident wave and the propagation vector $\vec{\kappa}$ of the scattered wave is the scattering plane. The incident and scattered fields are resolved into components parallel and perpendicular to the scattering plane, i.e., along $(\hat{e}_\ell^{(0)}, \hat{e}_r^{(0)})$ and $(\hat{e}_\ell, \hat{e}_r)$, respectively. Θ is the scattering angle.

scattering plane (See Fig. 2):

$$\vec{E}^{(0)} = E_t^{(0)} \hat{e}_t^{(0)} + E_r^{(0)} \hat{e}_r^{(0)} = \begin{pmatrix} E_r^{(0)} \\ E_t^{(0)} \end{pmatrix}.$$

Resolving the scattered field $\vec{E}^{(s)}$ into components parallel and perpendicular to the scattering plane as well (note that $\hat{e}_t^{(0)}$ and $\hat{e}_r^{(0)}$ are not parallel), the scattered field at \vec{r} , which is in the form of a spherical wave, can then be written

$$\vec{E}^{(s)} = \frac{1}{i\kappa r} \mathbf{A} \vec{E}^{(0)} \exp[i(\kappa r - \omega t)] \quad \text{or} \quad \begin{pmatrix} E_r^{(s)} \\ E_t^{(s)} \end{pmatrix} = \frac{1}{i\kappa r} \begin{pmatrix} A_{rr} & A_{tr} \\ A_{rt} & A_{tt} \end{pmatrix} \begin{pmatrix} E_r^{(0)} \\ E_t^{(0)} \end{pmatrix} \exp[i(\kappa r - \omega t)], \quad (6)$$

where \mathbf{A} is the 2×2 scattering amplitude matrix, and

$$\vec{E}^{(s)} = E_t^{(s)} \hat{e}_t + E_r^{(s)} \hat{e}_r = \begin{pmatrix} E_r^{(s)} \\ E_t^{(s)} \end{pmatrix}.$$

3. The differential scattering cross section

To relate the scattered field to scattering cross sections, etc., we recall that the time averaged Poynting vector of the scattered field is

$$\langle \vec{S} \rangle = \frac{\hat{\kappa}}{2\mu_0 c} \langle E_t E_t^* + E_r E_r^* \rangle = \frac{\hat{\kappa}}{2\mu_0 c} \langle \tilde{\vec{E}}^* \cdot \vec{E} \rangle = \hat{\kappa} \frac{dP}{dA}, \quad (7)$$

Where the superscript * indicates the complex conjugate, the tilde indicates the transposed matrix and, dP is the power crossing an area dA oriented normal to the propagation direction $\hat{\kappa}$ (i.e., the irradiance associated with the propagating field). The differential scattering cross section is defined to be the power scattered into a solid angle $d\Omega$ divided by the irradiance of the incident beam, i.e.,

$$\frac{d\sigma}{d\Omega} \equiv \frac{dP^{(s)}/d\Omega}{dP^{(0)}/dA} = r^2 \frac{\langle \tilde{\vec{S}}^{(s)} \rangle}{\langle \tilde{\vec{S}}^{(0)} \rangle}, \quad (8)$$

where the superscript "s" stands for "scattered" and the superscript "0" stands for "incident." The required Poynting vectors are given by

$$\langle \tilde{\vec{S}}^{(0)} \rangle = \frac{1}{2\mu_0 c} \langle \tilde{\vec{E}}^{(0)*} \cdot \vec{E}^{(0)} \rangle \quad \text{and} \quad \langle \tilde{\vec{S}}^{(s)} \rangle = \frac{1}{2\mu_0 c} \frac{1}{\kappa^2 r^2} \langle \tilde{\vec{E}}^{(0)*} \tilde{\mathbf{A}} \cdot \mathbf{A} \vec{E}^{(0)} \rangle,$$

so

$$\frac{d\sigma}{d\Omega} = \frac{1}{\kappa^2} \frac{\langle \tilde{\vec{E}}^{(0)*} \tilde{\mathbf{A}} \cdot \mathbf{A} \vec{E}^{(0)} \rangle}{\langle \tilde{\vec{E}}^{(0)*} \vec{E}^{(0)} \rangle}. \quad (9)$$

If the incident field is unpolarized, then

$$\langle E_r^{(0)*} E_r^{(0)} \rangle = \langle E_t^{(0)*} E_t^{(0)} \rangle \quad \text{and} \quad \langle E_r^{(0)*} E_t^{(0)} \rangle = 0 = \langle E_t^{(0)*} E_r^{(0)} \rangle,$$

and the differential cross section becomes

$$\frac{d\sigma}{d\Omega} = \frac{1}{\kappa^2} \frac{\langle \tilde{\vec{E}}^{(0)*} \tilde{\mathbf{A}} \cdot \mathbf{A} \vec{E}^{(0)} \rangle}{\langle \tilde{\vec{E}}^{(0)*} \vec{E}^{(0)} \rangle} = \frac{1}{2\kappa^2} (|A_{rr}|^2 + |A_{tr}|^2 + |A_{rt}|^2 + |A_{tt}|^2). \quad (10)$$

(Note: the quantity S_{11} defined by Bohren and Huffman [14] is $\kappa^2 d\sigma/d\Omega$.)

4. The Rayleigh-Gans approximation

In its simplest form, in the Rayleigh-Gans Approximation [4, 14, 15] (RGA) to scattering, the sum in the Eq. (1) is ignored ($C = 0$), i.e., the only field experienced by dV_i is the incident

field. Thus, the RGA provides the “zeroth-order” approximation to the scattered field. In the laboratory reference frame (x, y, z) , the incident electric field is given by Eq. (5) so the induced dipole moment [Eq. (2)] is

$$\begin{aligned} d\vec{p}_i(\vec{D}_i, t - r_i/c) &= \rho_n \alpha(\vec{D}_i) \vec{E}^{(0)}(\vec{D}_i, t - r_i/c) dV_i \\ &= \rho_n \alpha(\vec{D}_i) \vec{E}^{(0)} \exp[i(\vec{k}_0 \cdot \vec{D}_i - \omega t + r_i \omega/c)] dV_i. \end{aligned}$$

Then noting that $\kappa = \omega/c$, we have $r_i \omega/c = \kappa r_i = \kappa \vec{r} - \vec{k} \cdot \vec{D}_i$,

$$d\vec{p}_i(\vec{D}_i, t - r_i/c) = \rho_n \alpha(\vec{D}_i) \vec{E}^{(0)} \exp[i(\vec{k}_0 - \vec{k}) \cdot \vec{D}_i] \exp[i(\kappa r - \omega t)] dV_i. \quad (11)$$

Resolving the fields into components parallel and perpendicular to the scattering plane, as in Eq. (6) the scattered field is

$$d\vec{E}^{(s)} = \frac{1}{i\kappa} d\mathbf{A} \vec{E}^{(0)} \exp[i(\kappa r - \omega t)], \quad (12)$$

where $d\mathbf{A}_i$ is the contribution to the matrix \mathbf{A} from dV_i and is given by

$$d\mathbf{A}_i = \frac{-i\rho_n \kappa}{4\pi\epsilon_0} \vec{k} \times [\vec{k} \times \alpha(\vec{D}_i)] \exp[i(\vec{k}_0 - \vec{k}) \cdot \vec{D}_i] dV_i. \quad (13)$$

The scattering plane is the x - z plane (Fig. 2), so

$$\begin{aligned} \vec{E}^{(0)} &= E_t^{(0)} \hat{e}_t^0 + E_r^{(0)} \hat{e}_r^0 = E_t^{(0)} \hat{e}_x - E_r^{(0)} \hat{e}_y, \\ \vec{E}^{(s)} &= E_t^{(s)} \hat{e}_t + E_r^{(s)} \hat{e}_r = E_t^{(s)} \cos \Theta \hat{e}_x - E_r^{(s)} \hat{e}_y - E_t^{(s)} \sin \Theta \hat{e}_z, \\ \vec{k} &= \kappa(\hat{e}_x \sin \Theta + \hat{e}_z \cos \Theta), \end{aligned}$$

and

$$\vec{k}_0 = \kappa \hat{e}_z.$$

Inserting these into the equation for $d\mathbf{A}_i$ yields

$$d\mathbf{A}_i = \frac{i\rho_n \kappa^3}{4\pi\epsilon_0} \begin{pmatrix} -\alpha_{yy} & \alpha_{xy} \\ -\alpha_{yz} \sin \Theta + \alpha_{xy} \cos \Theta & \alpha_{xz} \sin \Theta - \alpha_{xx} \cos \Theta \end{pmatrix} \exp[i(\vec{k}_0 - \vec{k}) \cdot \vec{D}_i] dV_i, \quad (14)$$

where the α 's are the components of α in the laboratory reference frame (x, y, z) . The total scattered field is found by integration over the volume of the object:

$$\mathbf{A} = \frac{i\rho_n \kappa^3}{4\pi\epsilon_0} \iiint_V \begin{pmatrix} -\alpha_{yy} & \alpha_{xy} \\ -\alpha_{yz} \sin \Theta + \alpha_{xy} \cos \Theta & \alpha_{xz} \sin \Theta - \alpha_{xx} \cos \Theta \end{pmatrix} \exp[i(\vec{k}_0 - \vec{k}) \cdot \vec{D}] dV. \quad (15)$$

If the α 's are independent of position within the particle, the matrix can be removed from the integration. If the particle's polarizability tensor is isotropic (i.e., $\alpha_{ij} = \alpha \delta_{ij}$) then \mathbf{A} reduces to

$$\mathbf{A} = \frac{-i\rho_n \alpha \kappa^3}{4\pi\epsilon_0} \begin{pmatrix} 1 & 0 \\ 0 & \cos \Theta \end{pmatrix} \iiint_V \exp[i(\vec{k}_0 - \vec{k}) \cdot \vec{D}] dV, \quad (16)$$

and the differential cross section becomes

$$\frac{d\sigma}{d\Omega} = \left(\frac{\rho_n \alpha \kappa^2}{4\pi\epsilon_0} \right)^2 \frac{(1 + \cos^2 \Theta)}{2} \left| \iiint_V \exp[i(\vec{k}_0 - \vec{k}) \cdot \vec{D}] dV \right|^2. \quad (17)$$

The polarizability of the particle can be related to the refractive index, m , through the Clausius-Mossotti equation:

$$\frac{\rho_n \alpha}{\epsilon_0} = 3 \left(\frac{m^2 - 1}{m^2 + 2} \right); \quad (18)$$

and defining

$$R \equiv \iiint_V \exp[i(\vec{k}_0 - \vec{k}) \cdot \vec{D}] dV,$$

we have

$$\frac{d\sigma}{d\Omega} = \frac{9}{16\pi^2} \kappa^4 \left(\frac{m^2 - 1}{m^2 + 2} \right)^2 \left(\frac{1 + \cos^2 \Theta}{2} \right) |R|^2 \quad (19)$$

for the differential scattering cross section of a single particle of volume V . If the particle is immersed in a refracting medium, then m is the refractive index of the particle *relative* to the medium.

The total (σ) and back (σ_b) scattering cross sections are, respectively,

$$\sigma = \iint_{4\pi} \frac{d\sigma}{d\Omega} d\Omega \quad \text{and} \quad \sigma_b = \iint_{\text{Back } 2\pi} \frac{d\sigma}{d\Omega} d\Omega, \quad (20)$$

while the scattering phase and volume scattering functions are

$$P(\Theta) = \frac{4\pi}{\sigma} \frac{d\sigma(\Theta)}{d\Omega} \quad \text{and} \quad \beta(\Theta) = N \frac{d\sigma(\Theta)}{d\Omega}, \quad (21)$$

where N is the number density of scatterers. The contribution that particles of a given size and shape make to the total scattering coefficient (b) and the backscattering coefficient (b_b) are $b = N\sigma$ and $b_b = N\sigma_b$, respectively. In the RGA, the shape of the particle enters only through the computation of R . Analytic formulas are available for simple shapes, e.g., spheres and cylinders; however, it is easy to carry out the integrations numerically for particles of any shape. For particles other than spheres, R depends on the orientation of the particle. For particles with a given orientational distribution function, $d\sigma/d\Omega$ must be computed for a large number of orientations and the appropriate weighted average formed.

The fact that dV_i is subjected only to the incident field requires that two conditions must hold for the RGA to have validity: (1) there must be insignificant refraction or reflection at the surface of the particle, which implies $|m - 1|$ must be $\ll 1$; and (2) the phase of the incident field must not shift significantly over distances of the order of the "size" (L) of the particle, which requires $\kappa L |m - 1| \ll 1$.

This is one of many forms of the RGA. The resulting cross section becomes coincident with the equations in van de Hulst¹⁵ by using the requirement that $|m - 1| \ll 1$ so that $\rho_n \alpha / \epsilon_0 \approx 2(m - 1)$. Refinements to the RGA have been proposed by several authors, such as using the electrostatic approximation to relate the polarizabilities to the refractive index [16], or replacing the magnitude of the propagation vector in the medium by that in the particle [17]. I employ the form presented here because it is more closely related to the DDA, i.e., the DDA [18] uses the Clausius-Mossotti relationship modified to include radiation reaction and the "lattice dispersion relation."

5. Comparison between RGA and DDA for disk-like particles

In what follows we compare the backscattering cross sections (σ_b) of *randomly-oriented* disk-like objects computed via the RGA and the DDA. The DDA results are taken as "exact" computations (the DDA-computed σ_b 's are expected to be in error by no more than 5%). As an early motivation for such comparisons was interest in the backscattering of coccoliths detached from *E. huxleyi* suspended in water, I consider disks with diameters 1.5 to 2.75 μm with $m = 1.2$ (Calcite in water). Figure 3 provides such a comparison for a 2.75 μm homogeneous disk of various thicknesses (t). The comparison shows that the RGA is

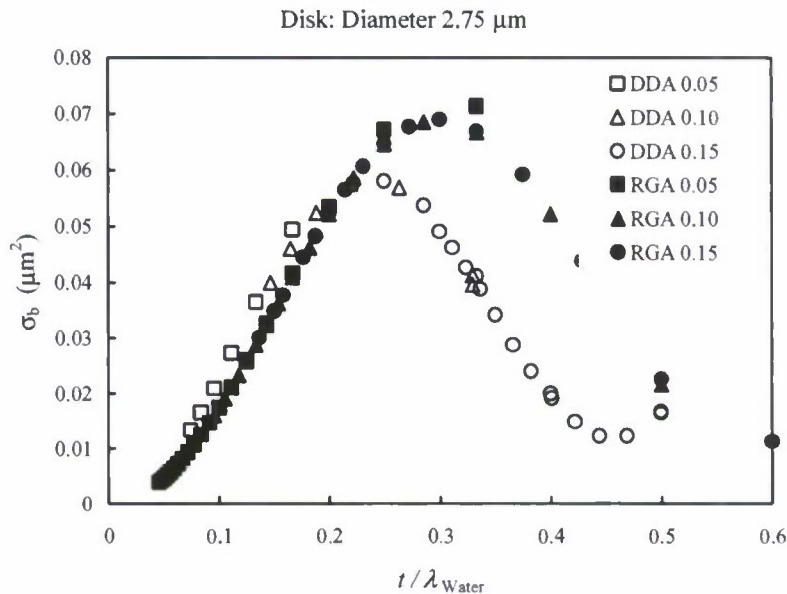


Fig. 3. Comparison of the backscattering cross section computed with the RGA and the DDA for a homogeneous disk of diameter 2.75 μm and thicknesses 0.05, 0.10, and 0.15 μm .

close to the DDA for t/λ_{Water} less than, or approximately equal to, 0.20 to 0.25. Perhaps more importantly, the comparison shows that σ_b can be expected to oscillate with increasing t (or decreasing λ_{Water}), i.e., the RGA also provides the *qualitative character* of the spectral variation of σ_b . It should be pointed out that the (approximate) “physical optics” developed by model of Gordon and Du [5] out performs the RGA when $t/\lambda_{\text{Water}} > 0.2$, following the DDA reasonably well up to a t/λ_{Water} of 0.8.; however, it cannot be applied to the more complex particle shapes of interest here, e.g., disk-like particles with periodic angular fine structure.

For a more complex example, Fig. 4 compares RGA and DDA computations of σ_b for the Gordon and Du [5] “fishing-reel” model of a detached coccolith. The fishing-reel model consists of two parallel disks of diameter D_o with material removed from a concentric circle of diameter D_i (i.e., a washer-like object). The two disks are joined together by a hollow cylinder of inner diameter D_i and outer diameter D_r . The axis of the cylinder passes through the center of both disks. The individual disks have a thickness of 50 nm and the space between them (the height of the joining cylinder) is t . Table 1 provides values of the parameters of the three fishing-reel models investigated. The three models all have the same volume ($\sim 0.587 \mu\text{m}^3$). This is accomplished by decreasing the thickness of the wall of the connecting cylinder as shown in Table 1.

For these models, the individual disks have a thickness of 0.05 μm , and therefore are within the $t/\lambda_{\text{Water}} < 0.2$ criterion from Fig. 3 in the visible. As in Fig. 3, Fig. 4 shows that the RGA and DDA produce *qualitatively similar* spectral variations, and surprisingly good quantitative agreement even though the total thickness of the particle exceeds λ_{Water} in some cases, and the total diameter is several times λ_{Water} . Comparison of the two suggests that the

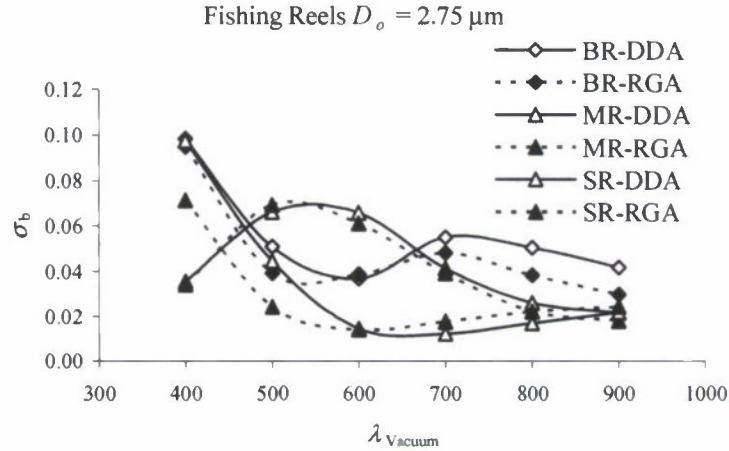


Fig. 4. Comparison of RGA and DDA computations for the Gordon and Du [5] "fishing reel" models of a detached coccolith.

Table 1: Parameters of the Gordon and Du [5] "Fishing-reel" model of a detached coccolith.

Model	D_o (μm)	D_i (μm)	D_r (μm)	t (μm)
SR	2.75	1.38	1.93	0.1
MR	2.75	1.38	1.68	0.2
BR	2.75	1.38	1.58	0.3

RGA can be a valuable tool in exploring problems involving multiple disks as long as the *individual disks* satisfy the $t/\lambda_{\text{water}} < 0.2$ criterion.

In an effort to understand the influence of small-scale periodic structure in disk-like objects on backscattering, I examined [11] backscattering by a "sectorized" disk formed by starting with a homogeneous disk and removing sectors. Specifically, the disk was divided into equal angle sectors of angle $\Delta\alpha$ and alternate sectors were removed. The angle $\Delta\alpha$ was given by

$$\Delta\alpha = \frac{2\pi}{2^n}$$

where n is an integer. Figure 5 provides the positions of one layer of dipoles for the resulting structures for $n = 4$ to 7. I will refer to these objects as "pinwheels." If we let s be the arc length of the open (or closed) regions at the perimeter of the pinwheel, then $s = D_d\Delta\alpha/2$, where D_d is the diameter of the disk. The values of s for the various cases that I examined ($D_d = 1.5 \mu\text{m}$) were such that at a wavelength (λ) of 400 nm in vacuum (300 nm in water), as n progresses from 4 to 7, s took on the values λ , $\lambda/2$, $\lambda/4$, and $\lambda/8$ in water. One of the main goals of my study was to determine if a relationship exists between s and λ where the periodic structure becomes important (or unimportant) to the backscattering.

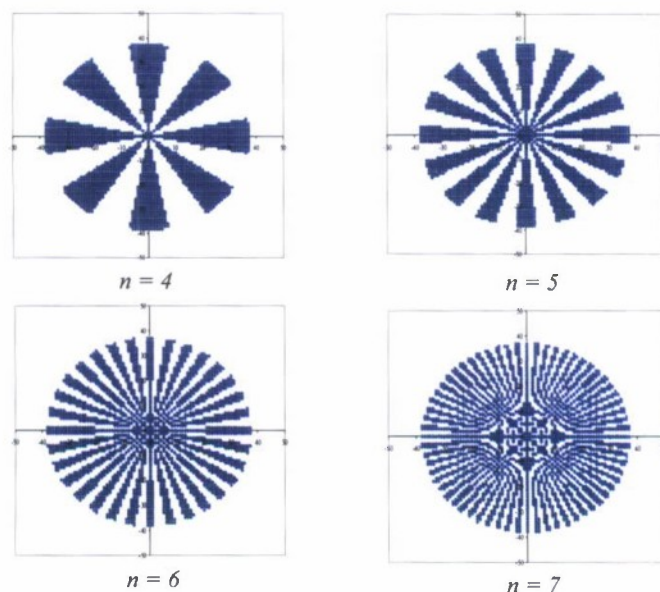


Fig. 5. Sectorized disks ("pinwheels") for various values of n used in this study.

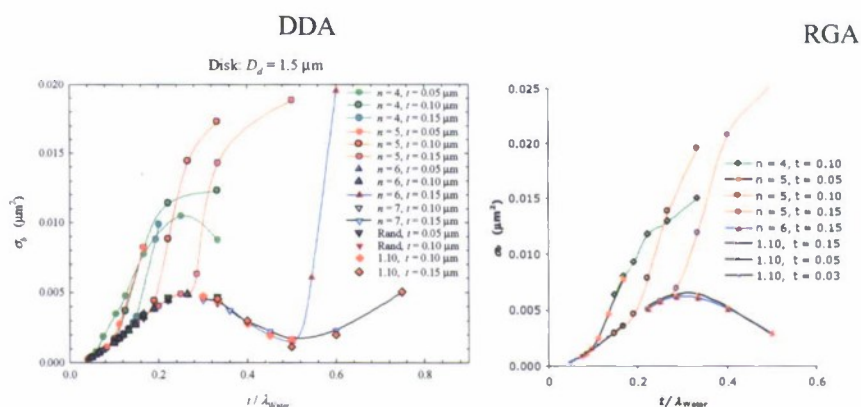


Fig. 6. Comparison of DDA and RGA backscattering by sectorized disks in Fig. 5.

The results of the computations of the backscattering cross section, σ_b , carried out for 1.5 μm pinwheels are provided in Fig. 6 (DDA on the left from Ref. 11, and RGA on the right), which displays σ_b as function of the thickness (t) of the disk divided by the wavelength of the light in water (λ_{water}). Three thicknesses of the disk are used: 0.05, 0.10, and 0.15 μm . The wavelength λ_{water} covers the range from 200 nm to over 1000 nm. Note the qualitative similarity between the DDA and the RGA computations. Both show that the backscattering appears to follow a "universal curve" that is close to that for a homogeneous disk with a reduced index $m = 1.10$ rather than 1.20 (labeled 1.10 in the key to the figure); however, as the wavelength decreases σ_b suddenly departs from the universal curve and increases dramatically. This was first observed through extensive computations using the DDA; however, in this case, the behavior could have been predicted based on the RGA computations. (The departure of σ_b from the universal curve occurs when the maximum arc

length of the open or closed regions of the pinwheel exceeds $\lambda_{\text{Water}}/4$). In Fig. 7 the comparisons in Fig. 6 are carried to larger values of t/λ_{Water} , and show that the RGA agrees well with the DDA for values of t/λ_{Water} up to, and somewhat beyond the first maximum that occurs in σ_b after the departure from the “universal curve.” This maximum is near $s/\lambda_{\text{Water}} = 1/2$. For larger values of t/λ_{Water} the RGA still provides the qualitative nature of the variation of σ_b with t/λ_{Water} ; however, it no longer quantitatively reproduces the DDA computations.

In Fig. 8 a more complex geometry – parallel pinwheels – is examined. This is somewhat similar to the “fishing reel” model [5] for detached coccoliths, but uses sectorized disks (washers) with $n = 5$ and 6 rather than homogeneous disks and the outside diameter is 1.50 μm rather than 2.75 μm . Again, the agreement between RGA and DDA is quite good throughout the visible, even in a quantitative sense.

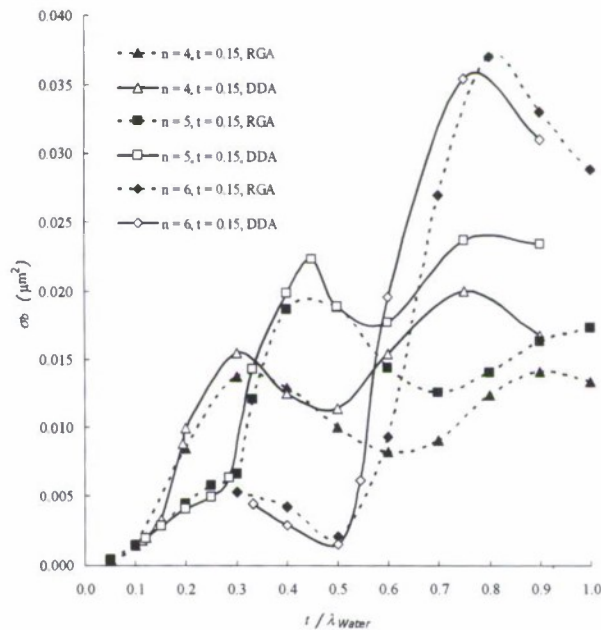


Fig. 7. Comparison of DDA and RGA backscattering by sectorized disks in Fig. 5.

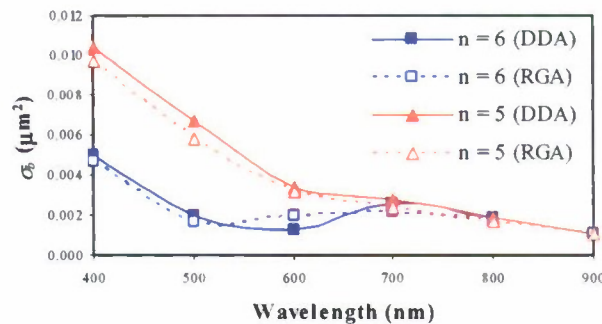


Fig. 8. Comparison of DDA and RGA backscattering by parallel sectorized ($n = 5$ and 6) washers. The individual washers have an outside diameter of 1.50 μm , inside diameter 1.00 μm and thickness 0.05 μm . They are separated by a space of 0.30 μm .

6. Application: estimate of the influence of *E. huxleyi* birefringence on backscattering

As the *E. huxleyi* coccolith is composed of calcite, one would expect it to be birefringent. This is indeed the case. The c-axis (optical axis) of the component parts of the *E. huxleyi* coccolith is radial, i.e., along the “spoke-like” structures [19]. How does this birefringence influence the backscattering? Since RGA provides an adequate description of the backscattering of homogeneous or structured disk-like objects as long as $t/\lambda_{\text{water}} < 0.2$, which is satisfied by the individual coccolith plates throughout the visible, we expect that it would apply equally well to a birefringent disk. Thus, we will investigate the possible influence of birefringence on *E. huxleyi* backscattering by comparing the backscattering in the RGA of a birefringent and an isotropic disk. Computation of the scattering matrix **A** for an anisotropic disk, for which the optical axis at any point is radial, is sketched out in the Appendix. A uniaxial crystal, Calcite has two refractive indices: m_e for propagation with the electric vector parallel to the c-axis; and m_o for propagation with the electric vector perpendicular to the c-axis. Letting m_i represent the refractive index of the isotropic disk, we take

$$\frac{\rho_n a}{\epsilon_0} = 3 \left(\frac{m_e^2 - 1}{m_e^2 + 2} \right) \quad \text{and} \quad \frac{\rho_n b}{\epsilon_0} = 3 \left(\frac{m_o^2 - 1}{m_o^2 + 2} \right)$$

for the polarizabilities a and b (see the Appendix) of the birefringent disk, and

$$\frac{\rho_n \alpha}{\epsilon_0} = 3 \left(\frac{m_i^2 - 1}{m_i^2 + 2} \right)$$

for the isotropic disk. Clearly, m_i must depend on m_o and m_e in some manner, and one of the goals of this exercise is to find the combination that provides the best agreement for backscattering of the isotropic and the anisotropic cases. If the disk were composed of small grains of Calcite in random orientation, one would expect [20] the average refractive index

Disk: $D = 2.75 \mu\text{m}$, $t = 0.05 \mu\text{m}$

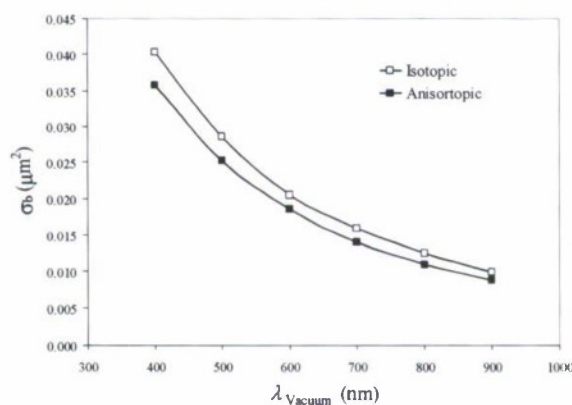


Fig. 9. Comparison of RGA computations of backscattering for a randomly-oriented birefringent disk and an isotropic disk with $m_i = (2m_o + m_e)/3$.

for unpolarized light to be approximately $(2m_o + m_e)/3$. Using tabulated values for the refractive indices of Calcite [21] near 500 nm and taking 1.338 for the index of water, we have $m_o = 1.241$, $m_e = 1.113$, and $m_i = 1.198$ (close to the value 1.20 used in the earlier

computations). Comparison of the RGA-computed σ_b for the radially-anisotropic disk with these values of m_o and m_e with the isotropic disk with index $m_i = (2m_o + m_e)/3$ is provided in Fig. 9. The isotropic disk's backscattering cross section is seen to be somewhat higher than the birefringent disk. The two can be brought into agreement by taking $m_i = 1.188 = 0.57 m_o + 0.43 m_e$. (For the total scattering cross section, $m_i = (2m_o + m_e)/3$ provides better agreement between the two than $m_i = 1.188$.) This suggests that for the computation of backscattering by model coccoliths with the DDA, a zeroth-order account of the birefringence can be effected by using $m_i = 1.188$ rather than 1.198.

7. Concluding Remarks

The value of the RGA in obtaining qualitative information regarding backscattering by disk-like particles has been demonstrated. The success of the RGA in this case derives from the fact that, unlike a spherical particle with the same mass, most of the volume elements of a thin disk are far enough away from any given element that their interaction is small, i.e., a relatively small amount of the total mass of the particle is close to any one of the volume elements.

I am not advocating the use of the RGA for quantitative computations of σ_b for disk-like particles. Rather, because it is computationally fast compared to the DDA, it can be used to *explore* the backscattering of disk-like models of marine particles for the purpose of either excluding models with unacceptable qualitative behavior, or selecting promising models for further study using the more time-consuming DDA.

8. Appendix: scattering by a birefringent disk

Here we develop the formulas for scattering from a birefringent disk. As our application is to the *E. huxleyi* coccoliths we take the disk to be uniaxial with the optical axis at any point in the disk in the radial direction. We develop the anisotropic case first and then reduce these formulas to the isotropic case.

A. Anisotropic case

Figure A1 provides the geometry of the scattering problem. The body-fixed coordinate system is cylindrical with radial coordinate ρ' , the angle η' , and the coordinate z' normal to the axis of the disk. In the integral for **A**, Eq. (15), the required elements of the polarizability matrix ($\alpha_{\rho'\rho'}$, $\alpha_{\eta'\eta'}$, $\alpha_{z'z'}$, and $\alpha_{\rho'\eta'}$, $\alpha_{\rho'z'}$, and $\alpha_{\eta'z'}$) must be provided in laboratory-fixed reference system and depend on the particle's orientation. However, in the body-fixed reference system the polarizability matrix assumes a particularly simple form:

$$\alpha_B = \begin{pmatrix} \alpha_{\rho'\rho'} & 0 & 0 \\ 0 & \alpha_{\eta'\eta'} & 0 \\ 0 & 0 & \alpha_{z'z'} \end{pmatrix} \equiv \begin{pmatrix} a & 0 & 0 \\ 0 & b & 0 \\ 0 & 0 & b \end{pmatrix}.$$

The transformation of this matrix to the laboratory-fixed system is straightforward:

$$\alpha = \tilde{\mathbf{U}} \mathbf{B} \alpha_B \mathbf{B} \mathbf{U},$$

where the matrices **U** and **B** are related to the Euler angles (θ, ϕ, ψ) and η' (Fig. A1 and Fig. A2) through

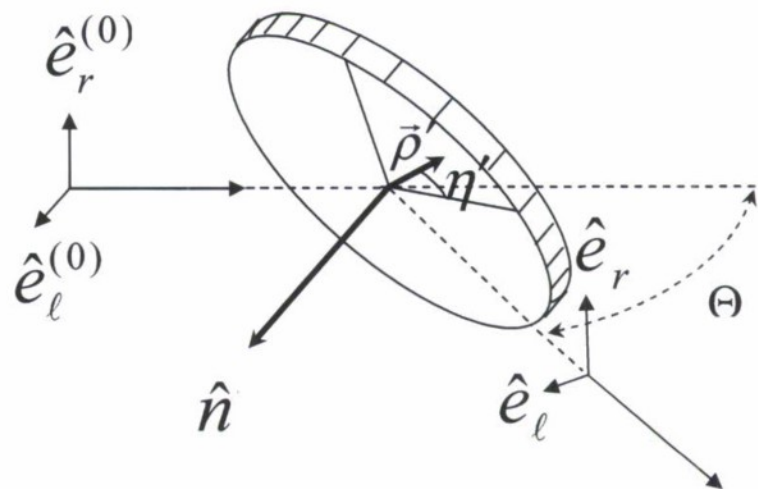


Fig. A1. A schematic of scattering by a disk. The cylindrical coordinate system (ρ', η', z') is fixed with respect to the disk (z' is in the direction of the normal, n).

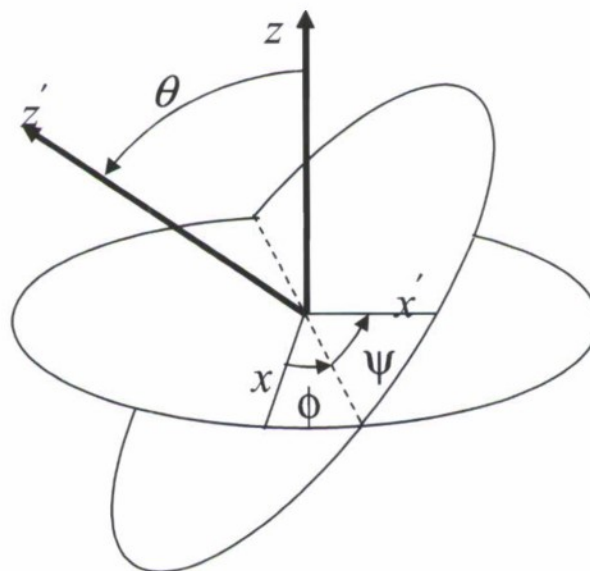


Fig. A2. Relationship between the laboratory-fixed coordinate system (x, y, z) and the body-fixed system (x', y', z') or (ρ', η', z') . θ , ϕ and ψ are the Euler angles. Because of the symmetry of the disk the angle ψ can be set to zero.

$$\mathbf{U} = \begin{pmatrix} \cos\psi \cos\phi - \cos\theta \sin\phi \sin\psi & \cos\psi \sin\phi + \cos\theta \cos\phi \sin\psi & \sin\psi \sin\theta \\ -\sin\psi \cos\phi - \cos\theta \sin\phi \cos\psi & -\sin\psi \sin\phi + \cos\theta \cos\phi \cos\psi & \cos\psi \sin\theta \\ \sin\theta \sin\phi & -\sin\theta \cos\phi & \cos\theta \end{pmatrix}$$

and

$$\mathbf{B} = \begin{pmatrix} \cos\eta' & \sin\eta' & 0 \\ -\sin\eta' & \cos\eta' & 0 \\ 0 & 0 & 1 \end{pmatrix}.$$

Because of the symmetry of the disk, the Euler angle ψ is redundant and may be set to zero. The matrix elements of α thus depend on θ , ϕ , and η' .

To carry out the required integrations to find \mathbf{A} , we need $\vec{D} = \vec{\rho}' + \vec{z}'$, and by resolving $(\vec{\kappa}_0 - \vec{\kappa})$ into components parallel and normal to the disk's surface, we find

$$(\vec{\kappa}_0 - \vec{\kappa}) \cdot \vec{D} = 2\kappa \sin(\Theta/2) [\rho' \cos(\eta' - \gamma) \sin\beta + z' \cos\beta]$$

and

$$\cos\beta = \cos\theta \sin(\Theta/2) - \sin\theta \sin\phi \cos(\Theta/2),$$

where γ is the angle between the component of $(\vec{\kappa}_0 - \vec{\kappa})$ parallel to the plane of the disk and the x' axis. A typical integral that must be evaluated to find \mathbf{A} is then

$$\int_0^R \int_0^{2\pi} \int_0^\pi \alpha_{yy} \exp\{i2\kappa \sin(\Theta/2) [\rho' \cos(\eta' - \gamma) \sin\beta + z' \cos\beta]\} \rho' d\eta' d\rho' dz'.$$

Explicit relationships for the components of α are:

$$\begin{aligned} \alpha_{xx} = & \frac{1}{2} \cos^2\eta' [a + b + (a - b) \cos 2\phi] \\ & + 2(-a + b) \cos\eta' \sin\eta' \cos\theta \cos\phi \sin\phi \\ & + \sin^2\eta' [b \sin^2\theta + \cos^2\theta (b \cos^2\phi + a \sin^2\phi)], \end{aligned}$$

$$\begin{aligned} \alpha_{xy} = & (a - b) (\cos\theta \cos\phi \sin\eta' + \cos\eta' \sin\phi) \\ & \times (\cos\eta' \cos\phi - \cos\theta \sin\eta' \sin\phi), \end{aligned}$$

$$\alpha_{xz} = (a - b) \sin\eta' \sin\theta (\cos\eta' \cos\phi - \cos\theta \sin\eta' \sin\phi),$$

$$\begin{aligned} \alpha_{yy} = & \frac{1}{2} \cos^2\eta' [a + b - (a - b) \cos 2\phi] \\ & - 2(-a + b) \cos\eta' \sin\eta' \cos\theta \cos\phi \sin\phi \\ & + \sin^2\eta' [b \sin^2\theta + \cos^2\theta (a \cos^2\phi + b \sin^2\phi)], \end{aligned}$$

$$\alpha_{yz} = (a - b) \sin\eta' \sin\theta (\cos\eta' \sin\phi + \cos\theta \sin\eta' \cos\phi),$$

$$\alpha_{zz} = b \cos^2 \eta' + \sin^2 \eta' (a \sin^2 \theta + b \cos^2 \theta),$$

$$\alpha_{yx} = \alpha_{xy}, \quad \alpha_{zx} = \alpha_{xz}, \quad \alpha_{zy} = \alpha_{yz}.$$

Thus, for a given orientation of the disk (given θ and ϕ), all of the required integrals are of the form

$$\int_0^R \int_0^{2\pi} \int_0^\pi \left(\frac{\cos^2 \eta'}{\sin^2 \eta'} \right) \exp\{i2\kappa \sin(\Theta/2) [\rho' \cos(\eta' - \gamma) \sin \beta + z' \cos \beta]\} \rho' d\eta' d\rho' dz'.$$

Figure A3 provides the required η' integrals, and this integrates to

$$\frac{2\pi}{\kappa'^2} \begin{pmatrix} 1 - J_0(\kappa'R) \\ 0 \\ \kappa'R J_1(\kappa'R) + J_0(\kappa'R) - 1 \end{pmatrix} \frac{2}{k'} \sin(k't/2),$$

where

$$\kappa' = 2\kappa \sin(\Theta/2) \sin \beta,$$

$$k' = 2\kappa \sin(\Theta/2) \cos \beta,$$

and

$$\cos \beta = \cos \theta \sin(\Theta/2) - \sin \theta \sin \phi \cos(\Theta/2).$$

The disk orientation enters through the variation of the α_{ij} 's with θ and ϕ as well as through κ' and k' .

The complete formulas for the scattering amplitude matrix and cross sections are straightforward to write down, but are too complicated to be informative. Rather, we shall only provide results of numerical computations in the text. However, in the case of an isotropic disk, the formulas are simple and are provided in the next subsection.

B. Isotropic case

When the polarizability of the disk material is isotropic, i.e., $a = b$, then $\alpha_{ij} = a\delta_{ij}$, and the scattering amplitude matrix becomes

$$\begin{aligned} \mathbf{A} &= \frac{-i\rho_n \kappa^3 a}{4\pi\epsilon_0} \begin{pmatrix} 1 & 0 \\ 0 & \cos \Theta \end{pmatrix} \iiint_V \exp[i(\vec{\kappa}_0 - \vec{\kappa}) \cdot \vec{D}] dV \\ &= \frac{-i\rho_n \kappa^3 a}{4\pi\epsilon_0} \begin{pmatrix} 1 & 0 \\ 0 & \cos \Theta \end{pmatrix} \frac{2\pi}{\kappa'^2} \kappa'R J_1(\kappa'R) \frac{2}{k'} \sin(k't/2). \end{aligned}$$

The differential cross section is then

$$\frac{d\sigma}{d\Omega} = \left(\frac{\rho_n \kappa^2 a}{4\pi\epsilon_0} \right)^2 \left(2V \frac{J_1(\kappa'R)}{\kappa'R} \frac{\sin(k't/2)}{k't/2} \right)^2 \left(\frac{1 + \cos^2 \Theta}{2} \right).$$

Note that the orientation of the disk enters only through the parameters κ' and

k' .

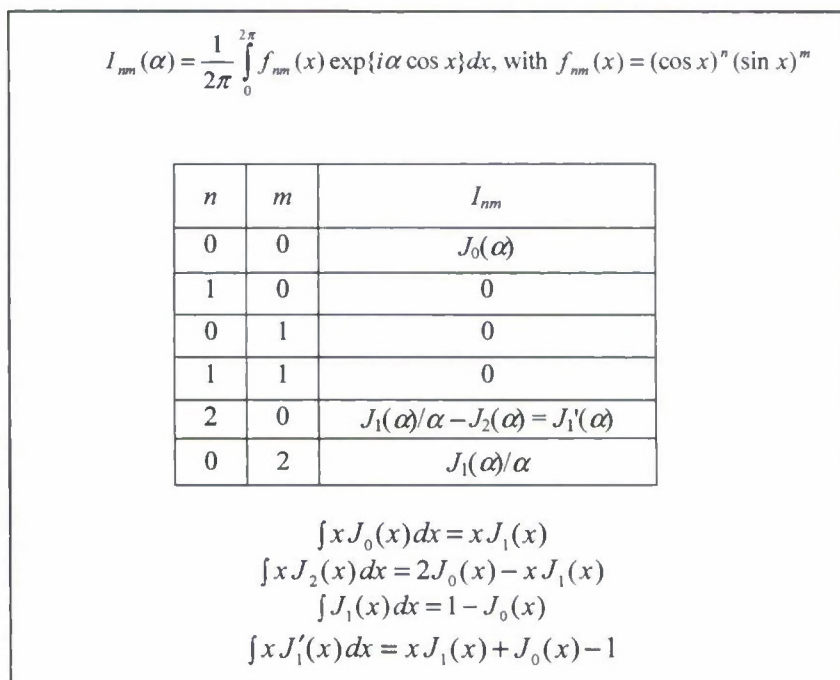


Fig. A3. The required integrals for the evaluation of the matrix A. The J 's are Bessel functions.

Acknowledgments

The author is indebted to K. Voss for many useful discussions, B. Draine and P. Flatau for providing their DDA code, and the Office of Naval Research for support under Grant Numbers N000140510004 and N000140710226.